UNIVERSITÀ DEGLI STUDI DELL'INSUBRIA

DIPARTIMENTO DI SCIENZA E ALTA TECNOLOGIA

DOTTORATO
FISICA E ASTROFISICA

Flocking in unbounded space: direct and inverse approaches to the weak cohesion problem

Supervisor
Prof. Francesco Ginelli
Co-supervisor
Prof. Antonio Celani

PhD Candidate
Martino Brambati

Academic year
2024/2025

Abstract

Active matter systems, composed of self-driven interacting units, provide a paradigmatic example of collective behavior far from equilibrium. Among these, flocking represents a striking form of large-scale organization, characterized by coherent motion and long-range correlations. While most theoretical and numerical studies have focused on bulk properties under periodic boundary conditions, much less attention has been devoted to finite, cohesive flocks evolving in unbounded space, as observed in natural systems. In this thesis, we investigate the physical characterization of cohesive, finite flocks that do not rely on a strongly ordered internal structure. We address this problem from two complementary perspectives. First, once weak cohesion is prescribed at the microscopic level, we ask how the size and shape of the resulting self-bound active object are selected, how its stability is maintained over long timescales, and which collective modes govern its large-scale deformations. Second, reversing the logic, we ask which local behavioral objectives are sufficient for the emergence of cohesive polar motion. To tackle these questions, we combine two complementary approaches. In a direct approach, we introduce a minimal Vicsek-like model in which alignment is supplemented by a weak social attraction and analyze the resulting finite flocks using both theoretical and numerical methods. We show that their global properties can be captured through a mode decomposition and demonstrate that these systems can exhibit underdamped collective shape oscillations despite purely overdamped microscopic dynamics. In an inverse approach, we employ a multi-agent reinforcement learning framework in which agents learn to balance attractive and aligning behavior from local information and biologically motivated objectives. We show that cohesive polar flocking can emerge from the combined requirement of staying together while avoiding potential collisions. Relaxing the latter constraint leads instead to cohesive but non-polar swarming states. Together, these results provide a unified perspective linking microscopic interactions and behavioral rules to the emergent static and dynamical properties of cohesive flocks in unbounded domains and contribute to the broader understanding of finite active systems in non-equilibrium statistical physics.

Contents

Introduction

Statistical mechanics is a branch of physics that aims to characterize systems composed of a vast number of microscopic degrees of freedom, linking macroscopic emergent properties to the behaviour of their interacting constituents. Despite the apparent complexity of such systems, it provides powerful tools to describe them in terms of a few macroscopic — and often experimentally accessible — quantities, such as mechanical pressure, density, or magnetization. These quantities may be expressed as averages over microscopic states, with a measure given by well known statistical ensembles for systems at *thermodynamic equilibrium*.
Equilibrium statistical mechanics has been remarkably successful in describing a wide range of physical systems. However, most systems encountered in nature do not reside at equilibrium. They are continuously driven by fluxes of particles or by injections of energy at either the microscopic or macroscopic scale. Such systems are generically referred to as *out-of-equilibrium*, and their description requires theoretical tools that go beyond the equilibrium framework.

The simplest out-of-equilibrium situations arise when a system at equilibrium is subjected to a small external perturbation that slightly breaks the equilibrium condition. Because the perturbation is weak, one can linearize around the equilibrium state and study how the system relaxes back. This approach, known as *linear response theory*, links the dynamical response of observables to their equilibrium fluctuations, leading to powerful results such as the fluctuation-dissipation theorem [1].
Other systems, however, are *far from equilibrium*, in the sense that perturbations are so strong that systems may develop phenomena like instabilities and turbulence whose behavior cannot be captured by linear response. These systems do not relax back to equilibrium, and keep violating detailed balance and time-reversal symmetry. Examples include systems that are strongly driven, such as interface growth processes [2], as well as virtually all biological systems.

The focus of this thesis lies within *active matter*, a branch of far-from-equilibrium statistical mechanics concerned with systems composed of many interacting units that consume energy locally to generate non thermal motion. Unlike passive systems, active matter is intrinsically far from equilibrium, with energy conversion and self-propulsion taking place at the level of individual constituents [3]. The modern study of active matter is often traced back to two seminal works published in 1995: the Vicsek model [4] and the Toner-Tu theory [5]. Since then, active matter has become a central topic in statistical physics proving useful in modeling biological systems on a wide range of scales, from bacterial colonies and cellular migration [6–8], to fish schools and mammal herds [9–11].

Among the many phenomena displayed by active matter, *flocking* represents one of the most striking forms of collective behavior, with the aerial displays of starling murmurations [12, 13] being the best known and most spectacular one.
The study of flocking has attracted intense interest among statistical physicists over the past three decades. Using hydrodynamical approaches [14, 15] and agent-based models [4, 16], physicists have identified the symmetries and conservation laws that govern flocking dynamics, revealing the mechanisms underlying collective motion in active matter. A central result is that flocking exhibits a strongly polarized phase characterized by long-range correlations in both velocity and density fields - even in two spatial dimensions - in apparent contrast to the Mermin-Wagner theorem for equilibrium systems. Moreover, flocking is accompanied by distinctive phenomena such as *giant number fluctuations* [7] and *scale free correlations* [12], further highlighting its departure from equilibrium physics.

Since interested in the bulk properties of flocking groups, most of the numerical models utilized to reproduce synthetic data of flocking make use of periodic boundary condition (PBC). This choice minimize finite size effects on the large scale properties of the system and makes computation more feasible. However, this is a rather stringent — and quite unnatural — condition for animal groups, and one would like to implement different microscopic models able to display collective behaviour even in unbounded space with open boundary conditions [17–19]. When removing PBC in the Vicsek model one inevitably faces the disgregation of the flock, since — due to the metric nature of interaction as in the original model — the particles become persistent random walkers as soon as the interparticle distance becomes larger than the interaction range. Moreover, as we will discuss in the next section, the problem persists even when the so-called topological interactions are considered. In order to maintain cohesion and collective behaviour one has to adjust the microscopical model adding further ingredients to the dynamics. This thesis work is indeed dedicated to different aspects of this problem.

While microscopic models of cohesive flocking can be found in the literature since the seminal work of Reynolds [19], little attention has been given so far to detailed studies of models that match the structural signatures of actual flocks observed in the wild. In particular, measures on starling flocks revealed that their pair correlation function lacks signs of internal structure beyond the exclusion scale set by bird size, implying a kind of intermediate behaviour between a liquid and a gas [20]. Indeed, the behaviour of finite flocks in open space domains has been scarcely addressed in the literature, with the exception of their resilience to external perturbations implemented as scattering obstacles [18].

In this thesis, rather than simply designing a model able to produce cohesive and polarized flocks in unbounded domains—a problem already addressed in several previous works—we focus on the physical properties of the finite object that emerges when cohesion is achieved without imposing a strongly ordered internal structure. Motivated by the weakly structured organization observed in natural flocks, we ask how the global static and dynamical properties of

such self-bound active systems are selected: what determines their size and shape, how their stability is maintained over long timescales, and which collective modes govern their large-scale deformations. From this perspective, the central problem is not merely the emergence of cohesion, but the characterization of cohesive, finite, weakly structured flocks as active objects in their own right.

To address these questions, we combine two complementary strategies. In a *direct* approach, we prescribe a minimal Vicsek-like dynamics in which alignment and cohesion are both encoded at the microscopic level, and we then study the finite flocks generated by this dynamics. In an *inverse* approach, we reverse this logic: rather than imposing microscopic rules, agents learn their behavior from local environmental information and simple, biologically motivated objectives. Taken together, these approaches allow us to connect microscopic interaction rules—or, more generally, local behavioral imperatives—to the emergent static and dynamical properties of cohesive flocks in unbounded space.

The thesis is organized as follows.

Chapter 1 Chapter 1 introduces the theoretical and experimental background. We first review the basic concepts of dry active matter, distinguishing scalar active systems from vectorial, aligning ones. We then discuss the Vicsek model as the paradigmatic microscopic model of flocking, focusing on its ordered phase, the spontaneous breaking of rotational symmetry, long-range order in two dimensions, giant number fluctuations, and the hydrodynamic description provided by Toner & Tu theory. The chapter concludes by connecting these theoretical ideas with experimental observations of collective motion, with particular emphasis on starling flocks, topological interactions, scale-free correlations, giant number fluctuations, inertial effects, and the structural signatures that motivate the cohesion problem studied here.

Chapter 2 Chapter 2 develops the direct approach to cohesive flocking in unbounded domains. After reviewing existing strategies to obtain cohesion in open space, we introduce a minimal topological Vicsek-like model in which polar alignment is supplemented by a weak pairwise social attraction acting as a torque on the direction of motion. We analyze this model both theoretically and numerically. The theoretical treatment relies on a mode decomposition of finite flocks and leads, already at Gaussian level, to predictions for their global size and shape fluctuations. We then discuss mode-coupling corrections, the distinction between directed and spontaneous symmetry breaking, and the resulting dynamics of finite cohesive flocks. A central result is that finite flocks may display underdamped collective shape oscillations even though the microscopic dynamics is purely overdamped. We also derive a directly testable prediction for the ratio between the oscillation period and the flock linear size, which depends only on measurable observables. Finally, we compare the model with empirical structural features of natural flocks—including weak positional order and velocity correlations—and briefly discuss how the scaling of flock size is modified by nonlinear social forces.

Chapter 3 Chapter 3 presents the inverse approach to the same cohesion problem. Instead of prescribing explicit Vicsek-like dynamics, we use a multi-agent reinforcement learning framework in which self-propelled agents learn their behavioral policy from local information about their topological neighbors. The learning problem is designed around biologically motivated imperatives: agents are rewarded for maintaining cohesion while avoiding excessive crowding. After introducing the relevant reinforcement-learning tools and our MARL implementation, we show that cohesive polar flocking can emerge from these local objectives alone. Importantly, we also identify a swarming counterexample: when the short-distance crowding penalty is removed, agents remain cohesive but lose polar order. This suggests a possible mechanism distinguishing flocking from swarming within a unified learning framework.

Conclusions In the conclusions, we provide a critical assessment of our results and discuss possible future developments. We also outline potential applications across different fields, including biology, robotics, and bioinformatics.

Chapter 1

Dry active matter

In all active matter systems, particles move either over a dissipative substrate or within a fluid. Birds navigate through the air [12], fish swim in water [9], and bacteria glide over surfaces [6, 8]. When we refer to active matter as *dry*, we assume that the surrounding fluid is stationary, providing only dissipation to the system. This assumption is valid when particles crawl on a surface, are strongly confined between boundaries [21, 22] or operate at high Reynolds numbers [23]. As a consequence, momentum conservation within the flock is broken at the individual level — changes every time a particle modifies its direction — and the motion of particles can be approximated by an overdamped dynamics [11, 12, 17]. Conversely, systems in which momentum transfer to the fluid cannot be neglected are referred to as *wet*, such as real bird flocks and active nematics. In these cases, momentum conservation is restored, by the explicit inclusion of the fluid surrounding the active particles, leading to substantial changes in the resulting physics. This is for instance the case of three dimensional suspensions in the large viscosity limit.

In this thesis, we focus exclusively on *dry active matter*. Accordingly, this chapter will outline the main physical principles and characteristic behaviours of dry active systems. The first part of the chapter discusses the key conceptual and dynamical differences between aligning and non-aligning active matter. To illustrate these ideas, we will briefly review one of the most widely studied minimal models for non-aligning, i.e. *scalar* active matter.
The second part of the chapter is devoted to vectorial (i.e., aligning) active matter, also known as *dry aligning and dilute active matter* (DADAM) [24], in which particles tend to align their direction of motion with that of their neighbours. This alignment mechanism is at the heart of *flocking* phenomena, whereby large groups of self-propelled agents spontaneously form coherent, collectively moving states. We will introduce the principal physical features of the seminal Vicsek Model, a minimal and paradigmatic framework that encapsulates the emergence of polar order in active systems. Subsequently, we will discuss the Toner and Tu theory, a hydrodynamic continuum description for flocking, originally obtained by phenomenological considerations about the symmetries and the conservation laws of the systems.
Finally, the last section of this chapter explores the connection between experimental observations of flocking in natural and synthetic systems. We will highlight how quantitative measurements on bird flocks have refined our understanding of collective motion in animal groups and motivated substantial improvements in the microscopic modelling of the Vicsek-type dynamics [12, 17, 25].

1.1 Scalar vs vectorial active matter

In the study of active matter systems, a central question is how to describe their behavior in the hydrodynamic limit, that is, at long times and large length scales, where microscopic details are coarse-grained into effective fields. This approach, inspired by the success of hydrodynamics in equilibrium statistical mechanics, provides a powerful framework to capture the emergent properties of active matter systems.

Within this framework, active matter can be classified according to the type of field that characterizes its large-scale behavior. When the relevant coarse-grained field is a scalar quantity, the system is referred to as *scalar active matter*. In this case, the order parameter does not carry a direction but instead describes a scalar field, such as the density. These systems are often studied through effective continuum theories for an active scalar field whose dynamics is intrinsically out of equilibrium.

The prototypical examples of scalar active matter are systems of self-propelled particles without alignment interactions, commonly referred to as active Brownian particles (ABPs) [24, 26, 27] or run-and-tumble particles (RTPs) [27, 28]. Despite their lack of orientational order, such systems exhibit striking collective phenomena, most notably motility-induced phase separation (MIPS) [29] —a dynamical instability that drives the spontaneous segregation of particles into dense and dilute phases in the absence of attractive interactions. This nonequilibrium phase separation is a hallmark of scalar active matter and has been extensively investigated both theoretically and numerically [24, 26–28, 30–33].

When aligning interactions are present, the density field alone is no longer sufficient to describe the system at large scales. In this case, an additional hydrodynamic mode must be introduced: a polar vector field that accounts for the average orientation of self-propelled particles. Systems of this type are therefore referred to as *vectorial active matter*.
This description is well suited for systems characterized by the spontaneous breaking of a continuous rotational symmetry, as observed for instance in flocking phenomena, where both the density and the velocity fields display long-range spatial correlations.

In this thesis, we focus on *dry aligning dilute active matter* (DADAM) [24], where *aligning* indicates that particles explicitly adjust their direction of motion to that of their neighbors, and *dilute* refers to the point-like treatment of particles. The latter assumption is admittedly a crude idealization when modelling biological systems, yet it remains useful for regimes far from the jamming transition, where steric interactions and volume exclusion forces can be neglected. One can, however, go beyond the dilute limit by incorporating finite excluded-volume effects between active particles. This extension becomes essential in systems where collective motion arises from the mechanical pressure exerted by neighboring active units, as observed in the coordinated migration of epithelial cells [7, 34].

To provide a more comprehensive understanding of active matter, the following

section is devoted to a detailed discussion of scalar active matter. Among the most prominent collective phenomena in this class, motility-induced phase separation (MIPS) exemplifies how purely repulsive self-propelled particles can undergo spontaneous phase segregation in the absence of attractive forces.

1.2 Dry scalar active matter

As previously discussed, scalar active matter encompasses all interacting and non-interacting systems whose large-scale dynamics can be captured by the evolution of a scalar field, such as the density field [26, 27]. A wide diversity of active particles exists in nature across many length scales, and a large variety of SPPs are now engineered in laboratories, including chemically powered Janus colloids [35], vibrated grains [36], and many others.

Active particles convert energy at the individual level into self-propulsion. Despite their microscopic differences, these systems share the distinctive feature of performing persistent random walks. In contrast with passive random walkers, active particles exhibit a characteristic timescale that separates the ballistic regime at short times from the diffusive regime at long times. This crossover is quantified by the *persistence time* τ and the corresponding average distance traveled during that time, known as the *persistence length* l_p.

The simplest models used to describe scalar active matter are the active Brownian particle (ABP) and run-and-tumble particle (RTP). In both cases, particles move with a constant speed $v = \mu f_p$, where μ is the particle mobility and f_p the constant amplitude of the self-propelling force. While ABPs change direction continuously due to rotational diffusion, characterized by a rotational diffusion coefficient D_r, RTPs move ballistically during their runs and reorient abruptly at discrete *tumbling* events occurring at a constant rate α. For ABPs, the direction of motion therefore changes continuously, and the persistence time in d spatial dimensions is given by $\tau = 1/[(d-1)D_r]$. For RTPs, on the other hand, the persistence time is simply the inverse of the tumbling rate, $\tau = \alpha^{-1}$.

For both ABPs and RTPs, the simplest form of the spatial dynamics reads:

$$\dot{\mathbf{r}}(t) = \mu \mathbf{f}_p(t), \tag{1.1}$$

where $\mathbf{f}_p(t)$ is a stochastic variable with fixed amplitude.

A further extension of these models is provided by the active Ornstein–Uhlenbeck particle (AOUP) model [31, 33, 37], introduced for systems in which the amplitude of the self-propulsion force fluctuates. In this case, particles can move with variable speeds because the self-propulsion force evolves according to an Ornstein–Uhlenbeck process.

Despite their different dynamics and microscopic details, ABPs, RTPs, and AOUPs all display autocorrelation functions for the self-propelling force decaying exponentially with time:

$$\langle f_{p,i}(t) f_{p,j}(0) \rangle = \delta_{ij} \left(\frac{f_p}{d} \right)^2 e^{-t/\tau}, \tag{1.2}$$

where $f_{p,k}$ denotes the k-th spatial component of the self-propelling force in d spatial dimensions. At large scales, all three models—ABPs, RTPs, and AOUPs—exhibit diffusive behavior characterized by an effective diffusion coefficient

$$D_{\text{eff}} = \frac{\mu^2 f_p^2 \tau}{d}. \tag{1.3}$$

For ABPs and RTPs, this expression can be rewritten in terms of the persistence length $l_p = \mu f_p \tau$, yielding $D_{\text{eff}} = l_p^2/(d\tau)$. For AOUPs, on the other hand, one obtains $D_{\text{eff}} = \pi l_p^2/(2\tau)$.

Scalar active matter thus includes systems whose long-time and large-scale behavior is fully captured by the evolution of the scalar density field. In such systems, interactions depend solely on the positions of the active particles and not on their orientations, as in the case of purely attractive or repulsive forces [26, 29, 38]. Another important class of interactions involves forces that act on the magnitude of the self-propulsion velocity but not on its direction [39, 40]. Such interactions can be mediated by chemical signals, as observed in assemblies of cells communicating through *quorum sensing* [41].

1.2.1 Motility induced phase separation

When dealing with systems in which interactions affect only the interparticle positions, the simplest collective behavior that can arise is the condensation of particles, resulting in the breaking of translational uniformity. Such behavior has been observed in numerous experimental realizations [42–44]. Condensation originates from the interplay between attractive, repulsive, and self-propulsion forces.

In the absence of self-propulsion ($f_p = 0$), an equilibrium system with attractive interactions may undergo an equilibrium liquid–gas phase separation. For weak self-propulsion, attractive forces can easily overcome activity, and the expected equilibrium phase separation typically survives. As the self-propulsion force increases, however, the phase-separated region progressively shrinks until activity dominates over attraction, leading to a homogeneous active fluid.

Surprisingly, at even larger propulsion forces, a re-entrant transition into a phase-separated state is observed [29]. The mechanism underlying this transition is known as *motility-induced phase separation* (MIPS), a phenomenon distinct from equilibrium phase separation that does not require attractive interactions between particles. Instead, MIPS can be driven purely by repulsive interactions—contrary to the equilibrium case—and emerges from a feedback mechanism between the particles' tendency to accumulate where they move more slowly and their slowdown at high densities due to collisions and repulsive forces [45]. This is a genuine non-equilibrium feature, and it can be shown that time-reversal invariance is broken when particles collide head-on and get effectively stuck for a time of the order of their persistence time [46].

Many active systems also exhibit interactions that require a more complex hydrodynamic description. This is the case for the well-known Vicsek model (VM) [4], in which interactions between active particles explicitly act on their

direction of motion. In the VM, rotational symmetry is spontaneously broken, and a polar-ordered flocking phase emerges in sufficiently dense systems. The complete hydrodynamic description of this flocking phase requires the inclusion of an orientational field [5, 14]. In this thesis, we will focus on vectorial active systems that display a transition to flocking, and the following section provides a detailed description of the Vicsek model and its main physical properties.

It is worth noting, however, that more recent results challenge the idea that explicit alignment interactions are necessary to observe orientational order. In [47] the authors show how ABPs undergoing MIPS can rearrange into large polarized domains inside the bulk of the cluster even without an explicit alignment term in the microscopic dynamics. In this setup, partial alignment is observed inside the domains, however without global polarization.

1.3 The Vicsek Model

Active matter is said to be *vectorial* when *aligning* interactions come into play. The prototypical example of vectorial active matter is provided by DADAM [24], and for clarity we briefly recall its definition. DADAM stands for *Dry Aligning Dilute Active Matter* and, together with the Vicsek model (VM), it encompasses two other main classes of systems: self-propelled rods and active nematics. These three models can be distinguished by the nature of their alignment interactions and by their underlying symmetries.

In the Vicsek model, active particles align *ferromagnetically*, while in the cases of self-propelled rods and active nematics, they align *nematically*, meaning that the interaction is invariant under a rotation of angle $\alpha = \pi$. Moreover, whereas self-propelled rods move in a polar fashion, active nematics can spontaneously reverse their direction of motion with a finite probability rate. As a consequence, the symmetry of the alignment interaction determines the nature of the emergent orientational order: the VM exhibits polar order, while the other two classes can display either nematic or local polar order depending on the specific parameters of the system.

In this thesis, we will focus exclusively on the Vicsek model and some of its variations. In the following, the model will be presented in detail together with its distinctive properties. Particular attention will be given to the ordered phase that emerges in systems belonging to the Vicsek universality class, for which a hydrodynamic description will also be discussed.

1.3.1 The microscopic model

The Vicsek Model (VM) is perhaps the simplest model exhibiting a transition to a polar ordered phase and plays a pivotal role in the study of DADAM, analogous to the role of the Ising model in equilibrium ferromagnetism. Its remarkably simple dynamical rule has made it the foundation for numerous variants and extensions, which have been employed to investigate a wide range of collective phenomena in active matter [17, 18, 48, 49].

The VM was first introduced in 1995 through the pioneering work of Vicsek and co-workers [4]. Since then, extensive numerical and theoretical studies have established its central importance as a minimal model for understanding collective motion and spontaneous symmetry breaking in active systems [14, 15, 50].

The model describes the *overdamped* dynamics of N self-propelled particles, each characterized by its position $\mathbf{r}_i^t$ and direction of motion $\mathbf{s}_i^t$, with $|\mathbf{s}_i^t| = 1$. Here, i labels the particles ($i = 1, \ldots, N$) and t denotes the discrete time step. All particles move with the same constant speed v_0, according to the discrete-time dynamics:

$$\mathbf{r}_i^{t+1} = \mathbf{r}_i^t + v_0\, \mathbf{s}_i^{t+1}, \tag{1.4}$$

which is said to be *synchronous*, meaning that all particles' positions and velocities are updated simultaneously at each discrete time step.

Throughout this thesis, we will often refer to the orientation vector $\mathbf{s}$ as the *velocity*, since $\mathbf{v}$ and $\mathbf{s}$ differ only by the constant multiplicative factor v_0. Moreover, because systems considered in this work are explicitely two-dimensional, or, as we will argue, quasi two dimensional due to the role played by gravity in three-dimensional setups, we will often focus on the bidimensional case, where the velocity of each active particle can be parametrized by a single angle θ.

In the VM, particles tend to mimic the behavior of their *local* neighbors: the i-th particle aligns its direction of motion with the average direction of all particles (including itself) within a circular neighborhood $\mathcal{S}_i$ of radius R_0 centered on particle i. To prevent perfect alignment, a noise term is introduced, playing a role analogous to temperature in equilibrium systems.

In two spatial dimensions, the equation governing the evolution of the orientation reads:

$$\theta_i^{t+1} = \arg\left(\sum_{j\sim i} \mathbf{s}_j^t\right) + \eta\, \xi_i^t, \tag{1.5}$$

where θ_i^t is defined such that $\mathbf{s}_i^t = (\cos\theta_i^t, \sin\theta_i^t)$. The sum runs over all neighbors j of particle i, including i itself to avoid indeterminacy when no neigbours are present within $\mathcal{S}_i$. The term ξ_i^t is an uncorrelated white noise with zero mean, uniformly distributed in $[-\pi, \pi]$, and amplitude $\eta \in [0, 1]$.

Because of the choice of neighbors, this model is often referred to as *metric*, since interactions are defined through a metric notion of distance. Other definitions of neighborhood are also possible and will be discussed later in this work [17, 18].

It is worth noting that, without loss of generality, one can set $\Delta t = R_0 = 1$, so that the behaviour of the model depends only on three *control parameters*: the noise amplitude η, the particle speed v_0, and the global particle density $\rho_0 = N/V$, where V denotes the system volume. For the sake of clarity, a simple cartoon describing the alignment dynamics of Vicsek particles is presented in Fig.1.1.

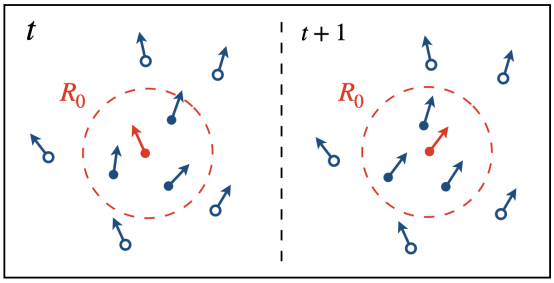

Figure 1.1: **Cartoon of the alignment mechanism in the VM** Particles align their direction of motion to the average direction of the neighbours in the sphere with metric range R_0. Figure adapted from [13].

1.3.2 The Vicsek class

In this section, the essential features that define the so-called *Vicsek universality class* are discussed explicitly.

Spontaneous breaking of a continuous rotational symmetry

The equations of motion for active particles—namely Eqs. (1.4) and (1.5)—are isotropic in both space and time, in the sense that no preferred direction is prescribed a priori. However, Eq. (1.5) includes an explicit polar alignment term which, when the noise amplitude is sufficiently low, allows the system to develop global orientational order. This order can be quantified through a *polar order parameter* defined as:

$$\boldsymbol{\phi}(t) = \frac{1}{N}\sum_{i=1}^{N} \mathbf{s}_i^t, \tag{1.6}$$

which is directly analogous to the total magnetization in spin systems. The stationary time average of its modulus, $\Phi = \langle|\boldsymbol{\phi}(t)|\rangle_t$, is then used to characterize *spontaneous symmetry breaking*: one finds $\Phi \approx 1$ in the collectively ordered phase, while it vanishes in the disordered phase, where the sum of N random vectors scales as $\Phi \sim 1/\sqrt{N}$.

No direction is favored a priori; instead, the orientation of the ordered phase is determined spontaneously by fluctuations, with equal probability over the full 2π range. For this reason, the transition to collective motion arises as a consequence of the spontaneous breaking of a continuous rotational symmetry. Symmetry breaking, however, may also be directed by external cues or by some a priori knowledge of the group target (e.g. a known foraging site). Cell motility, for instance, is known to be sensitive to a wide range of chemical, electrical and mechanical origin [51], and the signatures about the directed or spontaneous nature of symmetry breaking are discussed in [52].

Self-propulsion and local alignment

Unlike equilibrium spin systems such as the XY model, active particles are self-propelled and move according to Eq. (1.4), with velocities subject to stochastic

fluctuations. Since the interaction radius is small compared to the system size, the neighbors of each particle change continuously in time. This feature drives active matter far from equilibrium and it is responsible for its distinctive collective behavior, most notably, the emergence of long-range order (LRO) even in two dimensions, in contrast with the Mermin–Wagner theorem that forbids LRO in equilibrium systems with continuous symmetries [53].

Conservation laws

In the VM, the only conserved quantity is the total number of particles N: particles move but are neither created nor destroyed. Relaxing this condition — for instance, by allowing the global density to fluctuate around a given mean value — modifies the system's phenomenology and changes its universality class. Such systems, where density is not conserved, have been studied in Ref. [54] and are referred to as *Malthusian flocks*. As a dry system, the VM lacks momentum conservation. The surrounding medium acts as a *momentum sink*, providing friction to the moving particles. Consequently, Galilean invariance is broken: there exists a preferred reference frame for the dynamics, corresponding to the one in which the dissipative substrate is at rest.

1.3.3 Physical properties of the VM

Phase diagram

As previously stated, the transition from disorder to polar order in the VM can be characterized in terms of three control parameters: the noise amplitude η, the particles' speed v_0, and the global density ρ_0. Polar order in the VM emerges from the interplay between noise and alignment, the latter being effectively controlled by the local density of particles: the denser the system, the greater the number of neighbors contributing to the local mean velocity. For large noise amplitudes and low densities, the active particles behave essentially as *persistent random walkers*, and the system remains in the *disordered gas* phase. For sufficiently low noise amplitudes, or equivalently for large enough densities, the alignment term dominates over the noise, and the system undergoes a spontaneous breaking of its continuous rotational symmetry, resulting in *global polar order*, with a finite order parameter ($\Phi \sim 1$), see for instance the schematic phase diagram presented in Fig.1.2(a).

The ordered and disordered phases are separated by a coexistence region which, for the polar symmetry of the Vicsek universality class, manifests as dense, ordered bands traveling through a low-density disordered gas as one can see in Fig.1.2(b). These bands extend transversely to the mean direction of motion, and their number grows linearly with both the longitudinal system size and the global density. This (micro-)phase separation arises from the coupling between local density and local order induced by particle motion: particles moving within the system tend to accumulate in denser regions, enhancing local alignment. This positive feedback mechanism generates a long-wavelength instability, destabilizing the ordered phase along the longitudinal (w.r.t. the mean direction of motion) direction and leading to phase separation [55, 56]. The two lines delimiting this coexistence region meet at the origin and converge

as $\rho_0 \to \infty$. They can be interpreted as the *binodal* lines of a liquid-gas-like phase separation. Unlike equilibrium liquid–gas transitions, however, the critical point is effectively sent to infinity, since the rotational symmetry of the gas is spontaneously broken in the ordered phase and, as a consequence, it is impossible to move smoothly between the disordered and ordered phase.

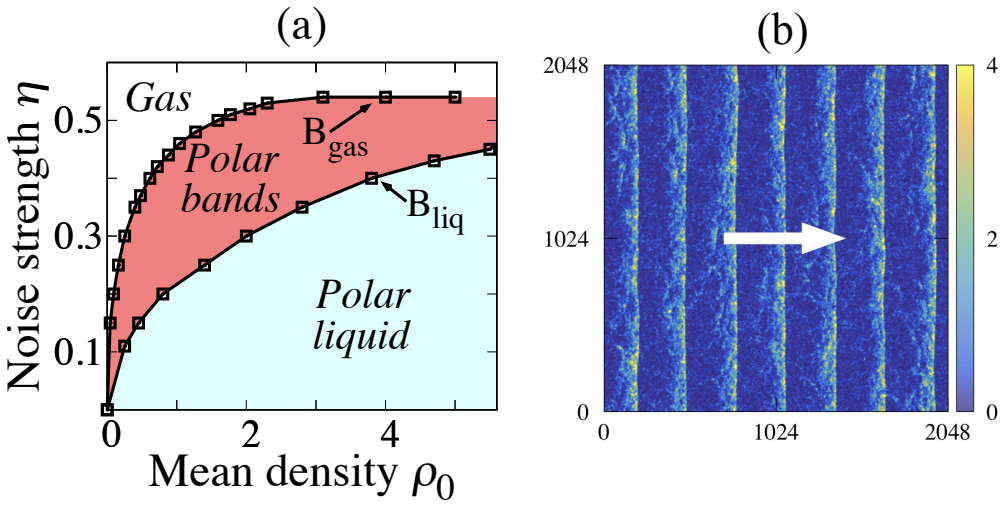

Figure 1.2: **Schematic phase diagram of the Vicsek classes in the plane** (ρ_0, η) **(a)** Phase diagram of the VM with the binodal lines B_{gas} and B_{liq}. **(b)** Snapshot of traveling bands in the microphase separation of the VM. Color encodes the density of particles. Figure reproduced from [24].

Long range order in d=2

An important and non-trivial property of the ordered phase of the VM is that it exhibits *long-range order* (LRO) even in two spatial dimensions, meaning that true collective motion arises in $d = 2$, in contrast to equilibrium systems. At first glance, this seems to contradict the Mermin–Wagner (MW) theorem, which states that no equilibrium system in $d = 2$ can achieve LRO by spontaneously breaking a continuous symmetry. For instance, the XY model in $d = 2$ can only exhibit a weaker form of order, namely *quasi long-range order* (QLRO), characterized by an order parameter that decays algebraically with system size, $\langle \phi \rangle \sim L^{-\eta(T)/2}$ with $\eta(T) \leq 1/4$. In this case, no true order exists asymptotically, but a remnant can be observed in the algebraic decay of the spin–spin correlation function. This type of phase transition is known as a Kosterlitz–Thouless transition [57].

The apparent contradiction is resolved by noting that the MW theorem applies only to equilibrium systems, whereas the VM is inherently out of equilibrium. The self-propulsion of particles allows for more efficient propagation of orientational information, bypassing the restrictions imposed by MW. The following heuristic argument [13, 58], due to John Toner, illustrates this phenomenon.

Let's consider first an XY model in d spatial dimensions. All spins point in the same direction, $\langle \mathbf{s} \rangle$, except for a single spin whose orientation deviates by

an angle $\delta\theta_0$. How does this misalignment evolve on the lattice? In a ferromagnetic system, the misalignment cannot simply vanish but instead spreads out diffusively over neighboring sites, following

$$\partial_t \delta\theta \sim \nabla^2 \delta\theta. \tag{1.7}$$

After a time τ, the original error spreads over a distance $l \sim \sqrt{\tau}$, corresponding to a volume $V_e \sim \tau^{d/2}$. Since the total error in this volume is conserved, the misalignment per spin decreases as $\delta\theta \sim \delta\theta_0/V_e \sim \delta\theta_0 \tau^{-d/2}$.

Noise continuously produces new local misalignments. In a propagation volume V_e, the number of misalignments grows as $n_e \sim \tau V_e \sim \tau^{1+d/2}$. By the central limit theorem, their combined root-mean-square is $\Omega \sim \sqrt{n_e} \sim \sqrt{\tau V_e}$. Therefore, the total error amplitude per spin scales as

$$\Delta\theta \sim \frac{\Omega}{V_e} \sim \sqrt{\frac{\tau}{V_e}} \sim r^{1-d/2} \longrightarrow \begin{cases} 0 & d > 2, \\ \infty & d < 2, \\ \ln L & d = 2. \end{cases} \tag{1.8}$$

For $d > 2$, Eq. (1.8) predicts that fluctuations per spin decay algebraically with distance, indicating that the system is robust to perturbations and exhibits LRO. Conversely, for $d < 2$, fluctuations grow algebraically with distance, preventing the emergence of LRO. The $d = 2$ case is marginal: the algebraic exponent is zero, but fluctuations diverge logarithmically with the system size L (to compute the logarithmic divergence, with system size, a slightly more refined argument is needed, see for instance [59]). In this scenario, fluctuations are unbounded but grow extremely slowly, leading to QLRO.

On the other hand, in the VM orientation fluctuations are coupled to motion. They induce a separation between particles of order $\delta x_\perp \sim v_0 \tau \sin\Delta\theta$ in the direction transversal to the mean direction of motion, and $\delta x_\parallel \sim v_0 \tau (1 - \cos\Delta\theta) \sim \tau \delta\theta^2$ in the longitudinal one. We therefore have two different mechanisms competing for the transportation of orientation information: particle motion and standard diffusion. One can decompose the propagation volume into its transversal and longitudinal directions ($V_e \sim w_\perp^{d-1} w_\parallel$):

$$w_\perp \sim \delta x_\perp + D_\perp \tau^{1/2} \sim \tau\Delta\theta + D_\perp \tau^{1/2} \dot{\sim} \tau^{\gamma_\perp} \tag{1.9}$$

$$w_\parallel \sim \delta x_\parallel + D_\parallel \tau^{1/2} \sim \tau\Delta\theta^2 + D_\parallel \tau^{1/2} \dot{\sim} \tau^{\gamma_\parallel}, \tag{1.10}$$

and the error per spin is given by the square root of the total number of errors over the spreading volume:

$$\Delta\theta \sim \frac{\tau^{1/2}}{\sqrt{w_\perp^{d-1} w_\parallel}} \dot{\sim} \tau^{\gamma}. \tag{1.11}$$

Solving simultaneously the three equations (1.9) - (1.11), where we have introduced the three exponents γ, $\gamma_\perp$ and $\gamma_\parallel$, one gets a system in the three

unknown exponents:

$$2\gamma = 1 - \gamma_{\parallel} - (d-1)\gamma_{\perp} \tag{1.12}$$

$$\gamma_{\perp} = \max\left[1 + \gamma, \frac{1}{2}\right] \tag{1.13}$$

$$\gamma_{\parallel} = \max\left[1 + 2\gamma, \frac{1}{2}\right] \tag{1.14}$$

The solution of the system depends on the dimension, so for $d \geq 4$ one has:

$$\gamma = \frac{1}{2} - \frac{d}{4}, \tag{1.15}$$

$$\gamma_{\perp} = \gamma_{\parallel} = \frac{1}{2}, \tag{1.16}$$

which means that above the upper critical dimension $d_c = 4$ the system is diffusive and $\gamma < 0$.
For $7/3 \leq d < 4$ transversal propagation is superdiffusive:

$$\gamma = \frac{3 - 2d}{2(d+1)}, \tag{1.17}$$

$$\gamma_{\perp} = \frac{5}{2(d+1)}, \tag{1.18}$$

$$\gamma_{\parallel} = \frac{1}{2} \tag{1.19}$$

and $\gamma < 0$ holds again. For $d < 7/3$ both directions display superdiffusive behaviour:

$$\gamma = \frac{1 - d}{d + 3}, \tag{1.20}$$

$$\gamma_{\perp} = \frac{4}{d+3}, \tag{1.21}$$

$$\gamma_{\parallel} = \frac{5 - d}{d + 3} \tag{1.22}$$

which gives $\gamma < 0$ in any dimension $d > 1$. This means that orientation fluctuations are suppressed on large scales and, as consequence, the VM displays LRO in any dimension $d > 1$. Below the upper critical dimension, particles motion dominates over diffusion. This is related to what is called *breakdown of linearized hydrodynamics* and will be discussed more rigorously in 1.4.2, via a dynamical renormalization group (DRG) analysis of the hydrodynamic equations of Vicsek universality class, first obtained by Toner & Tu [5, 14, 15, 50] by symmetry arguments. It is also worth noticing that in general it holds that $w_{\perp} \gg w_{\parallel}$ meaning that fluctuations propagate much faster in the transversal direction w.r.t. the longitudinal one. This spatial anisotropy is due to the symmetry breaking: once a direction is picked up, spatial isotropy is broken and longitudinal and transverse directions may even show different scaling properties. However, we will show how recent results obtained for the original Vicsek class suggests this is not the case and spatial scaling is isotropic.

Toner & Tu phase

The polar ordered phase of the Vicsek class is referred to as *Toner & Tu phase*, after the authors of the pioneering papers about the hydrodynamics of VM [5, 14]. By spontaneously breaking a continuous symmetry the ordered phase exhibits long range correlations (i.e. decaying algebrically) of the velocities. Moreover, because of the coupling between orientation and local density, also density-density and connected correlation functions show an algebraic decay:

$$C_v(\mathbf{r}) = |\mathbf{r}_\perp|^{2\chi} f_v\left(\frac{r_\parallel}{|\mathbf{r}_\perp|^\xi}\right), \tag{1.23}$$

$$C_\rho(\mathbf{r}) = |\mathbf{r}_\perp|^{\alpha} f_\rho\left(\frac{r_\parallel}{|\mathbf{r}_\perp|^\xi}\right), \tag{1.24}$$

where the roughness exponents χ, α, the anisotropy exponent ξ and the functions f_v, f_ρ are universal. Due to this algebraic decay, fluctuations for the Vicsek class are said to be *scale-free* in the ordered phase.

Giant number fluctuations

As an important consequence of the anomalous scaling of fluctuations we have a phenomenon called giant number fluctuations (GNF) [7]. GNF means that, taking boxes of linear size l, with a mean number of particles $\langle n\rangle = \rho_0 l^d$, the root mean square fluctuations $\Delta n \equiv (\langle n^2\rangle - \langle n\rangle^2)^{1/2}$ scales as:

$$\Delta n \sim \langle n\rangle^\alpha, \text{ with } \alpha > 1/2. \tag{1.25}$$

For equilibrium systems, away from the critical point, in general $\alpha = 1/2$, but numerics [7] show that $\alpha \approx 0.8$ in the entire *Toner & Tu phase*, for both $d = 2$ and $d = 3$, meaning that fluctuations in the number of particles are anomalously large, due to the power-law decay of correlations.
A slow enough decay in space of local density fluctuations $\delta\rho(\mathbf{r}, t)$ correlations corresponds indeed to an algebraic divergence at small frequencies $\mathbf{q}$ in Fourier space

$$S(\mathbf{q}, t) \equiv \langle \delta\hat{\rho}(\mathbf{q}, t)\delta\hat{\rho}(-\mathbf{q}, t)\rangle \sim q^{-\sigma}, \text{ for } q \to 0, \tag{1.26}$$

where $q = |\mathbf{q}|$. For systems without power-law decay of correlations $\sigma = 0$. The small frequency behaviour of the stationary density structure factor $S(\mathbf{q})$ gives indeed the fluctuations to mean ratio in the limit of large particles number

$$S(\mathbf{q} \to 0) = \rho_0 \left[\frac{\Delta n^2}{\langle n\rangle}\right]_{n\to\infty}. \tag{1.27}$$

Here again $\langle n\rangle = l^d\rho_0$, with l being the linear size of the boxes and, transforming back from Fourier space, we get $S(\mathbf{q} \to 0) \sim q^{-\sigma} \sim l^\sigma$, which means that

$$\Delta n \sim \langle n\rangle^{1/2+\sigma/(2d)}. \tag{1.28}$$

Comparing with (1.25) we then find

$$\alpha = \frac{1}{2} + \frac{\sigma}{2d}, \tag{1.29}$$

where one recovers the equilibrium result $\alpha = 1/2$ when $\sigma = 0$, as we would expect from the central limit theorem. The above simplified argument assumes spatial isotropy of correlation functions (and of the corresponding structure factors). However, due to symmetry breaking, spatial isotropy is broken and correlation functions may show different algebraic decays in the transversal and longitudinal directions. In this case, σ and thus α are determined from the leading contribution once one averages over all directions.

1.4 Hydrodynamic theory of the Toner & Tu phase

To give a full hydrodynamic description of VM we first need to identify the relevant fields associated with symmetries and conservation laws. These are said to be *slow fields*, since they vary slowly in space and time and their behaviour determines the dynamics of the system for sufficiently large time scales. We pick the density field ρ, associated with the conservation of the number of particles and the velocity field $\mathbf{v}$ which is associated with the spontaneous breaking of continuous rotational symmetry.
The first step in obtaining the hydrodynamic equations is to write the equations for the slow fields in terms of a gradient expansion, keeping only the terms compatible with the underlying symmetries and conservation laws and disregarding all higher order contribution, since we are interested in the hydrodynamic limit. Terms of order n in the gradients carry a corresponding weight $\sim q$ in momentum space (here q indicates a wavenumber), so that for $q \to 0$ (large wavelengths) higher order terms are irrelevant and they can be discarded as they only describe short-ranged non-universal features. The equations for the two continuous and coarse grained slow fields $\rho(\mathbf{r}, t)$ and $\mathbf{v}(\mathbf{r}, t)$ together give a hydrodynamic description of the ordered phase of the Vicsek flocks, the so called Toner & Tu Theory of flocking [5]. They come only from symmetry considerations and, in the long-wavelength limit read

$$\partial_t \rho + \nabla \cdot (\rho \mathbf{v}) = 0 \tag{1.30}$$

$$\begin{aligned} \partial_t \mathbf{v} + \lambda_1 (\mathbf{v} \cdot \nabla)\mathbf{v} + \lambda_2 (\nabla \cdot \mathbf{v})\mathbf{v} + \lambda_3 \nabla(|\mathbf{v}|^2) \\ = \mu \mathbf{v} - \beta |\mathbf{v}|^2 \mathbf{v} - \nabla P_1 - (\mathbf{v} \cdot \nabla P_2)\mathbf{v} \\ + D_1 \nabla(\nabla \cdot \mathbf{v}) + D_L \nabla^2 \mathbf{v} + D_2 (\mathbf{v} \cdot \nabla)^2 \mathbf{v} + \mathbf{f}. \end{aligned} \tag{1.31}$$

Equation (1.30) expresses the conservation of the particles density (particles can never die or be born during flight), while (1.31) is a sort of Navier-Stokes equation where galileian invariance is broken and a *mexican hat potential* term promotes the spontaneous symmetry breaking. The $\lambda_{1,2,3}$ terms are convective terms allowed by the lack of galileian invariance, which would otherwise enforce $\lambda_1 = 1$ and $\lambda_2 = \lambda_3 = 0$. Coefficients μ and β come from the mexican hat potential $U(\rho, |\mathbf{v}|) = -\frac{\mu}{2}|v|^2 + \frac{\beta}{4}|v|^4$ and account for a force $\mathbf{F} = (\mu - \beta|\mathbf{v}|^2)\mathbf{v}$ that induces the spontaneous breaking of the continuous rotational symmetry, allowing for a positive finite speed in the polar ordered phase $|\mathbf{v}| = v_0 = \sqrt{\mu/\beta}$. While $\beta > 0$, we have $\mu < 0$ in the disordered phase and $\mu > 0$ in the ordered

one. We then have the pressure terms (that in general are function of the density ρ and the magnitude of the velocity $|\mathbf{v}|$) accounting for both *isotropic* (P_1) and *anisotropic* (P_2) pressure, that can be written as a series expansion in the density fluctuations $\delta\rho(\mathbf{r},t) = \rho(\mathbf{r},t) - \rho_0$ w.r.t. the global density ρ_0:

$$P_1 = \sum_{n=1}^{\infty} \sigma_n(|\mathbf{v}|)(\delta\rho)^n, \quad P_2 = \sum_{n=1}^{\infty} \sigma_n^A(|\mathbf{v}|)(\delta\rho)^n. \tag{1.32}$$

The terms $D_{1,2,L}$ are diffusion coefficients accounting for the spreading out of fluctuations due to the presence of the aligning interactions. Here all phenomenological convective and viscous coefficients, as well as the two symmetry-breaking ones can in principle depend on ρ and $|\mathbf{v}|$.
Lastly, the term $\mathbf{f}$ in (1.31) represents a zero average additive noise, delta-correlated in space and time with variance Γ:

$$\langle f_i(\mathbf{r},t) f_j(\mathbf{r}',t')\rangle = \Gamma\delta(\mathbf{r}-\mathbf{r}')\delta(t-t'). \tag{1.33}$$

1.4.1 Linearized TT theory

In the absence of fluctuations, Eqs. (1.30) and (1.31) admit a homogeneous steady-state solution $\rho(\mathbf{r},t) = \rho_0$, $\mathbf{v}(\mathbf{r},t) = v_0\hat{e}_\parallel$, where the subscripts $\parallel$ denotes, as previously stated, the longitudinal ($\perp$ the transversal) direction w.r.t. the mean direction of motion. The value v_0 is determined by the condition

$$\mu v_0 - \beta v_0^3 = 0. \tag{1.34}$$

For $\alpha > 0$, in the polar ordered phase, $v_0 = \sqrt{\mu/\beta}$, with the direction $\hat{e}_\parallel$ randomly selected by the spontaneous breaking of the continuous symmetry. In the ordered phase, following [5, 15, 60], we proceed by linearizing Eqs. (1.30) and (1.31) around the homogeneous solutions

$$\rho(\mathbf{r},t) = \rho_0 + \delta\rho(\mathbf{r},t) \tag{1.35}$$
$$\mathbf{v}(\mathbf{r},t) = [v_0 + \delta v(\mathbf{r},t)]\hat{e}_\parallel + \mathbf{v}_\perp(\mathbf{r},t), \tag{1.36}$$

where $\mathbf{v}_\perp(\mathbf{r},t)$ measures velocity fluctuations transversal to the mean direction of motion. In the TT phase, the longitudinal velocity fluctuations $\delta v_\parallel$ are a fast mode enslaved to the unperturbed theory $\mathbf{v}_\perp$ and $\delta\rho$. Thus, they can be eliminated from the from Eqs. (1.30) and (1.31) to yield the linearized hydrodynamics

$$\begin{aligned}\partial_t\delta\rho + \rho_0\nabla_\perp\cdot\mathbf{v}_\perp + v_2\partial_\parallel\delta\rho - \rho_0\mu_2\partial_t\partial_\parallel\delta\rho \\ = D_{\rho_\parallel}\partial_\parallel^2\delta\rho + D_{\rho_\perp}\nabla_\perp^2\delta\rho + D_{\rho v}\partial_\parallel(\nabla_\perp\cdot\mathbf{v}_\perp)\end{aligned} \tag{1.37}$$

and

$$\begin{aligned}\partial_t\mathbf{v}_\perp = -\gamma\partial_\parallel\mathbf{v}_\perp - \frac{c_0^2}{\rho_0}\nabla_\perp\delta\rho + D_B\nabla_\perp(\nabla_\perp\cdot\mathbf{v}_\perp) \\ + D_v\nabla_\perp^2\mathbf{v}_\perp + D_\parallel\partial_\parallel^2\mathbf{v}_\perp + g_t\partial_t\nabla_\perp\delta\rho + g_\parallel\partial_\parallel\nabla_\perp\delta\rho + \mathbf{f}_\perp\end{aligned}. \tag{1.38}$$

All the constants introduced in the above expressions can be expressed as functions of the phenomenological constants appearing in Eqs. (1.30) and (1.31), their precise expressions can be found alongside a detailed linearization procedure, in [60]. The above equations can be solved in Fourier space, where

$$\begin{aligned}\hat{\mathbf{v}}_\perp(\mathbf{q},\omega) &\sim \int d\mathbf{r}dt\, e^{-i(\mathbf{q}\cdot\mathbf{x}-\omega t)}\mathbf{v}_\perp(\mathbf{r},t)\,,\\ \delta\hat{\rho}(\mathbf{q},\omega) &\sim \int d\mathbf{r}dt\, e^{-i(\mathbf{q}\cdot\mathbf{x}-\omega t)}\delta\rho(\mathbf{r},t)\,.\end{aligned} \tag{1.39}$$

If we carry out the calculations as done in [60], we get the leading order in the wave vector $\mathbf{q}$ of the linearized structure factor that tells us that both the density and velocity equal time autocorrelation functions scale as

$$S_\rho(\mathbf{q}) \sim S_v(\mathbf{q}) \sim q^{-2}, \tag{1.40}$$

predicting no LRO at the linear level in the TT phase alongside GNF in $d = 2$.

Furthermore linearizing the system near the onset of collective motion, one can see that the homogeneous solution for the ordered phase is unstable w.r.t. small spatial perturbations in the direction longitudinal to the mean direction of motion. This instability is indeed driven by the ρ dependence of the linear Ginzburg-Landau linear coefficient μ [56]. This mechanism describes the linear instability (i.e. the spinodal line) leading to the emergence of the band structure discussed above. Its full description, however, can only be obtained by means of a non-linear theory [61].

1.4.2 Non-linear TT theory

Nonlinear terms, ignored in the linearized approach, are known to be relevant in $d < d_c = 4$ [14, 15] and can be accounted for by a dynamical renormalization group (DRG) analysis [62]. The DRG procedure is carried out in the transversal direction and consists of two steps. First, we average nonlinear equations of motion over the short wavelength fluctuations (i.e. we average over the slow fields Fourier modes) with wave vector lying in in the hypercylindrical shell of Fourier space $b^{-1}\Lambda \leq q_\perp \leq \Lambda$. Λ represents here the *ultraviolet cut-off* - determined by the inverse of the microscopic interaction range - and $b > 1$ is an arbitrary rescaling factor. The second step consists of restoring the ultraviolet cut-off to Λ. This is done rescaling the transversal distance $r_\perp = |\mathbf{r}_\perp|$ and wave numbers as

$$r_\perp = br'_\perp, \quad q_\perp = b^{-1}q'_\perp. \tag{1.41}$$

Also time, parallel distances and the fields rescale according to

$$r_\parallel = b^\xi r'_\parallel, \quad q_\parallel = b^{-\xi}q_\parallel, \quad t = b^z t', \quad \delta\rho = b^\chi \delta\rho'. \tag{1.42}$$

We get to a new *renormalized* set of equations, where the form is the same as the orginal equations, but their parameters are renormalized. If we denote the collection of the initial parameters of the non-linear equation of motion as $\{\mu_i^{(1)}\}$, we can represent their evolution by the above RG flow

as $\{\mu_i^{(1)}\} \rightarrow \{\mu_i^{(b)}\}$. The exponents ξ, z and χ, known respectively as the *anisotropy*, *dynamical* and *roughness* scaling exponents, are in principle arbitrary. For a suitable choice, however, a renormalization group fixed point (such that the renormalized parameters do not change under DRG process) is obtained, in the limit $b \to \infty$. By analyzing the DRG flow near the latter fixed point we can thus deduce the system scaling properties.
The averaging step has to be performed perturbatively in the equations of motion nonlinearities and generally produces nonlinear corrections - the so called *graphical corrections*- in the DRG flow equations. Unfortunately, the large number of nonlinearities in TT equations makes arduous any exact treatment in the nonlinear DRG fixed point, and indeed no exact values for the TT theory scaling exponents at the nonlinear fixed point where known until recently. Recent high precision numerical simulation of the VM, however, provide good estimates in $D = 2, 3$ [63], which, in two spatial dimensions take values

$$z = 1.33(2), \quad \chi = -0.31(2), \quad \xi = 0.95(2), \tag{1.43}$$

while in $d = 3$ one has

$$z \approx 1.77, \quad \chi \approx -0.62, \quad \xi \approx 1. \tag{1.44}$$

Additionally, [63] provides numerical evidence that the hyperscaling relation

$$z = \zeta = (d-1) + \xi + 2\chi. \tag{1.45}$$

is satisfied. Given the velocity structure factor $S_v\left(q_\perp, q_\parallel, \{\mu_i^{(b)}\}\right)$, we can also deduce qualitatively its scaling behaviour via a naive power counting. The recursive equation for the structure factor then reads

$$S_v\left(q_\perp, q_\parallel, \{\mu_i^{(1)}\}\right) = b^\zeta S_v\left(q_\perp, q_\parallel, \{\mu_i^{(b)}\}\right), \tag{1.46}$$

where we defined ζ in Eq.(1.45) and the scaling of the structure factor has been determined considering that it is given by the Fourier transform of the equal time, real-space velocity correlation function. Now, by choosing the rescaling factor b such that $bq_\perp = \Lambda$ and taking the small wavelength limit we have $\{\mu_i^{(b)}\} \approx \{\mu_i^*\}$. Therefore equation (1.46) can be written in the form

$$S_v\left(q_\perp, q_\parallel, \{\mu_i^{(1)}\}\right) = \left(\frac{q_\perp}{\Lambda}\right)^{-\zeta} S_v\left(\Lambda, \Lambda^\xi \frac{q_\parallel}{q_\perp^\xi}, \{\mu_i^*\}\right). \tag{1.47}$$

If we reabsorb the dependencies on Λ and $\{\mu_i^*\}$ into a suitable function g we can recast equation (1.47) into the form

$$S_v\left(q_\perp, q_\parallel, \{\mu_i^{(1)}\}\right) = q_\perp^{-(d-1+\xi+2\chi)} g\left(\frac{q_\parallel}{q_\perp^\xi}\right). \tag{1.48}$$

At the nonlinear fixed point both the velocity and density structure factor scale as

$$S\left(q_\perp, q_\parallel, \{\mu_i^{(1)}\}\right) \sim q_\perp^{-\zeta}. \tag{1.49}$$

This implies long-range density correlations in real space and leads to anomalously large fluctuations of the number of particles in a region of size L, that is the GNF discussed in Section 1.5.2.

1.4.3 Recent theoretical developments

As we noted, the exact scaling exponents of the symmetry-broken phase of polar flocks have remained rather elusive over the years, due to the large number of diagrammatic corrections that must be computed perturbatively. Under the conjecture that certain nonlinearities are irrelevant in the RG sense, Toner suggested the exact values [5]

$$z = 6/5, \;\; \chi = -1/5, \;\; \xi = 3/5 \tag{1.50}$$

in $d = 2$. This values are however in disagreement with the numerical estimates given in the previous section, so that the latter argument is invalidated and it seems one cannot compute exactly the scaling exponents.

More recent analytical developments [61] suggest that the symmetry broken equation describing the Goldstone mode of the theory should bear a gradient structure due to the required symmetry. At odds with [5, 14, 50, 54, 64], authors in [61] wrote down a generic equation for the dynamics of the hydrodynamics mode directly in the ordered phase, once the symmetry is broken. Notably, its well defined gradient structure preserves the noise vertex from graphical corrections. This immediately implies that the scaling exponents satisfy the hyperscaling relation in (1.45).

This new result can also be reconciled with the original Toner & Tu treatment if one assumes that the Goldstone mode obtained by eliminating the fast variable from the isotropic Toner-Tu equation is not exactly the direction of the velocity field, as one would naively expect. In $d = 2$ one can parametrize the velocity field as $\mathbf{v} = v(\mathbf{r}, t)\mathbf{n}(\phi(\mathbf{r}, t))$ with ϕ being the phase. By eliminating the modulo of the velocity, since it is a fast mode, we find ourselves with two coupled equations for ϕ and $\delta\rho$. It is then possible to recover the gradient structure of [61] starting from TT theory if picking the correct Goldstone mode

$$\tilde{\phi} = \phi - \alpha\partial_\parallel\phi - \beta\delta\rho\partial_\parallel\phi, \tag{1.51}$$

with the detailed expression of the coefficients α, β that can be found in [61]. Furthermore, it is further argued that – at least in $d = 2$ – a generalized Galilean invariance preserves other nonlinear vertex from graphical correction, thus making possible a complete determination of $d = 2$ exponents from simple scaling arguments,

$$z = 4/3, \;\; \chi = -1/3, \;\; \xi = 1, \tag{1.52}$$

These values are indeed in perfect agreement with the ones obtained in [63] (see (1.43)) from large-scale numerical simulations. For completeness, however, we point out that the validity of the latter argument is still a matter of debate [65–68].

1.5 Interaction with experimental observations

Flocking is an emergent collective behaviour displayed by a large number of biological systems, on all length scales. Experimental observation range from *in vitro* reproduction of flocking in confluent epithelial tissues [7] to the observation in the field of gregarious macroscopic animals such as fishes, birds and mammals [25, 69, 70].

The comparison with such experimental observations helped us to better understand the properties of the emergent ordered phase and, in the following we'll briefly review the most influential results for this thesis. In particular, the ones regarding scaling relations measured for starling flocks [20, 25, 69] and confluent tissues of epithelial cells [7] and regarding the internal structure of starling flocks [20, 71].

1.5.1 Topological vs metric interactions

The original Vicsek rule is said to be *metric*, since neighbours are defined as all the particles lying in a sphere with metric range R_0, centred around a given agent. In topological models, instead, one chooses neighbours based on some topological (or metric-free) rule, such as the first n_c nearest neighbours, with a fixed n_c for all SPPs, or the Voronoi neighbours. The latter will be the one used in the following of this thesis and relies on the so called *Delaunay Triangulation*, the dual of Voronoi tessellation, for which two particles are said to be neighbours if their Voronoi cells (i.e. the Voronoi cells centered on particle positions) are adjacent.

This choice is motivated by experimental evidence, gathered for flocks of European starlings observed in the field [69] and for other social vertebrates studied in the lab [72] that interact with a more or less fixed number of neighbours, regardless of local density. In [25] the authors studied the average angular position of nearest neighbours for flocks of birds with different densities, showing a surprising lack of nearest neighbours along the direction of motion of birds, and consequently, a strong anisotropic nature of the interaction. Looking at higher order neighbours, this anisotropy fades away, leading to a basically uniform angular distribution of the n-th nearest neighbour for n sufficiently large, suggesting a finite interaction range, at least for what concerns the anisotropic part of the interaction.

For any given flock we can define an interaction range n_c, that quantifies the order of neighbour such that birds farther than the n_c-th nearest neighbour are distributed homogeneosly. Alongside the order of the neighbour n_c (i.e. the topological distance) we can define also the metric distance r_c of the n_c-th neighbour apart from the reference bird. Changing the density of the flocks, n_c and r_c cannot remain both constant and their behaviour can actually elucidate the nature of the interaction among individual to be rather topologic or metric. The simple idea is the following: if the interaction is metric, then the range r_c should be the same for flocks with different densities and, consequently, the number n_c of neighbours within this range should be larger for denser flocks. Conversely, if the interaction is topologic, the range in unit birds n_c

should be the same, no matter what density we consider and r_c should be larger for sparser flocks. More quantitatively, if we define r_1 as the average nearest neighbour distance, the average distance r of th n-th nearest neighbour grows as $r \sim r_1 n^{1/3}$, that means that the number of individuals in a sphere of radius r, grows as $n \sim r^3$. In the metric scenario r_c is constant so the relation $n_c^{-1/3} \sim r_1$ holds. In the topologic scenario, instead, n_c is constant, so it should hold that $r_c \sim r_1$. Experimental evidence — presented here in Fig.1.3 — showed an evident linear correlation between r_c and r_1 (panel (c)) and no clear relation between n_c and r_1 whatsoever (panel (d)), leading the authors to confirm the hypothesis of the topological nature of the interaction, with an average number of interacting neighbours $n_c = 6.5 \pm 0.9$, with error given by standard error.

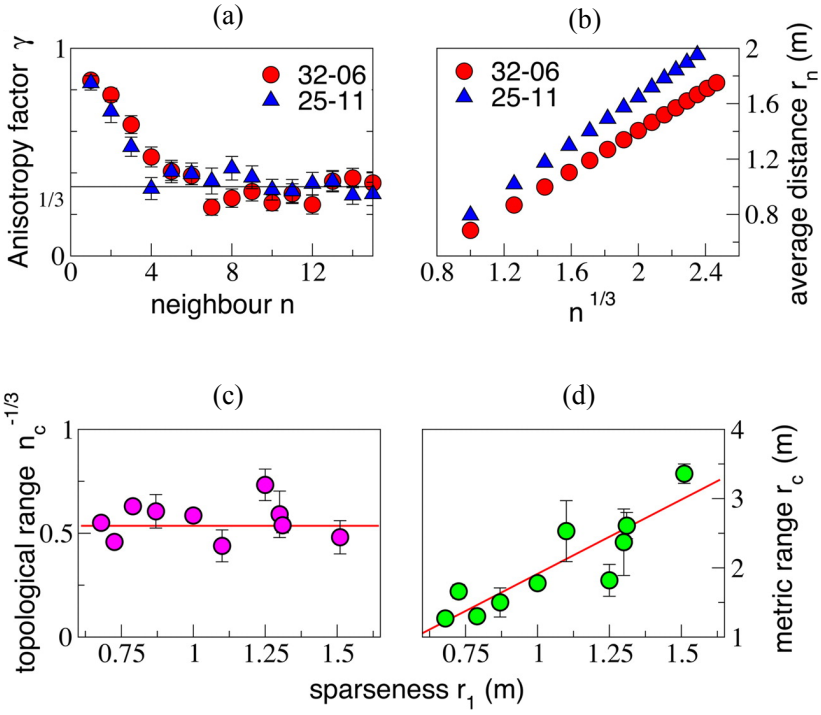

Figure 1.3: **Evidence for topological rather than metric interaction in starling flocks** **(a)** Anisotropy factor γ, that measure to what degree the distrubution of n-th neighbour is anisotropic. $\gamma = 1/3$ means it is isotropic, viceversa for $\gamma > 1/3$ the distribution is anisotropic. Distribution for first nearest neighbours appears to be strongly anisotropic, while it becomes uniform at higher order neighbours. Error bars represent standard error. **(b)** Average distance of the n-th nearest neighbour vs $n^{1/3}$ The slope of the curve is proportional to r_1. **(c)** $n_c^{-1/3}$ as a function of r_1. **(d)** Metric range r_c vs sparsness r_1. Figure reproduced from [25].

This experimental results stimulated the introduction of a topological version of the VM where local neighbours are not selected within a metric range but are rather chosen via neighborhood in a Voronoi rassellation [73]. It will be discussed in details in Section 2.1.

1.5.2 Experimental measures of scaling relations

We recall here some results for scaling relation for experimental setups of *in vivo* realization of cellular collective motion [7] and of starling flocks observed in the field [12]. Given the fluctuation of the velocity of birds w.r.t. the mean direction of motion

$$\mathbf{u}_i = \mathbf{v}_i - \frac{1}{N}\sum_{j=1}^{N} \boldsymbol{v}_j, \tag{1.53}$$

the correlation function of the velocity fluctuations for a flock of N SPPs is defined as

$$C(r) = \frac{1}{C_0}\frac{\sum_{ij} \mathbf{u}_i \cdot \mathbf{u}_j \delta(r - r_{ij})}{\sum_{ij} \delta(r - r_{ij})}, \tag{1.54}$$

where $\delta(r - r_{ij})$ is a smoothed Dirac δ-function and C_0 is a normalisation factor ensuring that $C(r = 0) = 1$. Large values of $C(r)$ imply that fluctuations in particles' direction are nearly parallel and thus, strongly correlated, while negative values represent antiparallel — thus anticorrelated — fluctuations. Moreover, for uncorrelated fluctuations, their average is zero, corresponding to a vanishing correlation function.

To interpret the behaviour of $C(r)$ we introduce the correlation length ξ defined as the zero of the correlation function

$$C(r = \xi) = 0, \tag{1.55}$$

which defines the the size of correlated domains in the flock. In section 1.4 we used ξ to represent a scaling exponent, from now on ξ will be used in this thesis to indicate correlation length.

We can write the leading contribution of the correlation function as

$$C(r) = \frac{1}{\xi^{\gamma}} f\left(\frac{r}{\xi}\right) \tag{1.56}$$

where f is a dimensionless scaling function and γ being a scaling exponent not to be confused with the phenomenological one introduced in Section 1.3.3 [13, 58]. Since the correlation length is linear w.r.t. the system's size L it holds that $\xi(bL) = b\xi(L)$, and, by taking $b = 1/r$ and substituting back into (1.56) we get

$$C(r, L) = r^{-\gamma} f\left(\frac{r}{L}\right). \tag{1.57}$$

To get rid of finite size effects, we take the asymptotic correlation function in the limit $L \to \infty$ and we get a power law behaviour

$$C_{\infty}(r) \sim r^{-\gamma}. \tag{1.58}$$

In starling flocks the correlation length grows linearly with the size L of the flock, meaning that correlations are scale-free: there is no characteristic length scale for correlations between birds. We report in Fig.1.4 some experimental results obtained in [12] for both the velocity and speed correlation functions. To quickly determine the value of the exponent γ, one can take the derivative

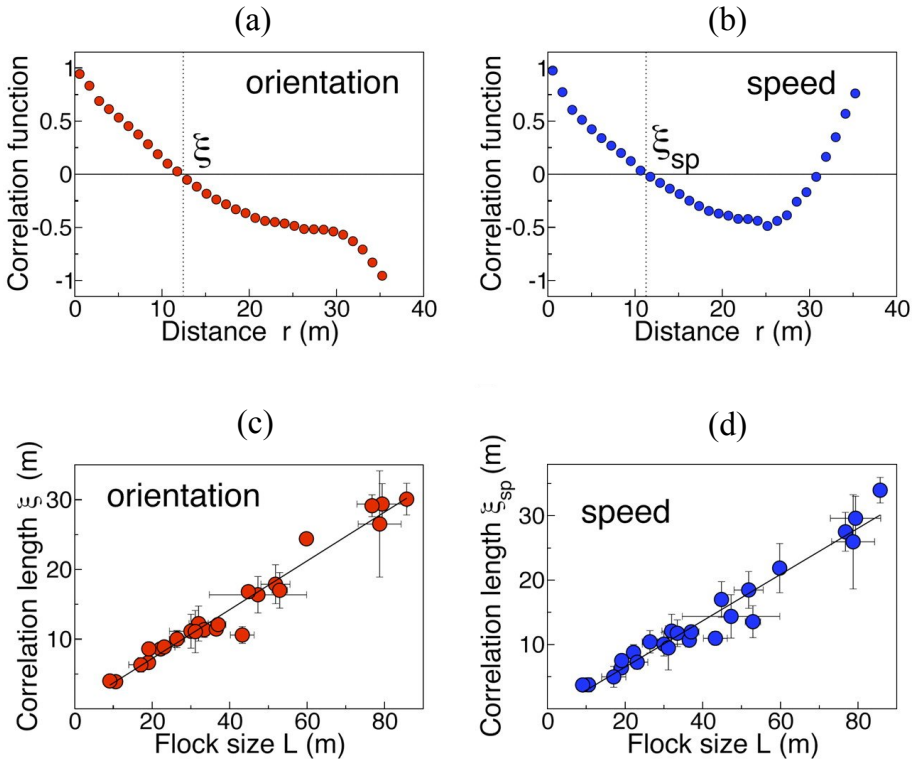

Figure 1.4: **Correlation functions and correlations legnths** **(a)** Normalized correlation function $C(r)$ of the velocity fluctuations. $r = \xi$ gives a spatial scale for correlated domains.**(b)** $C_{sp}(r) = \frac{1}{C^0_{sp}} \frac{\sum_{ij} \phi_i \cdot \phi_j \delta(r - r_{ij})}{\sum_{ij} \delta(r - r_{ij})}$ measures the correlation of the speed fluctuations $\phi_i = \|\mathbf{v}_i\| - \frac{1}{N} \sum_{k=1}^{N} \|\mathbf{v}_k\|$. It is normalized as $C(r)$ and the correlation length ξ_{sp} gives information on the size of speed correlated domains. **(c)-(d)** Correlation length ξ and ξ_{sp} plotted vs the linear size L for different flocks, each of them have been averaged over many time steps and the errors are given by standard deviation. Figure reproduced from [12].

of the finite size correlation function (1.57), w.r.t. the rescaled variable $x = r/\xi$ at the zero of correlation function

$$C'(x = 1) = \xi^{-\gamma} f'(1) \approx -\xi^{-\gamma} \approx -L^{-\gamma}, \tag{1.59}$$

hence the correlation function should flatten at its zero for larger flocks. However, this does not happen, meaning that the exponent γ assumes a rather small value. This means that the asympthotic correlation does not quite decay at all, and therefore behavioural correlations are not only scale free, but also anomalously long ranged.

This results is in contrast with both equilibrium systems, like the Heisenberg model that has $\gamma = 1$ and nonequilibrium theory of flocking, where the exponent predicted by the Toner and Tu theory is $\gamma = 6/5$ in 3D and $\gamma = 2/5$ in 2D. As pointed out in [74] the origin of such an anomalously slow decay of correlation function could be due to a dynamical information inflow from the boundaries of the flock to the bulk, rather than being a non equilibrium feature of the system. Applying a dynamical external field to a portion of spins on the

boundaries of the system results in an exponent $\gamma \approx 0$ that closely resembles the anomalously long ranged behaviour displayed by starling flocks.

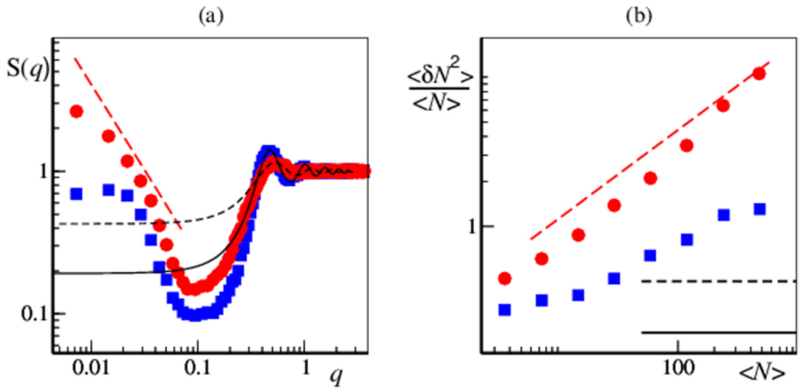

Figure 1.5: **Giant number fluctuations (a)** Red circles: static structure factor for RAB5A monolayer. The dashed black line corresponds to the structure factor for a monodisperse ensemble of hard disks. The marked divergence exhibited by the structure factor for $q \to 0$ is the signature of the presence of giant density fluctuations that are not compatible with equilibrium models. The dashed red line marks the theoretical prediction for flocking systems. The blue squares represent the experimental results for the structure factor of the control monolayer and the bold black line is the structure factor of an equilibrium ensemble of randomly scattered hard disks. For a full description of the parameters used see [7]. **(b)** Normalised mean squared number fluctuations for the control (blue squares) and the RAB5A monolayer (red circles) respectively. The dashed red line marks the theoretical prediction, see (1.61). The horizontal lines represent the asymptotic behaviours expected for large $\langle$N$\rangle$ by assuming the two hard disks models whose static structure factors are shown (with the same line types) in panel (a). Figure reproduced from [7].

Beside the anomalous decay of correlation function observed in real starling flocks, a quantitative agreement with scaling theory has been observed in highly confluent epithelial cell monolayers undergoing a flocking transition to polar order [7]. Epithelial cells are very motile, but they reach a near-jammed state above a critical density. The over-expression of the protein RAB5A, however, can reawaken the cell monolayer promoting the emergence of large scale migratory pattern, thus enabling a transition to a polar ordered phase. In [7] experimental measures of both the density structure factor and the giant number fluctuations (discussed in Section 1.3.3) have been presented. Since we have shown that they are directly related, for the sake of compactness here we mainly discuss the latter. To quantify the GNF one has to quantify the fluctuations

$$\Delta N = N - \langle N \rangle \tag{1.60}$$

in the number of cells contained in a square box of prescribed size, around the mean value $\langle N \rangle$. Experimental results — presented in Fig.1.5 — show that the flocking state is accompanied by GNF, as predicted by TT theory, with a scaling

$$\langle \Delta N \rangle \sim \langle \delta N \rangle^{\alpha} \tag{1.61}$$

with the exponent $\alpha \approx 0.8$ in reasonable agreement with the numerical and theoretical estimates given in Section 1.4.

1.5.3 The inertial spin model

The Vicsek Model can be regarded as an overdamped description of self-propelled particles with alignment interaction, in which both the particles' positions and orientations are updated without any explicit inertial dynamics. The Inertial Spin Model (ISM) [75] was introduced since the VM does not correctly reproduce the way that flocks of birds turn. Experimental analysis suggests that collective turns involve linear propagation of the information of both the direction of motion of birds and their individual trajectory's curvature without any local change in density. The turnings start locally in space and propagate extremely fast and undamped through the group, with a linear dispersion law analogous to superfluid transport [75], see Fig.1.6 for a better visualization. This significantly differs from the VM, where the hydrodynamic theory of flocking predicts propagating sound modes that couple orientational and density disturbances [5, 14, 76]. The main ingredients missing in the microscopic dynamics of the VM accountable for the theoretically reproducibility of the dispersion law observed in turning flocks are two: the presence of a conservation law associated to the system's rotational symmetry and the existence of a behavioral inertia mediating the effect of the social force. The new set of equations of motion reads

$$\frac{d\mathbf{v}_i}{dt} = \frac{1}{\nu}\mathbf{s}_i \times \mathbf{v}_i, \tag{1.62}$$

$$\frac{d\mathbf{s}_i}{dt} = \mathbf{v}_i \times \left[\frac{J}{v_0^2}\sum_j \mathcal{N}_{ij}\mathbf{v}_j - \frac{\eta}{v_0^2}\frac{d\mathbf{v}_i}{dt} + \frac{\boldsymbol{\xi}_i}{v_0}\right], \tag{1.63}$$

$$\frac{d\mathbf{r}_i}{dt} = \mathbf{v}_i. \tag{1.64}$$

In these equations $\mathbf{r}_i$, $\mathbf{v}_i$ and $\mathbf{s}_i$ represents respectively the position, the velocity and the generalized momentum of particle i. ν is a generalized moment of inertia, η a friction coefficient, J the strength of the alignment force to neighbours and $\boldsymbol{\xi}_i(t)$ a zero average, δ-correlated, white noise. $\mathcal{N}$ is the adjacency matrix such that $\mathcal{N}_{ij} = 1$ if particles i and j are neighbours and $\mathcal{N}_{ij} = 0$ otherwise. Interestingly, performing an overdamped approximation — on sufficiently long time scales and large length scales — of the ISM, the VM is recovered, see [77].

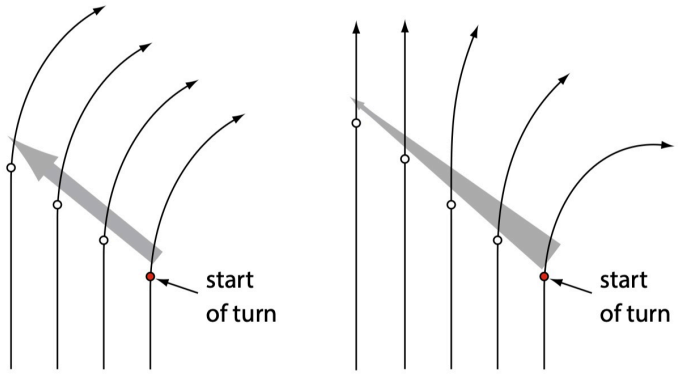

Figure 1.6: **Schematic representation of turning information propagation** Left panel: turning propagation for real flocks. Information gets no attenuation as it propagates trhough the entire flock. Right panel: in the VM turning information is damped. Figure reproduced from [78].

1.5.4 Starling flocks' internal structure

As previously shown in Section 1.5.2, starling flocks exhibit long-range correlations emerging from local interaction, but, due to the self-propelled nature of their constituents, they significantly differs from equilibrium systems. Particles inside a flock do flow, and are characterized by a kind of intermediate behaviour between liquid and gas. Moreover, the reshuffling of neighbours due to self-propulsion of particles is also responsible for the information transfer mechanism that violates the MW theorem. In order to describe quantitatively the internal structure of starling flocks, we make use of two different quantities, such as the *pair correlation function* $g(r)$ and the *neighbours exchange rate* μ.

Pair correlation function

A function that physicists typically use to quantify the degree of spatial order of particles systems is the so called *pair correlation function* — or *radial distribution function* — $g(r)$, defined as the density of particles at a distance r from a given focal particle:

$$g(r) = \frac{1}{4\pi r^2 dr} \frac{1}{n_c(r)} \sum_{i}^{n_c(r)} \sum_{j \neq i} \delta(r - r_{ij}), \tag{1.65}$$

where r_{ij} is the distance between the i-th and the j-th particles, $\delta(r - r_{ij})$ is a smoothed Dirac δ-function and $n_c(r)$ is the number of all possible SPPs that can be picked as centroid for the computation of the pair correlation function

for a given distance r. The pair correlation function in Eq.(1.65) is a rather powerful tool to characterize different states of matter. For crystalline solid, $g(r)$ presents sharp and pronounced peaks at a constant distance, reflecting the periodic fixed disposition of particles. Liquids and gases, on the other hand, display a more structureless form for the pair correlation function, even though a residue of order is present for the liquid state: particles in a liquid display some broader peaks representing the arrangement in shells due to the intermolecular forces, while for gaseous state of matter, where such forces are absent, no order is present at all, and the pair correlation function looks almost flat [79]. We further provide a sketch of a typical pair correlation function for both a gas and a liquid in Fig. 1.7 to better compare the experimental results for starling flocks with typical liquids and gasses pair correlation functions.

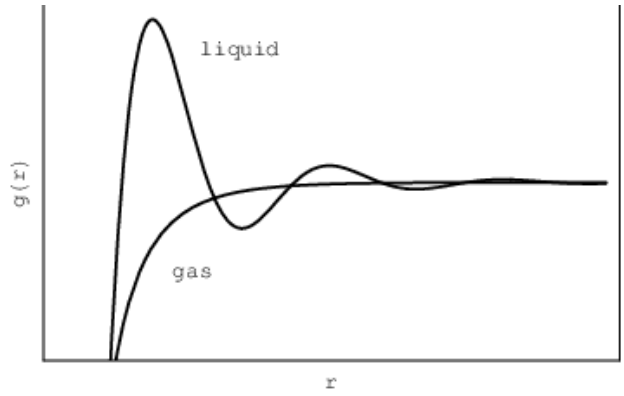

Figure 1.7: **Pair correlation function sketch** Typical pair correlation function $g(r)$ for both a liquid and a gas.

In Fig.1.8 we display the results for the radial distribution function obtained for experimental observation of starling flocks in the field [20]. The plot shows the $g(r)$ for various flocks at different densities. It is clear that the behaviour of the $g(r)$ is incompatible with the hypothesis of a crystalline structure — put forward for fish schools [80]— since, apart from the first and only peak, it has no clear structure for larger distance. This implies that positions of starlings in the flock are not fixed, but changes continuously, displaying a structure that is intermediate between a fluid and a gas. Contrary to gases, flocks have strong correlation and are able to mantain a finite shape in open space. However, they do not display the behaviour of a liquid either, lacking its typical periodic arrangement in shells.

The decay to zero of $g(r)$ at a short fixed distance is a short-range metric feature due to the birds finite wingspan, that fixes a metric exclusion zone since birds, unlike other gregarious species as fishes, try to avoid collisions at any cost.

Rate of neighbours exchange

In starling flocks, birds continuously exchange positions with their neighbours similarly to what happens in ordinary liquids. This mechanism is responsible

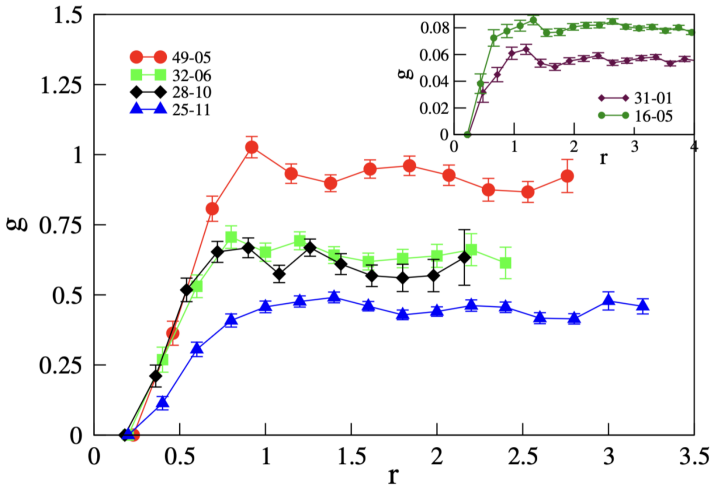

Figure 1.8: **Experimental pair correlation function** Pair correlation function $g(r)$ from experimental observation in the field of several flocks with different densities. Figure reported from [20].

for the violation of the MW theorem, allowing true long range order even in two spatial dimensions. Such neighbours exchange can be quantified by the mixing rate [71]

$$\mu = \frac{1}{N}\sum_{i}^{N}\frac{1}{m_i}\sum_{j}^{N}\left|\mathcal{N}_{ij}(t+1) - \mathcal{N}_{ij}(t)\right|, \tag{1.66}$$

where $\mathcal{N}$ is the adjacency, or connectivity, matrix, such that $\mathcal{N}_{ij}(t) = 1$ if particles i and j are topological neighbours at time t and 0 otherwise and $m_i = \sum_j \mathcal{N}_{ij}(t)$ is the number of topological neighbours of particle i at time t. The source of entropy production of the VM lies indeed in the activity of particles causing the dynamical exchange of neighbours and it can be further shown that the entropy production rate of the VM is proportional to the mixing rate μ [81]. Therefore, the irreversible, nonequilibrium dynamics of the VM is a consequence of a finite mixing rate.

However, as observed in starling flocks [82], the rearrangement of neighbours occurs on a rather slow timescale with respect to the fast relaxation of the local order parameter, meaning that even if the system is out of equilibrium on large timescales, it locally obeys an quasi-equilibrium condition. This suggests that some properties of flocks can be captured considering quasi static interaction networks.

Taken together, the features presented in this section give a comprehensive description of flocking in biological systems. In the following chapters we'll make use of these findings to characterize the internal structure and the scaling relations of flocking systems moving in unbounded spaces.

Chapter 2

Theory of cohesive flocking

As we have seen, in the VM, pure alignment interaction is not able to maintain the cohesion of a finite flock alone: in the absence of confinement, a finite group in boundless space disperses under the effect of noise fluctuations, unless additional attractive interactions are introduced [16]. In other words, the VM is not able to correctly reproduce the flocking phenomenon in the zero density limit. For instance, SPPs in metric flocks will basically become persistent random walkers as soon as the interparticle distance becomes larger than the metric interaction range. On the other hand, this won't happen in topological flocks, since particles do interact with neighbours irrespectively of their mutual distance [73]. This mechanism alone, however, is not sufficient to ensure cohesion of finite flocks, since fluctuations transversal to the mean direction of motion tend to separate nearby particles, leading to a diverging — even if only in a diffusive way — global size of the group target.

Additional attractive interactions are thus needed to guarantee cohesion. Typically, this is ensured via some kind of *social force*, introduced in the model through an overdamped torque which tends to orient the direction of motion towards nearest neighbours. In this spirit, the first attempts dates back to the so called *zonal model* [11, 19] where particles interact in different ways depending on their mutual distance, defining three different *zones*, a hard-core repulsive, an aligning and a cohesive ones. In the physics literature, social attraction was similarly introduced via a pairwise short-range repulsive-attractive force, characterised by an equilibrium metric distance [17].

While different behavioral models leading to cohesive flocking have been proposed in the literature [83–85], we argue that their dynamics ultimately generates some effective torques that implement a kind of cohesive interaction. Therefore, we decided to tackle the problem of flocking in unbounded domains in a similar way as in [17, 18], that is through the adoption of a social force that acts as an attractive torque on particles' orientation, with an intensity that grows with interparticle distance. Moreover, in order to match the observed structural features of starling flocks, with an almost structureless pair correlation function (see Sec. 1.5.4), we focus on the weak cohesion limit, where alignment interactions dominate cohesive ones. In the following, we derive a general theory for the global shape and size modes of weakly cohesive flocks and test it numerically, probing both static and dynamical properties of the global modes. Interestingly, for the simple case of attractive interactions that grow linearly with the distance, our minimal model is able to produce cohesive flocks with a global underdamped oscillatory dynamics, despite the purely overdamped behaviour of the VM. Note that the mechanism producing

this underdamped dynamics is completely different from the inertial effects introduced in Sec. 1.5.3 to better describe the flock turning dynamics via the so-called Inertial Spin Model.

The structure of this chapter is the following: in the first section the problem of flocking in open space in presented. After a brief introduction about the shortcomings of the VM in unconfined domains, the relevant literature is briefly reviewed. We then discuss the case of (weak) cohesive interaction linearly growing with the distance, presenting a comprehensive theory for the global shape and size modes of large but finite flocks in the weak cohesion limit. Our results are verified by direct numerical simulations in $d = 2$, which we argue to be the most relevant dimension for natural flock due to the presence of gravity that strongly suppresses vertical motion. One notable result consists in the relation linking the size of the flock with its typical oscillation time, which only depends on experimentally observable quantities and thus provide an obvious candidate for experimental tests of our theory. Note also that global underdamped oscillations emerge naturally, for any sufficiently large flock. We also compare the structural features of our simulated flocks, such as the velocity correlations and the pair correlation function, with the ones obtained by empirical observation of starling flocks. Finally, we briefly consider the case of nonlinear attractive forces, mainly limiting our discussion to the static characterization of the global modes.

2.1 Cohesion of flocking in open space

Several studies [10, 69, 72, 86] have highlighted the relevance of a metric-free determination of neighbours for flocking in active matter. Starling flocks observed in the wild appear to interact with a rather fixed ($\sim 7/8$) number of neighbours, located at a well-defined angular distance, but irrespectively of their actual metric distance [69]. Moreover, other hints about the relevance of metric-free interaction can be found in some works on fish schools [72] or on crowd dynamics [87], where the authors claim that pedestrians make decision based on the angular distribution of close neighbours that may screen out other possible neighbouring agents. Even if the topological VM gives rise to true long-range polar order, as for the metric counterpart, the nature of the ordered phase is qualitatively different in the topological case.

In the metric VM local density couples with local order, in the sense that the higher the density of SPPs, the more effective is the ordering mechanism [73]. In the topological case, on the other hand, there is no coupling between local density and local order since, even in sparse regions, particles are never disconnected, so low density doesn't induce disorder. This results in the absence of the so called *microphase separation*, typical of the metric version of VM, where ordered dense bands travel in a sea of disordered and sparse particles (see for instance Fig.1.2), and the transition from disorder to order appears to be continuous [88]. However more recent works suggest that a residual coupling between local order and local density should appear by means of coarse-graining dynamical renormalization group analysis so that such a different behavior should not survive the proper thermodynamic limit [89].

Moreover, the topological nature of the interaction between particles accounts for another difference between the two models. In the zero density limit, i.e. when periodic boundaries are removed, metric interaction will inevitably lead to the breaking of the flock. This is due to the fact that fluctuations transversal to the direction of motion lead to spatial separation between particles and, when the separation becomes larger than the interaction range, the SPPs basically becomes persistent random walkers. On the other hand, when the interaction is topological, particles are never isolated so they continuously interact irrespectively of their mutual distance. Topological interaction alone, however, is not sufficient to maintain cohesion of flocks in unbounded domains and the size of the flock, even if interacting particles are never isolated, is bound to diverge — even if only diffusively [73] — as one can see in Figure 2.1.

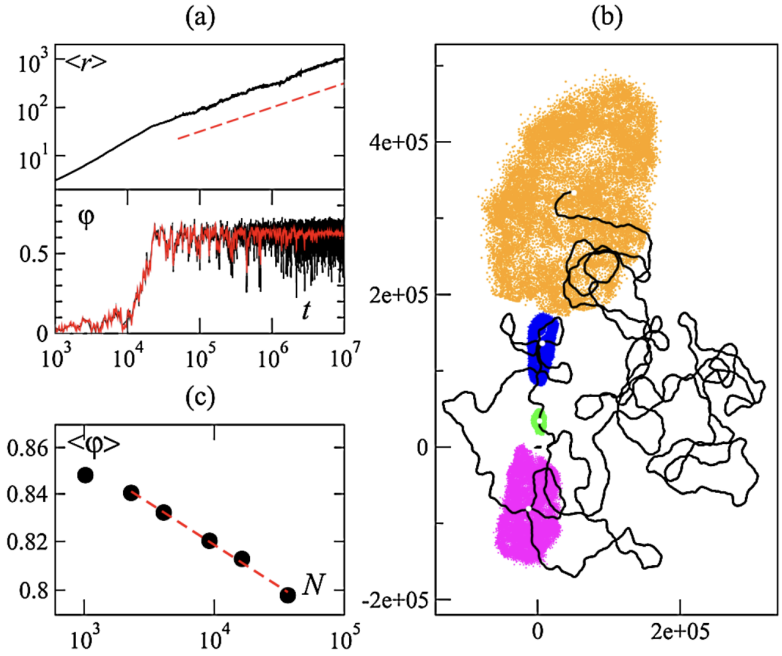

Figure 2.1: **Ordered flock in an infinite domain (a)** Mean neighbours distance $\langle r \rangle$ (top panel) and mean order parameter ϕ (bottom panel) vs time ($N = 2^{14}$, $\eta = 0.61$). The dashed line represent the diffusive behaviour $\langle r \rangle \sim \sqrt{t}$, while the red bold line in the bottom panel represents a moving average. **(b)** Trajectory of the centre of mass of the flocking (bold black line) in the diffusive regime, with some snapshots (in temporal order: green, blue, magenta and finally orange) of the configurations. **(c)** Order parameter $\langle \phi \rangle$, defined in Eq.(1.6) vs N in the diffusive regime ($\eta = 0.5$, time averages of 10^7 time steps after a transient of 10^6 time steps. Dashed line: power law with exponent -0.74. Figure reproduced from [73].

2.1.1 Zonal model

The first attempt to maintain cohesion in open space flocking can be traced back to the so called zonal model [11, 19], introduced long before the Vicsek one. In this model pairs of particles interact in different ways depending on their mutual distance, with three metric radii, namely r_{hc}, r_a and r_c, defining three different zones as depicted in Fig. 2.2 for better visualisation. Particle i will experience a hard-core repulsive force with all neighbours lying in the inner circle centred around i mimicking finite-volume exclusion. The intermediate shell, defined by the two radii r_{hc} and r_a is defined as the alignment zone, and particle i will align its direction of motion to the average direction of motion of all the neighbours lying in this shell. Finally, the third shell is characterized by an attractive pairwise torque: it will try to adjust the direction of motion towards the neighbours' centre of mass.

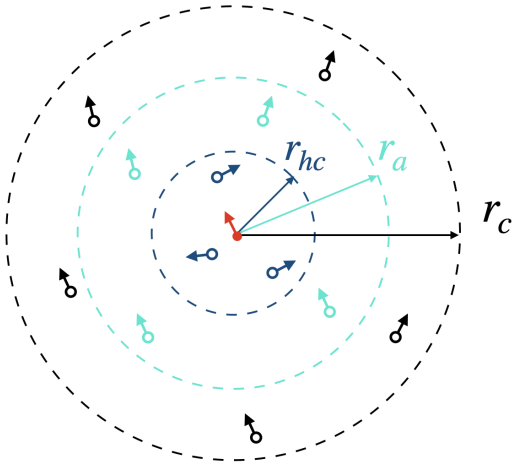

Figure 2.2: **Schematic representation of Reynolds zonal model** The i-th particle – in red – experiences different kind interactions with neighbours depending on their mutual distances: a hard core repulsive interactions with particles inside the circle with radius r_{hc}, aligning towards the mean velocity of ones inside the annulus with radii r_{hc}, r_a and attraction to the centre of mass of particles in the annulus with radii r_a, r_c.

2.1.2 Hybrid projection model

A different model giving rise to finite and deeply polarized flocks combines topological interaction between Voronoi neighbours with projected view of individuals through the entire flock [83]. In this model, large enough flocks self-organize to the maximum value of density that allows individuals from within the flock to still perceive outside signals in different directions, a condition described as *marginal opacity*. Here, individuals are modeled as identical spheres of unit size and the basic visual input they perceive is nothing but a simple dynamic pattern of dark and light across their visual cone. The presence of neighbouring agents is depicted by dark areas across light regions of clear sky. In two dimensions, light-dark domain boundaries perceived by an

agent i define a set of angles θ_{ij} (measured from the x-axis) where the j index runs over all the $\mathcal{N}_i$ light-dark boundaries sensed by the i-th individual, see for instance, the cartoon in figure 2.3 for a simple visualization. Such choice for the set of the θ_{ij} angles is motivated by behavioural models describing the neural hardware of the visual cortex in higher animals [90]. The model dynamics takes in input the light-dark domain angles — which encode the visual information about the perceived opacity of the flock — and returns characteristic directions, combining this information with other two ingredients, the tendency of individuals to coalign with neighbours and a microscopic noise. The two preferred directions are the average direction of motion of topological neighbours and the one defined by the average direction to all boundaries $\boldsymbol{\delta}_i$:

$$\boldsymbol{\delta}_i = \frac{1}{\mathcal{N}_i} \sum_{j=1}^{\mathcal{N}_i} \begin{pmatrix} \cos\theta_{ij} \\ \sin\theta_{ij} \end{pmatrix}. \tag{2.1}$$

The dynamics is then given by an analogous of equation (1.4) where now, the velocity $\boldsymbol{s}_i^{t+1}$ is picked according to

$$\boldsymbol{s}_i^{t+1} = \phi_p \boldsymbol{\delta}_i + \phi_a \langle \boldsymbol{s}^t \rangle_\sigma + \phi_n \boldsymbol{\eta}_i^t, \tag{2.2}$$

where ϕ_p, ϕ_a, ϕ_n are the relative strength of the projected visual, alignment and noise respectively, with $\phi_p + \phi_a + \phi_n = 1$. The average $\langle \cdot \rangle$ is taken over the first σ closest neighbours and $\boldsymbol{\eta}_i^t$ is a unit magnitude delta-correlated noise.

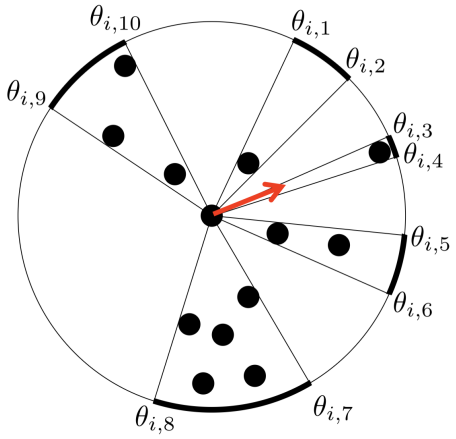

Figure 2.3: **Cartoon depiction of the visual cues perceived by an individual in the hybrid projection model** The i-th individual (in the centre) perceives dark domains (the regions where the line of sight to infinity is obscured by other individuals), represented by the thick dark lines on the circle, and light ones. The angles θ_{ij} defines the boundaries between dark and light regions and the average direction $\boldsymbol{\delta}_i$ is represented here with the bold red arrow. Figure reproduced from [83].

The two quantities used to describe the flocking state are the opacity Θ' and the average opacity seen by an individual located inside the flock Θ. The former is defined as the fraction of the sky obscured by the presence of the individuals, from the viewpoint of a distant external observer, while the latter is the same quantity but from the viewpoint of individual that lies inside the

flock.
The hybrid projection model described above displays robustly cohesive swarms, characterized by the emergency of a *marginal opacity* for both Θ and Θ', that is neither close to 0 nor to 1, with typical values in the range $0.25 \sim 0.6$, independently of the flock's size. Metric models, on the other hand, display an opacity that approaches 1 as the number of the individuals in the flock is increased, with systems becoming quickly fully opaque. Moreover, as could be seen in Fig. 2.4, changing the control parameters $\{\phi_p, \phi_a\}$, the flock is always cohesive, except for $\phi_p = 0$, where individuals just align with each other ignoring the projected view. The emergent collective behaviour of the group target — flocking/swarming/milling — is controlled via the combination of the control parameters $\{\phi_p, \phi_a\}$. If one looks at the average velocity of the centre of mass of the system, normalized by the individuals' velocity, namely α in figure 2.4(E), we can see how different combinations of the parameters lead to different emergent behaviours, from flocking ($\alpha \sim 1$) to swarming which consist in cohesive but disordered groups ($\alpha \sim 0$). These behaviors are summarized in figure 2.4.

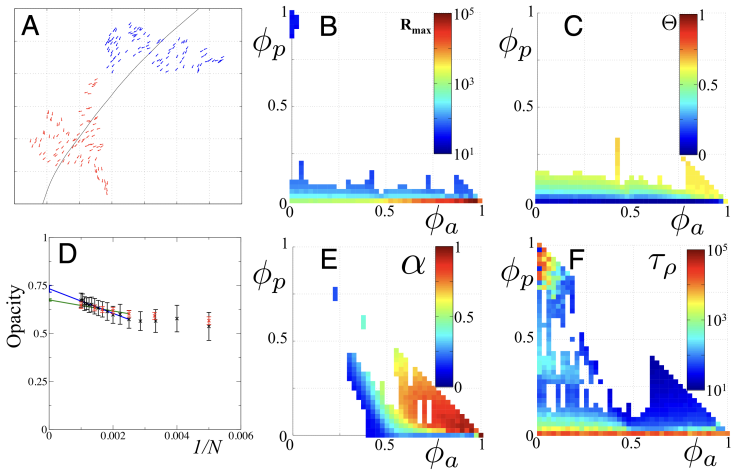

Figure 2.4: **Results from numerical simulations of the hybrid projection model** parametrized by the two parameters ϕ_p, ϕ_a with alignment computed on the first 4 neighbours. **(A)** snapshot of a 2d swarm with $\phi_a = 0.75$ and $\phi_p = 0.1$ at two different time steps (blue and red), with centre of mass moving along the solid black line. **(B)** Size of the flock, defined as the maximum distance between a pair of particles in the flock, in units of the particles diameter, for different values of the couple $\{\phi_p, \phi_a\}$. **(C)** Same plot as (B) but for the average opacity Θ. **(D)** Average opacity Θ for 2d (black) and 3d (red) swarms, as a function of $1/N$, with N being the number of individuals, with $\phi_p = 0.03$ and ϕ_a=0.8, average over $T = 5 \cdot 10^4$ timesteps. The blue line is the linear fit ($R^2 = 0.97$) for the 2d case, while the green ($R^2 = 0.99$) for the $3d$ one, for $N \geq 400$. **(E)** average speed α of the centre of mass, normalized by the individuals' speed. **(F)** swarm density autocorrelation time τ_p measuered in simulation timesteps. Figure reproduced from [83].

2.1.3 Predictive Alignment

An alternative to the zonal model [11, 19], again without explicit attractive interaction, is represented by the predictive alignment proposed in [84]. In this framework cohesion is ensured not via an explicit attractive term, but via a different alignment model that tries to predict the future positions of agents. The system is composed by N Vicsek-like agents self-propelling in discrete time in two dimension, with constant velocity v_0 in the direction of their orientation vector, parametrized by a single angle θ_i^t, $i = 1, ..., N$. At each timestep agents reorient by discrete angles $\Delta\theta_i^t \in \Omega_\theta = \pm\{0, 0.01, 0.2, 0.5\}$ rad, to achieve maximum alignment with their future neighbours. The resulting Vicsek-like dynamics is then given by

$$\mathbf{r}_i^{t+\Delta t} = \mathbf{r}_i^t + \mathbf{v}_i^{t+\Delta t}\Delta t, \tag{2.3}$$

$$\theta_i^{t+\Delta t} = \theta_i^t + \Delta\theta_i^t + \xi_i^t, \tag{2.4}$$

where ξ_i^t is a random noise term such that its amplitude $\xi_i^t \in [-\eta\pi, \eta\pi]$. In the usual VM the reorientation angles $\Delta\theta_i^t$ is chosen so to align the i-th individual's velocity to the average velocity of its neighbours. In the predictive alignment model, however, it is chosen so to maximize the generalized correlation function

$$C_i^t = \bar{\mathbf{v}}_i^t \cdot \left(\sum_{j\sim i} \mathbf{v}_j^t - (\mathbf{v}_i^t - \bar{\mathbf{v}}_i^{t+\Delta t}) \right). \tag{2.5}$$

Equation (2.5) can be interpreted as the correlation between the agent's future desired velocity $\bar{\mathbf{v}}_i^{t+\Delta t} = v_0[\cos(\theta_i^t + \Delta\theta_i^t), \sin(\theta_i^t + \Delta\theta_i^t)]$ and the generalized, non-normalized average velocity of its predicted future neighbours. The sum in (2.5) it is indeed taken over all particles in a circle with interaction radius R_0 centered around the future position of the i-th agent $\mathbf{r}_i^{t+\Delta t}$.
C_i^t is not normalized and quantifies the degree of alignment between the i-th agent's intended future heading and the dominant orientation of its predicted future neighbours.

This model, which lacks an explicit attractive torque in the alignment dynamics, is indeed able to produce deeply polarized and cohesive flocks. However, the caveat lies in the non-normalization of the correlation function evaluated in (2.5). This choice for the correlation functions will inevitably lead to favour directions where the number of predicted future neighbours will be maximized, introducing, de facto, a sort of implicit attractive torque. In the following, we will exclusively focus on the explicit implementation of pairwise social attractive torques in the context of the VM.

2.1.4 Lennard-Jones like social force

We finally discuss the classic Ref [17] which first introduced cohesion in the VM [17]. In the spirit of *social forces* arising from the gregarious behavior of

vertebrates rather than from interactions of direct physical origin, attraction is introduced through (overdamped) torques acting on pairs of particles in the Vicsek alignment dynamics (Eq. (1.5)). Equation (1.5) is then replaced by

$$\theta_i^{t+1} = \arg\left(\alpha \sum_{j\sim i} \mathbf{s}_j^t + \beta \sum_{j\sim i} \boldsymbol{f}_{ij}\right) + \eta\, \xi_i^t, \tag{2.6}$$

with the parameters α, β controlling the relative importance of the alignment and cohesion respectively. In the original formulation, the choice for the pairwise force is a short-range repulsive–attractive social force with an equilibrium distance r_e, of the kind

$$\boldsymbol{f}_{ij} = \hat{e}_{ij} \begin{cases} -\infty & \text{if } r_{ij} < r_c, \\ \frac{1}{4}\frac{r_{ij}-r_e}{r_a-r_e} & \text{if } r_c < r_{ij} < r_a, \\ 1 & \text{if } r_a < r_{ij} < r_0, \end{cases} \tag{2.7}$$

with the choice of the parameters $r_c = 0.2, r_a = 0.8, r_0 = 1$ defining shells with different interparticles interactions (namely a first hard-core repulsive one, an intermediate with cohesive interaction growing linear with distance, and one with constant force), $r_e = 0.5$ being an equilibrium metric distance and $\hat{e}_{ij}$ the unit vector along the segment going from i to j. Again the set of interacting neighbours is evaluated via a Voronoi tessellation. However, given the presence of the metric cutoff r_0, only the Voronoi neighbours within a distance r_0 contribute in (2.6). Simulations were conducted on 2d systems with periodic boundaries.

Phase Diagram

For a fixed noise amplitude ($\eta = 1$) the phase of the system is described in terms of the aligning and cohesion strength parameters α, β. For small β, i.e. weak body force, cohesion cannot be maintained. Particles in a finite box present a gas-like behaviour, while arbitrary large flocks in infinite space dissolve and particles behave essentially as isolated random walkers. Increasing the value of β, while simultaneously keeping fixed α, one expects cohesion to be restored, however, no positional order arises for intermediate β and systems display a liquid phase. For large enough β, eventually, the body force is sufficiently large so to ensure quasi-positional order and particles rearrange themselves in a sort of hexagonal lattice.
Varying α instead, one can control the global motion of the system. For instance, in a regime where cohesion is maintained, a sufficiently large α enables a collective motion of the system, that behaves either as a *moving droplet* or a *flying crystal*, depending on the value of the parameter β.

In order to quantitatively discriminate between the phases described above, two different order parameters are introduced, namely n/N and Δ. The first one is essentially the mass n of the largest cluster over the total number of particles and allows us to discriminate between the gas-like phase and the liquid one. For instance, gas-like systems (small β) will display a vanishing

n/N while increasing β we expect $n/N \sim 1$ for the liquid phase. The *liquid-solid* transition is quantified by the parameter Δ, that encodes the relative diffusion over some large time T of initially neighboring particles:

$$\Delta \equiv \left\langle \frac{1}{m_i} \sum_{j \sim i} \left(1 - \frac{r_{ij}^2(t)}{r_{ij}^2(t+T)} \right) \right\rangle_{i,t} , \tag{2.8}$$

being m_i the number of neighbouring particles of i. The parameter Δ reflects the tendency of particles in a fluid to diffuse over time, so that particles initially very close to each other will find themselves arbitrarily far apart after a sufficiently long time T. For large enough systems in the liquid phase one gets $\Delta \sim 1$, while in the solid phase one typically gets $\Delta \sim 0$, since particles in solids do not flow. For both n/N and Δ the authors set the threshold for the transition at $n/N = \Delta = 1/2$. Typical phase diagrams are represented in figure 2.1.

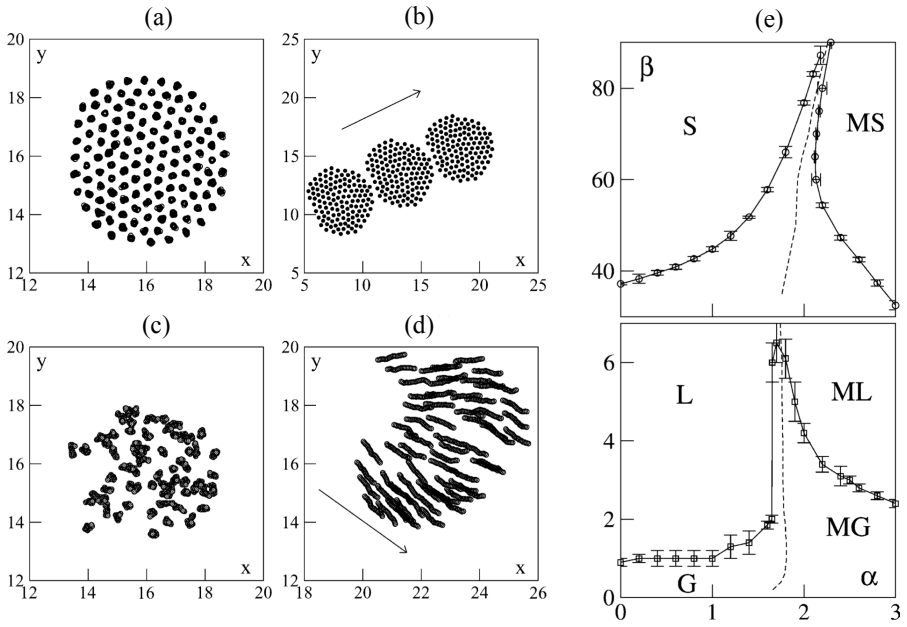

Figure 2.5: **Phases displayed by Gregoire-Chate** Cohesive flocks of 128 particles in a square box of linear size 32 with periodic boundary conditions. **(a)** Superposition of 20 different timestamps for the *immobile solid* obtained for $\alpha = 1,\ \beta = 100$. **(b)** Three snapshot taken at 120 timesteps interval of the *flying crystal*, with $\alpha = 3,\ \beta = 100$. **(c)** *Fluid droplet*, $\alpha = 1,\ \beta = 2$, for 20 consecutive timesteps. **(d)** *Moving droplet* $\alpha = 3,\ \beta = 3$, 20 timesteps. **(e)** Phase diagram for $\rho = 1/16,\ L = 180$. S: solid phase, MS: moving solid, L: liquid, ML: moving liquid, G: gas, MG: moving gas. Dashed line: transition to collective motion. Figure reproduced from [17].

2.2 Theory of weakly cohesive flocks

While the model introduced above in Section 2.1.4 can produce cohesive and polarized groups for sufficiently strong attraction, the existence of a preferred separation r_e typically imposes a liquid-like positional structure, with short-range order and damped oscillations in the pair correlation function. By contrast, empirical observations suggest that natural flocks, such as starling flocks, are largely structureless beyond the exclusion scale set by body size [20, 25]. This structural difference may be addressed by imposing balanced topological interactions (such as Voronoi neighbours [73]) and weak attractive forces [18], so that the typical neighbour distance becomes much larger than r_e and no preferred separation is effectively hardwired in the attractive interaction.

The behavior of finite flocks in this regime has been scarcely addressed in the literature, with the exception of their resilience to external perturbations implemented as scattering obstacles [18]. In this weak-cohesion regime, a number of basic questions remain unexplored. In particular, the long-time asymptotic stability of large flocks, together with their shape dynamics and possible global oscillatory modes, has received little to no attention in the literature. Yet these properties are central to any theoretical description of cohesive flocking in open space, since they determine not only whether a flock persists, but also how it deforms and relaxes on large scales.

Here we study finite cohesive flocks in the weak-cohesion regime by means of a minimal topological Vicsek-like model with pairwise alignment and social attraction. We focus on global observables describing flock extension and shape fluctuations, neglecting short-range repulsion for simplicity. The attractive interaction is taken to grow with neighbour separation, consistently with the behavioral idea that the tendency to approach neighbours increases with their distance, and consistently with what observed for instance in fish schools [72].

While we formulate the general theory in arbitrary spatial dimension d, in this work we mainly focus on its observable consequences in $d = 2$, which we argue to be the most relevant case for natural flocks. Although fish schools and bird flocks live in three-dimensional space, gravity selects a preferred direction so that collective motion typically occurs perpendicular to it and vertical fluctuations are suppressed, leading to an anisotropic, effectively quasi-two-dimensional geometry [14, 69].

Furthermore, we mostly focus on attraction torques growing linearly with distance to neighbours. In this setting, our main results are twofold.

First, we show that sufficiently large cohesive flocks display underdamped collective modes despite the purely first-order and non-inertial nature of the microscopic Vicsek dynamics. Second, we derive an experimentally testable relation between the characteristic shape-oscillation timescale and the average flock size, involving only directly measurable quantities. We will verify these results via numerical simulations of a Vicsek-like microscopic model and, towards the end of the chapter, also briefly discuss the case of nonlinear attractive torques.

2.2.1 Continuous time Vicsek model with social attraction

For concreteness, we consider a continuous time topological Vicsek-like model with pairwise alignment and attractive social forces. Particles move in d spatial dimensions with constant speed v_0 in a boundless space and are described by their position $\mathbf{r}_i(t)$ and unit headings $\hat{\mathbf{s}}_i(t)$, $i = 1, ..., N$. As previously said, social alignment provides the usual torque orienting $\hat{\mathbf{s}}_i$ towards the heading $\hat{\mathbf{s}}_j$ of its topological neighbours, while social attraction consists in a second torque term aligning $\hat{\mathbf{s}}_i$ towards the separation vector $\mathbf{r}_{ij} = \mathbf{r}_j - \mathbf{r}_i$ with a magnitude linearly growing with the distance $\|\mathbf{r}_{ij}\|$. The equations of motion then read

$$\dot{\mathbf{r}}_i = v_0 \hat{\mathbf{s}}_i, \tag{2.9}$$

$$\dot{\hat{\mathbf{s}}}_i = \mathbf{\Theta}_i^{\perp} \left[\gamma \sum_j \mathcal{N}_{ij} \hat{\mathbf{s}}_j + \beta \sum_j \mathcal{N}_{ij} \mathbf{r}_{ij} + \boldsymbol{\xi}_i \right], \tag{2.10}$$

with γ and β being respectively the alignment and attraction strength parameters. The time-dependent connectivity matrix $\mathcal{N}_{ij} = 1$ if particles i and j are Voronoi neighbours at time t and $\mathcal{N}_{ij} = 0$ otherwise. The operator

$$\mathbf{\Theta}_i^{\perp} \equiv \mathbb{I} - \hat{\mathbf{s}}_i \hat{\mathbf{s}}_i^T \tag{2.11}$$

projects vectors perpendicular to $\hat{\mathbf{s}}_i$, $\boldsymbol{\xi}_i$ is a zero-mean white noise with correlations

$$\langle \boldsymbol{\xi}_i(t) \cdot \boldsymbol{\xi}_j(t') \rangle = 2d\Gamma \delta_{ij} \delta(t - t'). \tag{2.12}$$

We are interested in the strongly aligned regime where the polar order parameter

$$\mathbf{P} = \frac{1}{N} \sum_{i=1}^{N} \hat{\mathbf{s}}_i, \tag{2.13}$$

has nearly unit amplitude $\Phi = \|\mathbf{P}\| \approx 1$, and alignment interaction dominates attraction, i.e. in the weak cohesive regime where $\gamma \gg a\beta$, with a being the characteristic Voronoi neighbours distance. We will further discuss this condition and estimate a in Section 2.2.3.

2.2.2 Spin wave expansion and Gaussian theory for the transverse sector

In finite systems, the spontaneously selected mean direction of motion $\hat{\mathbf{p}} = \mathbf{P}/\Phi$ undergoes slow angular diffusion, $\dot{\hat{\mathbf{p}}} = \boldsymbol{\eta}^{\perp}$ where $\boldsymbol{\eta}^{\perp}$ is a zero average noise term in the $(d-1)$ dimensional transversal subspace with correlations [52]

$$\langle \boldsymbol{\eta}^{\perp}(t) \cdot \boldsymbol{\eta}^{\perp}(t') \rangle = 2(d-1) \frac{\Gamma}{N} \delta(t - t'). \tag{2.14}$$

Being deeply in the ordered phase, we can perform the spin-wave expansion, decomposing the orientation field $\hat{\mathbf{s}}$ in its longitudinal and transverse component as

$$\hat{\mathbf{s}}_i = \hat{\mathbf{p}}\sqrt{1-\boldsymbol{\pi}_i^2} + \boldsymbol{\pi}_i, \tag{2.15}$$

in the reference frame co-rotating with $\hat{\mathbf{p}}$ with the transverse component w.r.t. the average polarization ($\boldsymbol{\pi}_i \cdot \hat{\mathbf{p}} = 0$) being small, $\|\boldsymbol{\pi}_i\| \ll 1$.
We introduce the symmetric Voronoi graph Laplacian

$$\mathcal{L}_{ij} \equiv \delta_{ij}\left(\sum_h \mathcal{N}_{ih}\right) - \mathcal{N}_{ij} \tag{2.16}$$

(where the sum is intended over the Voronoi neighbours) and the two projections of $\mathbf{r}_i$ defined in the reference frame co-moving at velocity v_0 and co-rotating with the average polarisation $\hat{\mathbf{p}}$. These are the transverse and longitudinal projections, respectively defined as

$$\mathbf{x}_i = \left[\mathbb{I} - \hat{\mathbf{p}}\hat{\mathbf{p}}^T\right]\mathbf{r}_i, \tag{2.17}$$

$$y_i = \hat{\mathbf{p}}^T(\mathbf{r}_i - v_0\hat{\mathbf{p}}t). \tag{2.18}$$

We then expand Eqs. (2.9)-(2.11) at the lowest order in $\boldsymbol{\pi}_i$ using Eq.(2.15). The spin-wave dynamics then reads

$$\dot{y}_i = -\frac{v_0}{2}\boldsymbol{\pi}_i^2 + (\boldsymbol{\eta}^\perp \cdot \mathbf{x}_i), \tag{2.19}$$

$$\dot{\mathbf{x}}_i = v_0\boldsymbol{\pi}_i + \boldsymbol{\eta}^\perp \sum_j \mathcal{L}_{ij} y_i, \tag{2.20}$$

$$\dot{\boldsymbol{\pi}}_i = -\gamma \sum_j \mathcal{L}_{ij}\boldsymbol{\pi}_j - \beta \sum_j \mathcal{L}_{ij}\mathbf{x}_j + \boldsymbol{\xi}_i^\perp + \beta\mathbf{b}_i, \tag{2.21}$$

where $\boldsymbol{\xi}_i^\perp$ denotes the transverse projection of the microscopic noise,

$$\mathbf{b}_i[\boldsymbol{\pi}_i, y_i] = \boldsymbol{\pi}_i \sum_j \mathcal{L}_{ij} y_j \tag{2.22}$$

is the leading order mixing term generated by the expansion of Eq. (2.10). Note that we also ignored a subleading multiplicative noise contribution $\boldsymbol{\pi}_i(\hat{\mathbf{p}}^T\boldsymbol{\xi}_i)$. The $\mathbf{b}_i$ term couples the fast transverse spin-wave dynamics of $(\mathbf{x}, \boldsymbol{\pi})$ with the slower longitudinal one, being the latter driven by $\boldsymbol{\pi}_i^2$ terms. In finite systems, angular diffusion of the mean direction of motion provides further coupling via Coriolis type multiplicative noise terms proportional to $\boldsymbol{\eta}^\perp \sim N^{-1/2}$, see Eq. (2.14).

The graph Laplacian $\mathcal{L}$ is time–dependent due to the topological neighbour reshuffling by the dynamics. While this explicit time dependence prevents a straightforward normal–mode expansion of Eq.(2.21), here we focus on a regime in which the topological network evolves on a much faster characteristic time scale τ_μ than the one of the collective fast transverse mode $\tau_\perp$. Its

validity has been verified numerically comparing the two timescale and finding that the ratio between the two timescale is approximately $\tau_\perp/\tau_\mu \approx 10$. In this "annealed-network" approximation we can average our dynamics on an intermediate timescale T_{av} such that $\tau_\mu \ll T_{av} \ll \tau_\perp$ and replace $\mathcal{L}$ by its time-averaged version $\bar{\mathcal{L}}$. At the microscopic particle level, fluctuations of the instantaneous Laplacian should generate still a multiplicative coloured noise with state-dependent amplitude. Due to scale separation, $\tau_\mu \ll \tau_\perp$, its projections on the slow eigenmodes of $\bar{\mathcal{L}}$ is, however, well described by an Ornstein-Uhlenbeck process with correlation time τ_μ. A more rigorous derivation is carried out in the Appendix A.1.1. Since this short correlation time does not significantly affect the low modes dynamics, it can be safely ignored at the Gaussian level.

The spectrum of $\bar{\mathcal{L}}$ is given by

$$\sum_j \bar{\mathcal{L}}_{ij} w_j^{(k)} = \lambda_k w_i^{(k)}, \quad k = 0, ..., N-1. \tag{2.23}$$

It is well known that the infrared spectral behaviour of locally connected graph Laplacians is universal and insensitive to local structural disorder [91]. We can thus approximate the low-lying spectrum of a finite flock of linear size L by that of a continuum Laplacian with free boundary conditions in d dimensions and a microscopic scale set by the characteristic neighbor distance a,

$$\lambda_k \approx \rho_k (a/L)^2, \tag{2.24}$$

where the dimensionless eigenvalue ρ_k obeys Weyl's scaling,

$$\rho_k \sim k^{2/d} \tag{2.25}$$

for large mode index k [92]. See Refs. [93, 94] for a more rigorous derivation via spectral inequalities.

One should however be aware that neighbour reshuffling plays an essential role in the breakdown of linearized hydrodynamics in Toner & Tu theory[5, 13], and it is in fact the microscopic source of entropy production in Vicsek dynamics [81], so that the scaling (2.24) should therefore be understood as a linearized approximation.

We first focus on the fast transverse sector $(\mathbf{x}_i, \boldsymbol{\pi}_i)$, disregarding Coriolis type terms in Eqs. (2.20)-(2.21), that are coupling terms that naturally originate from the spin-wave expansion given we put ourselves in a reference frame corotating with the direction of the average polarization. Expanding on the orthonormal eigenmodes of $\bar{\mathcal{L}}$, such that $\mathbf{x}_i = \sum_k \mathbf{X}_k w_i^{(k)}$ and $\boldsymbol{\pi}_i = \sum_k \boldsymbol{\Pi}_k w_i^{(k)}$ we get the large scale deformations of position and spin wave fields for k small but finite

$$\dot{\mathbf{X}}_k = v_0 \boldsymbol{\Pi}_k, \tag{2.26}$$

$$\dot{\boldsymbol{\Pi}}_k = -\gamma \lambda_k \boldsymbol{\Pi}_k - \beta \lambda_k \mathbf{X}_k + \boldsymbol{\Xi}_k^\perp + \beta \mathbf{B}_k, \tag{2.27}$$

where

$$\mathbf{\Xi}_k^{\perp} = \sum_i \boldsymbol{\xi}_i^{\perp} w_i^{(k)}. \tag{2.28}$$

We also denoted the projection of $\mathbf{b}_i$ on mode k as

$$\mathbf{B}_k = \sum_h Q_{kh} \mathbf{\Pi}_h, \tag{2.29}$$

where

$$Q_{kh}[Y] = \sum_p \lambda_p Y_p W_{kph} \tag{2.30}$$

is the mode coupling matrix

$$W_{kph} = \sum_i w_i^{(k)} w_i^{(p)} w_i^{(h)} \tag{2.31}$$

the triple overlap and Y_p the projection of the longitudinal coordinate on mode p. It amounts to a higher order (in the weak-cohesion expansion parameter $\epsilon = a\beta/\gamma \ll 1$) correction to the $\mathbf{\Pi}$ dissipative sector providing the feedback coupling of the slow longitudinal sector to the fast transverse spin–wave dynamics. Neglecting it, we are left with an exactly solvable Gaussian transverse theory. We use Eq. (2.26) to eliminate the spin-wave terms $\mathbf{\Pi}_k$ from Eq. (2.27) to obtain

$$\ddot{\mathbf{X}}_k = -\gamma_k \dot{\mathbf{X}}_k - \beta_k \mathbf{X}_k + v_0 \mathbf{\Xi}_k^{\perp}. \tag{2.32}$$

In this Gaussian and annealed approximation, the lowest transverse modes, with the exclusion of the zero eigenvalue associated to rigid translation, follow the dynamics of a stochastically forced linear oscillator with an effective dissipation $\gamma_k = \gamma\lambda_k$ and an effective harmonic stifness $\beta_k = v_0\beta\lambda_k$. In particular, we can readily compute the expectation values of the low-lying modes:

$$\langle \mathbf{X}_k \rangle = 0, \tag{2.33}$$

$$\langle \mathbf{X}_k^2 \rangle = (d-1)\frac{v_0\Gamma}{\gamma_k\beta_k} = (d-1)\frac{v_0\Gamma}{\gamma\beta}\left(\frac{L}{a}\right)^4 \frac{1}{\rho_k^2}\,, \tag{2.34}$$

and their autocorrelations

$$\begin{aligned} C_{kh}(t) &= \langle \mathbf{X}_k(t) \cdot \mathbf{X}_h(0) \rangle \\ &= \delta_{kh} \langle \mathbf{X}_k^2 \rangle e^{-\frac{\gamma_k}{2}|t|} \left[\cos(\Omega_k t) + \sin(\Omega_k t)\right], \end{aligned} \tag{2.35}$$

with natural frequencies

$$\Omega_k = \sqrt{\beta_k - \frac{\gamma_k^2}{4}} = \frac{a\sqrt{\rho_k}}{L}\sqrt{v_0\beta - \frac{\gamma^2}{4}\frac{a^2\rho_k}{L^2}}\,. \tag{2.36}$$

For large enough

$$L/a > [(\gamma^2\rho_k)/(4v_0\beta)]^{1/2} \tag{2.37}$$

natural frequencies are real for any given finite β. Even in the alignment dominated regime, the lowest modes of finite flocks are characterized by an underdamped, oscillatory dynamics despite the dissipative nature of Vicsek dynamics. Oscillations disappear only in the absence of social attraction, i.e. $\beta = 0$, or in the equilibrium limit where $v_0 = 0$. This is one of the central findings of this work.

2.2.3 Global modes

We now discuss the consequence of these results on global size indicators such as the squared gyration radius

$$\begin{aligned} R_g^2 &= \frac{1}{N}\sum_i (\mathbf{r}_i - \mathbf{r}_{cm})^2 \\ &= \frac{1}{N}\sum_{k>0}\left(\mathbf{X}_k^2 + Y_k^2\right) \equiv R_\perp^2 + R_\parallel^2, \end{aligned} \tag{2.38}$$

where $\mathbf{r}_{cm}$ is the instantaneous centre of mass position of the flock and we have separated the transverse and longitudinal contributions. They are estimators of the transverse and longitudinal flock extent, $L_\perp = \sqrt{\langle R_\perp^2\rangle}$ and $L_\parallel = \sqrt{\langle R_\parallel^2\rangle}$. We first focus on the transverse sector. Due to Weyl scaling, the corresponding modes' sum is convergent in physical dimensions $d = 2, 3$ and the transverse gyration radius is dominated by the lowest modes. From Eq. (2.34) we get

$$\langle R_\perp^2\rangle = \frac{1}{N}\sum_{k>0}\langle \mathbf{X}_k^2\rangle = S_d\,\frac{v_0\Gamma}{\gamma\beta}\left(\frac{L}{a}\right)^4\frac{1}{N}\,, \tag{2.39}$$

where

$$S_d = (d-1)\sum_{k>0}\rho_k^{-2} \tag{2.40}$$

is an order one geometric factor. In the absence of mean orientation diffusion, and assuming that the global density is independent of N, the flock shape can be characterized by the scaling with N of its transverse and longitudinal extent,

$$L_\perp \sim aN^{\alpha_\perp}, \tag{2.41}$$

$$L_\parallel \sim aN^{\alpha_\parallel}, \tag{2.42}$$

with

$$(d-1)\,\alpha_\perp + \alpha_\parallel = 1, \tag{2.43}$$

given by the flock's total constant density. Substituting into Eq. (2.39), with $L = \max(L_\perp, L_\parallel)$, yields the isotropic scaling

$$\alpha_\perp = \alpha_\parallel = 1/2 \tag{2.44}$$

for $d = 2$. In $d = 3$, on the other hand, one has either $\alpha_\perp = 1/2$ and $\alpha_\parallel = 0$ for $L = L_\perp > L_\parallel$ or $\alpha_\perp = 3/10$ and $\alpha_\parallel = 2/5$ for $L = L_\parallel > L_\perp$. In both cases, the scaling is anisotropic and the ratio $L_\parallel/L_\perp$ either vanishes or diverges in the large N limit. In Section 2.3.1 we verify numerically that anisotropic scaling indeed follows the latter option, possibly with logarithmic corrections not captured by this simple scaling argument.

Isotropic scaling is supported by a direct inspection of the longitudinal dynamics carried out in Appendix A.1. Here we summarize the main result of this analysis. In the absence of global orientation diffusion, the slow longitudinal dynamics (2.19) is coupled back to the fast transverse sector via the first-order correction $\mathbf{B}_k$. Adiabatic elimination of the fast transverse spin-wave sector yields, to first order in the weak-cohesion expansion, an effective Ornstein-Uhlenbeck dynamics for the longitudinal modes,

$$\dot{Y}_k \simeq -\sum_h M_{kh} Y_h + \Delta_k, \tag{2.45}$$

with M positive definite. Longitudinal fluctuations are therefore confined and overdamped. In the isotropic $d = 2$ regime, the mode overlap sums entering the effective drift and noise terms are dominated by modes of wavelength comparable to that of mode k, implying

$$\langle Y_k^2 \rangle \sim \lambda_k^{-2} \tag{2.46}$$

and therefore the same scaling as the transverse modes. Under additional regularity assumptions, one also obtains

$$\langle R_\parallel^2 \rangle \lesssim \langle R_\perp^2 \rangle. \tag{2.47}$$

On the other hand, in $d = 3$, where there are two equivalent transverse directions, Eq. (2.39) is inconsistent with the isotropic scaling $L \sim aN^{1/3}$ and instead suggests a strongly anisotropic regime with anomalous behavior. In the following, we focus on the biologically relevant case $d = 2$.

We can further relate Eq. (2.39) to the flock polar order parameter by making use of the spin-wave expansion [95] and remembering that in Toner-Tu theory the effective noise amplitude determines the size of equal-time spin-wave fluctuations [14],

$$1 - \Phi \simeq \sum_i \langle \boldsymbol{\pi}_i^2 \rangle / (2N) \sim \Gamma/\gamma, \tag{2.48}$$

where $\Phi = \langle ||\mathbf{P}|| \rangle$ is the time averaged order parameter. We thus obtain

$$\langle R_\perp^2 \rangle = c_d \frac{v_0(1-\Phi)}{\beta} N \,, \tag{2.49}$$

with c_d a nonuniversal $O(1)$ dimensionless constant. Since $\langle R_\perp^2 \rangle \sim a^2 N$, Eq. (2.49) also provides an estimate of the characteristic length

$$a \sim \sqrt{v_0 \beta^{-1}(1-\Phi)}. \tag{2.50}$$

The weak-cohesion condition then reads

$$a\beta \sim \sqrt{v_0 \beta (1-\Phi)} \ll \gamma. \tag{2.51}$$

Due to the underdamped behavior of the low-lying modes for sufficiently large N (or β), stationary time series of $R_\perp^2$ will also show underdamped oscillatory autocorrelations. The longitudinal squared gyration radius $R_\parallel^2$, on the other hand, will be characterized by a slower and overdamped dynamics. In the absence of mean orientation diffusion, in $d = 2$ we thus expect a statistically anisotropic finite flock, elongated in the transverse direction and characterized by underdamped transverse shape fluctuations.

We finally note that Eq. (2.39) still depends on the attraction parameter β which cannot be directly accessed in field observations. To circumvent this difficulty, we note that for large N the underdamped dynamics is dominated by the lowest collective mode, with frequency given by Eq. (2.34) (once again, with $L \sim \sqrt{N}$)

$$\Omega_1 \simeq \sqrt{\rho_1 v_0 \beta / N}. \tag{2.52}$$

This essentially allows one to estimate the transverse timescale from the position of the first minimum in the autocorrelation function. For large N one has

$$\tau_\perp \simeq \frac{\pi}{\Omega_1} = \frac{\pi N^{1/2}}{\sqrt{\rho_1 v_0 \beta}}. \tag{2.53}$$

Eq. (2.53) can be used together with Eq. (2.49) to deduce an effective β from the joint measure of the typical flock size R_g^{rms} and of the characteristic autocorrelation time $\tau_\perp$. This leads to the particularly simple relation

$$R_g^{rms} = \kappa(v_0, \Phi)\tau_\perp, \tag{2.54}$$

with

$$\kappa(v_0, \Phi) = a_2 v_0 \sqrt{1-\Phi}, \tag{2.55}$$

$$a_2 = \frac{1}{\pi}\sqrt{2\rho_1 c_2}. \tag{2.56}$$

This implies the collapse on a single line of the typical flock size plotted w.r.t. $\kappa\,\tau_\perp$ for systems with different parameters obtaining an experimentally testable relation that only depends on observable quantities such as the typical bird speed v_0 and the flock polarization Φ.

2.3 Numerical simulations

We test these results via numerical simulations in two spatial dimensions. A brief discussion of numerics for the three-dimensional case will be provided at the end of this section. For efficiency, we consider a discrete-time topological VM with social attractive force and vectorial noise [96]

$$\mathbf{r}_i^{t+1} = \mathbf{r}_i^t + v_0 \hat{\mathbf{s}}_i^{t+1}, \tag{2.57}$$

$$\hat{\mathbf{s}}_i^{t+1} = \boldsymbol{\theta}\left[\gamma \sum_j \mathcal{N}_{ij}\hat{\mathbf{s}}_j^t + \beta \sum_j \mathcal{N}_{ij}\mathbf{r}_j^t + m_i^t \eta \boldsymbol{\xi}_i^t + \mathbf{h}\right], \tag{2.58}$$

which we expect to share the same large-scale properties with the continuous time dynamics (2.9)-(2.10). Here $\boldsymbol{\theta}[\mathbf{u}] = \mathbf{u}/|\mathbf{u}|$, $m_i^t = \sum_j \mathcal{N}_{ij}$ is the number of all topological neighbours interacting with i-th particle at time t and the $\boldsymbol{\xi}_i^t$ are random, uniformly distributed and uncorrelated unit vectors. The parameter γ is the coefficient of the aligning term, β the one for the cohesion, v_0 is the particles' speed and η is the amplitude of the noise. Finally, a small external field of amplitude h is introduced, so to prevent the diffusion of the mean direction of motion. In the following, unless otherwise stated, we fix $\gamma = 1,\ \eta = 0.3$ and $v_0 = 0.5$.

2.3.1 Directed flocking

We first wish to test our theory in the absence of Coriolis-like term that may mix the longitudinal and transversal directions. In order to suppress the angular diffusion of the mean flocking direction, we initially added a small external field of amplitude $h = |\mathbf{h}|$ [60] that locks $\hat{\mathbf{p}}$ to the field direction. This choice allows us to study the behaviour of the transversal and longitudinal components of the gyration radius in a regime where they do not mix. Denoting by ψ the angle between $\mathbf{h}$ and the mean flocking direction, we have indeed

$$\langle \delta\psi^2 \rangle \sim (hN)^{-1} \tag{2.59}$$

for the *directed flocking* case [52]. The choice $h = 2 \cdot 10^{-3}$, for instance, yields numerically $\langle \delta\psi^2 \rangle \approx 1.3 \cdot 10^{-2}$ for $N = 10^4$ and $\beta \in [10^{-3}, 1]$. We expect this choice to not distort significantly our unperturbed results as long as h is small compared to the typical magnitude of alignment and attraction terms.

Typical time series for R_g^2 and its transverse and longitudinal components are reported in 2.6(a). As one can readily verify, the transverse extension is always larger than the longitudinal one and the behaviour of the former resembles the

one of the full squared gyration radius. Moreover, R_g^2 displays qualitatively the same underdamped oscillations of its transverse component $R_\perp^2$, while the longitudinal component $R_\parallel^2$ seems to display a totally different one. The different transverse and longitudinal timescales can also be appreciated from the connected autocorrelations

$$G_\alpha(t) = \langle R_\alpha^2(t) R_\alpha^2(0)\rangle - \langle R_\alpha^2\rangle^2, \quad \alpha = \perp, \parallel, g \tag{2.60}$$

shown in Fig. 2.6(b). $R_\perp^2$ and R_g^2 present the same typical underdamped oscillations, as confirmed by having almost the same exact connected autocorrelation functions in Fig. 2.6(b), while the longitudinal component $R_\parallel^2$ presents an overdamped behaviour characterized by the absence of such harmonic oscillations. Note that the negative lobes of the transverse autocorrelation suggest mode-coupling corrections to the quadratic Gaussian behavior, as discussed in the Appendix A.2.

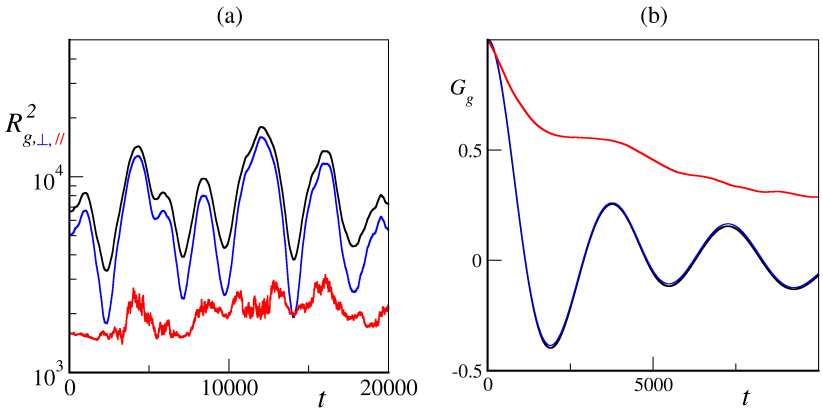

Figure 2.6: **Statics and dynamics for flocks subjected to a small external field** **(a)** Time series of the squared gyration radius R_g^2 (black) and its longitudinal (red) and transverse (blue) components, namely $R_\parallel^2$ and $R_\perp^2$, with an external field of amplitude $h = 2 \cdot 10^{-3}$ that prevents the mean flocking direction to slowly diffuse over time. **(b)** Connected autocorrelations for the root-mean-squared gyration radius and its two components, again with the same amplitude of the external field h. The colour scheme is the same as in panel (a).

We now consider the root-mean-squared gyration radius $R_g^{rms} = \sqrt{\langle R_g^2\rangle}$ which is a good estimator of the flock size. The isotropic scaling

$$L_\parallel^{rms} \lesssim L_\perp^{rms} \sim \sqrt{v_0(1-\Phi)N/\beta}, \tag{2.61}$$

involves the longitudinal and perpendicular global size of the flock. In Fig. 2.7 we tested this relation by plotting the transversal (blue) and longitudinal (red) components of the root-mean-squared gyration radius varying both the attraction strength $\beta \in [10^{-3}, 0.5]$ (Fig. 2.7(a)) and the number of particles $N \in [5 \cdot 10^2, 10^4]$ (Fig. 2.7(b)). The dashed black lines mark the predicted scaling according to Eq.(2.61). As we can readily see from Fig. 2.7, the latter relation is numerically confirmed when the small external field of amplitude

h that locks the average direction towards the field's direction and prevents longitudinal and transversal components of R_g^2 to mix.

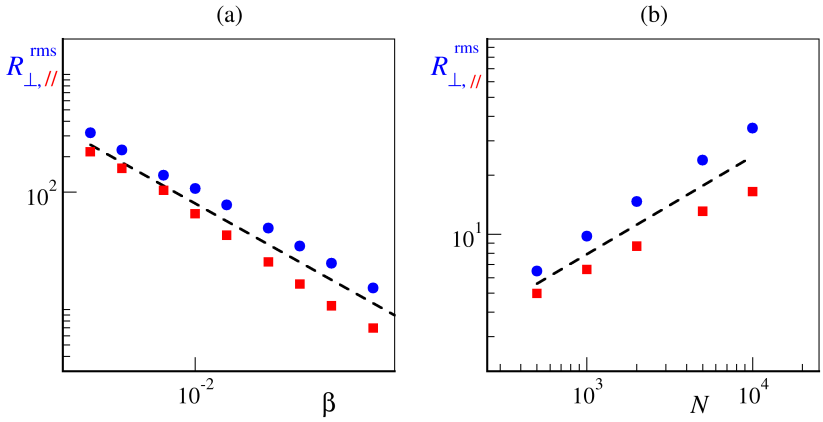

Figure 2.7: **Scaling of root-mean-squared gyration radius** **(a)** Stationary time average of the longitudinal ($R_\parallel^2$) and transverse ($R_\perp^2$) components of the root-mean-squared gyration radius vs $\beta \in [10^{-3}, 0.5]$ with an external field of amplitude $h = 2 \cdot 10^{-3}$ that prevents the mean flocking direction to slowly diffuse over time. The dashed black line marks the best fit by Eq. (2.49). **(b)** Stationary time average of the longitudinal and transverse components of the root-mean-squared gyration radius vs $N \in [5 \cdot 10^2, 10^4]$ with again the same external field amplitude h. The dashed black line marks the best fit by Eq. (2.49).

We now turn the attention to the three-dimensional case in order to verify the anysotropic scaling of the transverse and longitudinal flock's extension discussed in Sec. 2.2.3. Numerical simulations reported in Fig. 2.8(a) of Eqs. (2.9)-(2.10) in $d = 3$ support the anisotropic scaling with $\alpha_\perp = 1/2$ and $\alpha_\parallel = 0$ in Eqs. (2.41)-(2.42), once we add logarithmic corrections in the form

$$L_\perp \sim a\sqrt{N/\ln N} \tag{2.62}$$

and

$$L_\parallel \sim a \ln N, \tag{2.63}$$

so that

$$L_\perp^2 L_\parallel \sim a^3 N. \tag{2.64}$$

These logarithmic corrections cannot be captured by our Gaussian theory scaling and their investigation is left for future work.

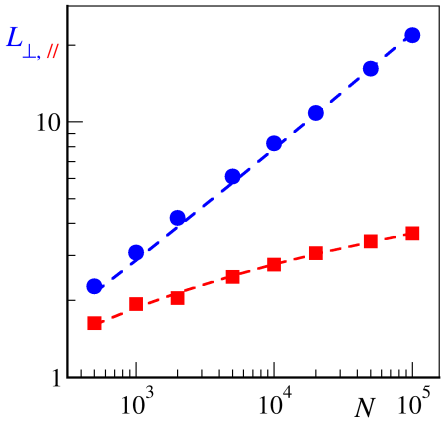

Figure 2.8: **Numerical simulations in $d = 3$** Root-mean-square transverse (blue circles) and longitudinal (red squares) gyration radii vs. N for $\beta = 0.05$ and $h = 0.002$. The dashed lines mark the transverse $L_\perp \sim \sqrt{N/\ln N}$ and longitudinal $L_\parallel \sim \ln N$ scaling with logarithmic corrections.

2.3.2 Spontaneous flocking

Typical starling flocks, however, are observed in the absence of stationary external fields [97], showing spontaneous symmetry breaking rather than a directed one. In this more realistic setup, Coriolis-type terms must be taken into account. Their net effect is to induce diffusion in the mean flocking direction that tends to mix the transverse and the longitudinal components. As a consequence, the longitudinal gyration radius more closely resembles the underdamped dynamics of the transverse one, as shown in Fig.2.9. Their connected autocorrelation functions, alongside the total one for R_g^2, also present the characteristic underdamped signatures of the transverse sector dynamics.

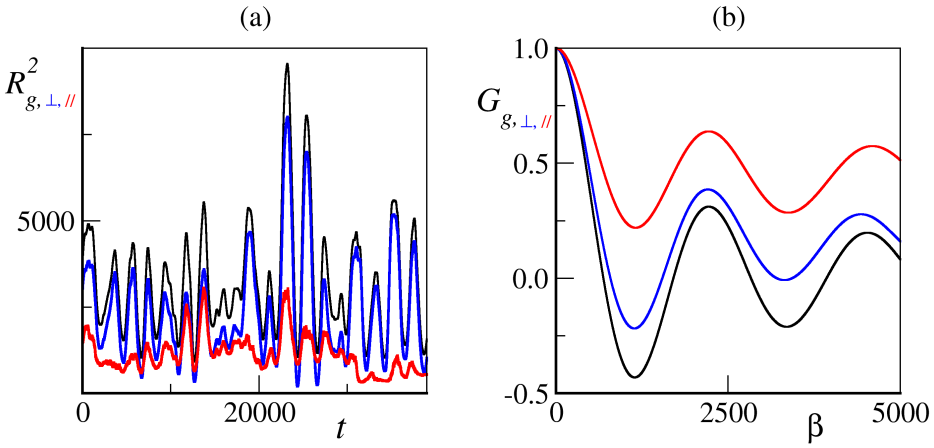

Figure 2.9: **Spontaneous symmetry breaking flocking** **(a)** Time series of the squared gyration radius R_g^2 (black) and its transverse (blue) and longitudinal (red) components for spontaneous symmetry breaking flocking for a flock of $N = 10^4$ SPPs, $\eta = 0.3$ and $\beta = 5 \cdot 10^{-2}$. **(b)** Connected autocorrelations for the quantity in panel (a) with the same colour coding.

In the following we will mainly focus on the full gyration radius, dominated by the transverse Gaussian sector dynamics.

Polarization in finite flocks

We performed numerical simulations by varying both the number N of self-propelled particles (SPPs) and the attraction coefficient β. We have verified that spontaneous cohesive flocking emerges even for rather small cohesion parameter, at least up to $\beta = 5 \cdot 10^{-5}$. This behavior is confirmed by a finite mean-squared gyration radius and by a finite order parameter Φ of order one. As shown in Fig. 2.10(a), when varying the attraction strength β while keeping the number of particles N fixed, the order parameter remains approximately constant — i.e., it is essentially independent of β — as one would reasonably expect in the weak cohesion limit. Conversely, when β is kept constant and N is varied, as shown in Fig. 2.10(b), the order parameter converges to an asymptotic order one value, signaling long range order. This finite size, power-law decay to the asymptotic value is consistent with the behavior reported in [73] and controlled by the roughness scaling exponent, as discussed in [22].

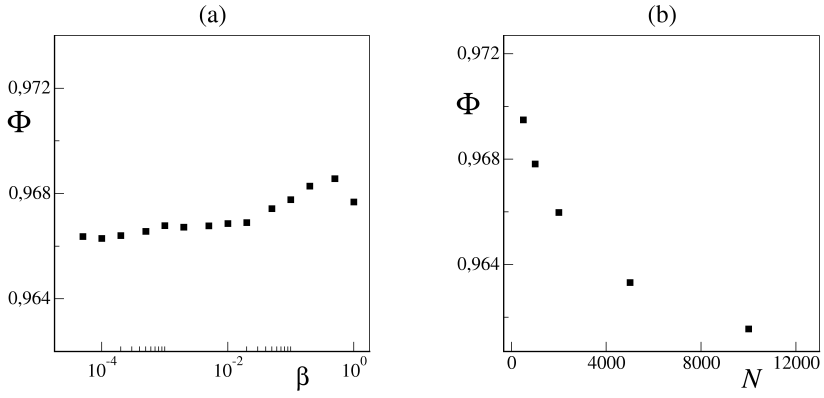

Figure 2.10: **Stationary order parameter (a)** Stationary order parameter ϕ of the metric free model as a function of the cohesion strength β for $N = 10^3$. ϕ remains approximately constant if β is varied. **(b)** Stationary average of ϕ as a function of the number of active particles N, with $\beta = 10^{-1}$.

Statics of finite flocks: global size indicators

Cohesion, on the other hand, is displayed via finite global size indicators, such as the mean-squared gyration radius R_g^2 and its root-mean-squared version R_g^{rms}. As an example, in Fig.2.11, we display some time series of the gyration radius in the stationary regime, for different $\beta \in [10^{-3}, 1]$ (panel (a)) and for different $N \in [5 \cdot 10^2, 10^4]$ (panel (b)). The value for the gyration radius is always finite and, as β is increased, it starts to oscillate as we found in Section 2.2.1 for its perpendicular component. Qualitative confirmation of Eq.(2.52) can be found in Fig.2.16. The number of SPPs in 2.11(a) is kept fixed to $N = 10^3$. In panel (b), instead, the time series of the gyration radius of the flock is displayed keeping the attraction parameter fixed to $\beta = 0.1$ while varying the number of particles N. We can immediately see that characteristic underdamped oscillatory behaviour is present for each value of $N \in [5 \cdot 10^2, 10^4]$.

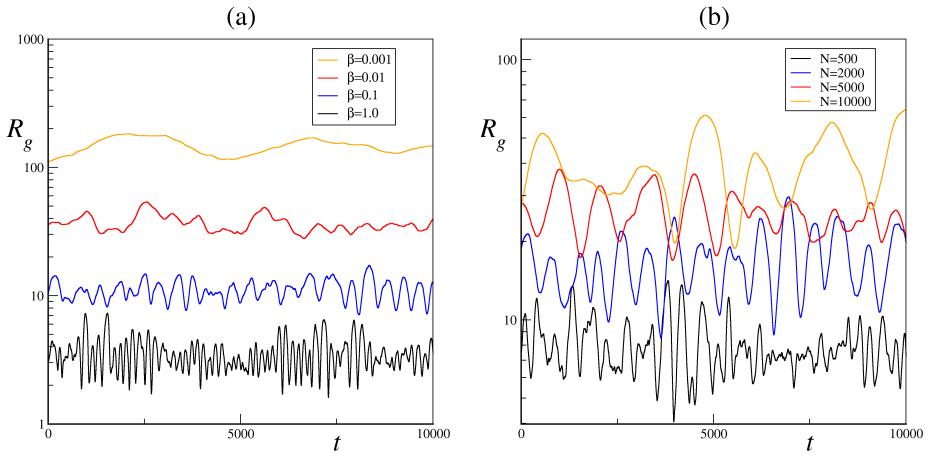

Figure 2.11: **Time series of the gyration radius R_g (a)** Time series of R_g for different values of the cohesion strength β with $N = 10^3$. **(b)** Time series of R_g for different active particles' number N, with $\beta = 10^{-1}$.

In Fig. 2.12 we display the stationary average of the transverse and longitudinal components of the root-mean-squared gyration radius $R_\perp^{rms}$ and $R_\parallel^{rms}$. In panel (a) the stationary average of $R_{\perp,\parallel}^{rms}$ are plotted as a function of the attraction strength $\beta \in [5 \cdot 10^{-5}, 1]$. As one can easily see, for small values of β, the transverse and longitudinal components not only share the same scaling but also, due to Coriolis-like term mixing, also become practically indistinguishable, at least at small enough β. In panel (b) the scaling with N of $R_{\perp,\parallel}^{rms}$ is presented. Both components seem to scale with the same power-law behaviour, with the transverse one being slightly larger than the longitudinal one. In practice we find that $R_\parallel^2(t)$ becomes comparable to $R_\perp^2(t)$, so that $R_g^2(t) \approx 2R_\perp^2(t)$.

After displaying the results for the transverse and the longitudinal extensions, we now turn the attention to the full gyration radius. In Fig. 2.13(a) we display the stationary average of R_g^{rms} as a function of the attraction strength β, while, in the panel (b) of the same Figure, we have the its scaling with N. The dashed magenta line marks the best fit by our theory, by Eq.(2.49). Eq. 2.49 fits nicely the numerical data for the typical flock size determined by $R_g^{\rm rms} \equiv \sqrt{\langle R_g^2 \rangle} \simeq \sqrt{2} L_\perp$ with a single fitting parameter $c_2 \approx 1/2$, even if we are currently unable to determine this nonuniversal prefactor from our theory. To summarize our findings, numerics show strong agreement with Gaussian theory, confirming that the full gyration radius is dominated by the low-lying modes of its transversal component.

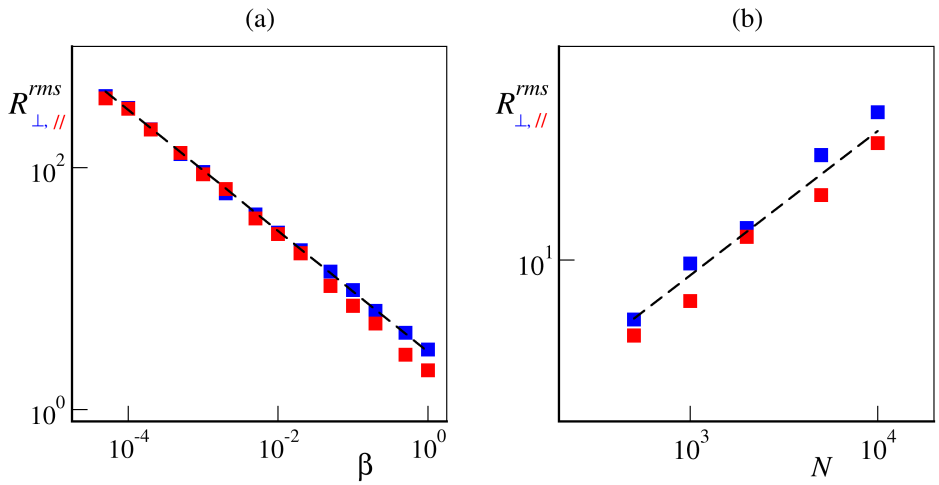

Figure 2.12: **Stationary average of transversal and longitudinal extensions (a)** Stationary average of $R_{\perp}^{rms}$ (in blue) and of $R_{\parallel}^{rms}$ as a function of $\beta \in [10^{-4}, 1]$ for $N = 10^3$. **(b)**. Stationary average of $R_{\perp}^{rms}$ (in blue) and of $R_{\parallel}^{rms}$ as a function of $N \in [5 \cdot 10^2, 10^4]$. The dashed black lines mark the theoretical scaling of Eq.(2.49). The order parameter $\Phi \approx 0.965$

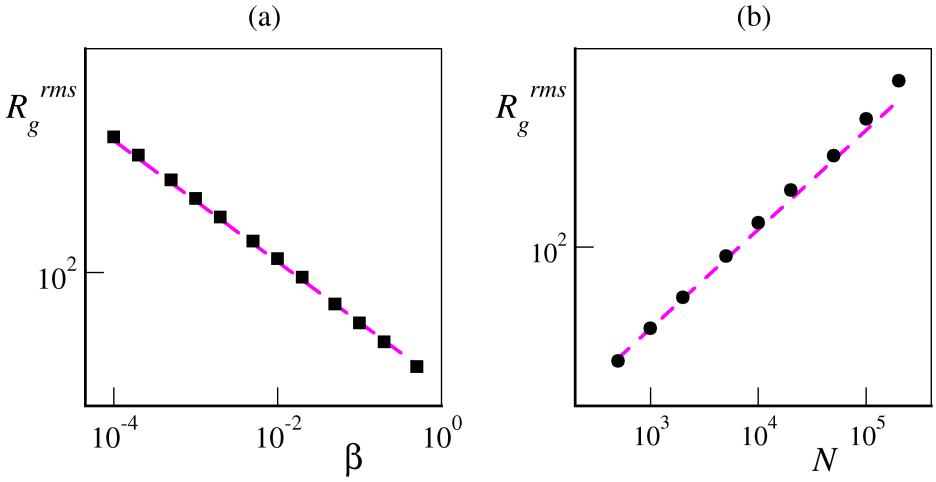

Figure 2.13: **Stationary average of root-mean-squared gyration radii (a)** Stationary average of R_g^{rms} as a function of $\beta \in [10^{-4}, 1]$ for $N = 10^3$. The magenta dashed line marks the best fit by our theory with $c_2 \approx 1/2$ (see Eq. (2.49)). **(b)** Stationary average of R_g^{rms} as a function of $N \in [5 \cdot 10^2, 2 \cdot 10^5]$. The magenta dashed line marks the best fit by our theory with $c_2 \approx 1/2$ (see Eq. (2.49)). For both panels we have $v_0 = 0.5$ and $\eta = 0.3$. The order parameter $\Phi \approx 0.965$

Dynamics of finite flocks: underdamped oscillations regime

We now focus on the dynamical properties of cohesive flocks by analyzing the connected autocorrelations G_g of R_g^2 and of its transverse and longitudi-

nal components (see Eq.(2.60)). In Fig. 2.14, we show that for $\beta = 2 \cdot 10^{-3}$ and $N = 5 \cdot 10^2$ (black line), the gyration radius does not yet exhibit a clear underdamped behavior consistently with the theoretical prediction that in the weak cohesion limit only large enough flocks should display fully underdamped oscillations. However, as the number of particles increases, R_g^2 progressively develops the characteristic oscillations of the underdamped regime, which become increasingly pronounced. This is consistent with the Gaussian theory, that predicts the emergence of characteristic oscillations for arbitrary small values of β if N is large enough. Being the dynamics dominated by the low-lying modes — see Eq.(2.36) — it is sufficient to take N large enough so that the frequency in Eq.(2.36) becomes real, so that underdamped oscillations appear.

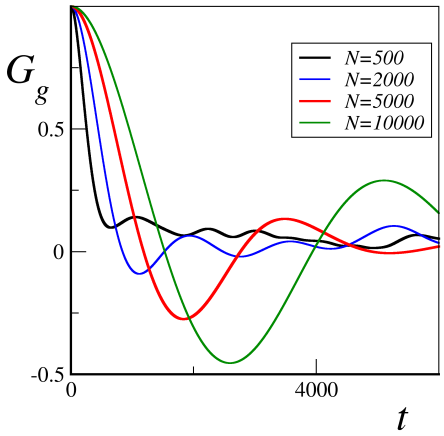

Figure 2.14: **Autocorrelation of R_g^2 for small attraction parameter** Autocorrelation G_g for the squared gyration radius R_g^2 for $\beta = 2 \cdot 10^{-3}$ for different number of active particles N. If N grows the underdamped behaviour appears and becomes more and more clear. The noise amplitude is $\eta = 0.3$.

We have seen that, for sufficiently large N (or equivalently large β), flocks exhibit the characteristic underdamped behavior of a stochastically forced harmonic oscillator, with autocorrelations given by Eq. (2.35). We now aim to characterize such dynamics in terms of the characteristic timescale $\tau_\perp$ governing these oscillations.

To this end, we performed additional numerical simulations in the regime where the system displays clear underdamped oscillations, exploring different values of the attraction parameter β and system size N. In Fig. 2.15, we report the autocorrelations of R_g^2 obtained by varying these parameters.

In Fig.2.15 we present the connected autocorrelations G_g of the mean-squared gyration radius R_g^2 for different β and N. We firstly fixed $N = 10^3$ and evaluated G_g for different values of the attraction strength $\beta \in [10^{-2}, 5 \cdot 10^{-1}]$ (Fig.2.15(a)). As one can see from panel (b) of the same figure, once rescaling the time by a factor $\beta^{1/2}$ all , as suggested from Eq. (2.53), the autocorrelation minimum we used to define $\tau_\perp$, almost collapse on the same value. Analogously, we display in Fig.2.15(c) G_g for different sizes $N \in [5 \cdot 10^2, 10^4]$ with $\beta = 10^{-1}$. Panel (d) shows how all the the characteristic timescale collapse when rescaling

the time by a factor $N^{-1/2}$. These numerical results confirm the scaling of the characteristic time of oscillations $\tau_\perp$ with both β and N in Eq.(2.53).

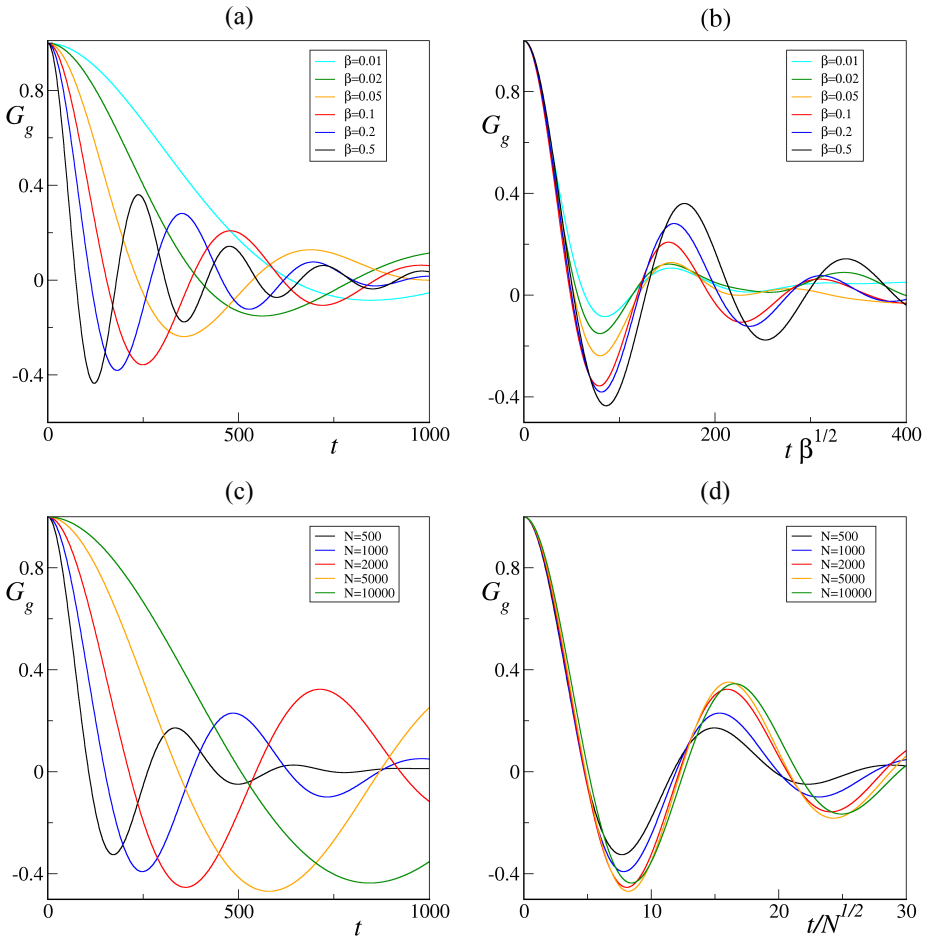

Figure 2.15: **Autocorrelation function of the squared gyration radius (a)** Autocorrelation function for the mean squared gyration radius R_g^2 for different values of the cohesion strength β. **(b)** Collapse of the autocorrelation functions of panel (a) when the time is rescaled by a factor $\beta^{1/2}$. **(c)** Autocorrelation function for the mean squared gyration radius R_g^2 for different values of the number N of active particles. **(d)** Collapse of the autocorrelation functions of panel (c) when the time is rescaled by a factor $N^{-1/2}$.

To be more precise, we directly measure the characteristic timescale $\tau_\perp$ associated with the transverse dynamics from the connected autocorrelations of R_g^2 as the position of the first minimum of the autocorrelation function of the gyration radius. We then plot the extracted times for different values of β and N. The results are shown in Fig. 2.16(a,b).

In panel (a), we report the timescale $\tau_\perp$ at fixed $N = 10^3$ as a function of $\beta \in [10^{-3}, 1]$. The black dashed line corresponds to the behavior suggested by Eq. (2.53), yielding the scaling $\tau_\perp \sim \beta^{-1/2}$. In panel (b), we show the transverse characteristic timescale at fixed $\beta = 10^{-1}$ as a function of the number of particles $N \in [5 \cdot 10^2, 10^4]$, with the dashed line marking the scaling $\tau_\perp \sim N^{1/2}$, again in agreement with Eq. (2.53). Overall, the numerical results strongly support the scaling relations predicted by the Gaussian approximation.

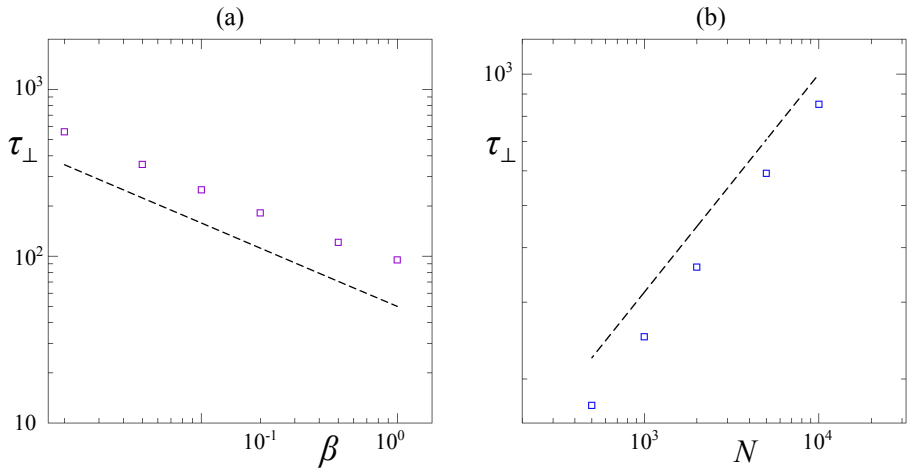

Figure 2.16: **Scaling of the transverse characteristic timescale of oscillations** t **(a)** Scaling of the position of the first minimum $\tau_\perp$ of the autocorrelation function for $N = 10^3$ w.r.t. the cohesion strength β. The dashed black line represents $\tau_\perp \sim \beta^{-1/2}$. **(b)** Scaling of the position of the first minimum $\tau_\perp$ of the autocorrelation function for $\beta = 0.1$ w.r.t. the number N of active particles. The dashed black line represents $\tau_\perp \sim N^{1/2}$.

We finally proceeded to verify Eq. (2.54), a central result of our Gaussian theory, by comparing the root-mean-square gyration radius R_g^{rms} with the transverse timescale $\tau_\perp$ for flocks characterized by different values of N, β, η, and v_0. Operationally we took the stationary average of R_g^{rms} for a given set of parameters (N, v_0, η), varying β in an interval dependent by N, so that G_g clearly displays underdamped oscillations. We then extracted $\tau_\perp$ as the position of the first minimum in the connected autocorrelations of R_g^2 for each value of β. We repeated this procedure varying the number N of SPPs, their speed v_0 and the amplitude of the noise η. The latter parameter controls the average polarization Φ of the flock with small corrections due to N and β. We then plotted $R_g^{rms} = \sqrt{R_g^2}$ as a function of the respective transverse timescale $\tau_\perp$ properly rescaled by

$$\kappa(v_0, \Phi) = \frac{v_0}{\pi}\sqrt{2\rho_1 c_2(1-\Phi)}\,, \tag{2.65}$$

defined in Eqs. (2.55) and (2.56). Here the average of $\Phi = \Phi(N, v_0, \eta)$ has been computed numerically for every set of parameters. The results are presented in Fig. 2.17, where we plot $R_g^{\rm rms}$ as a function of $\tau_\perp\,\kappa(v_0, \Phi)$. Our results are reported in Fig. 2.17, where each dataset, encoded by a given color and a given marker, represent the gyration radii and their timescale $\tau_\perp$ for different values of the triple (N, v_0, Φ).

As shown in Fig. 2.17, once rescaling the transverse timescale $\tau_\perp$ for κ, all sets of R_g^{rms} corresponding to different values of v_0, Φ, and N approximatively collapse onto a single curve with unit slope. This provides strong numerical evidence supporting the theoretical prediction obtained within the Gaussian zeroth-order approximation.

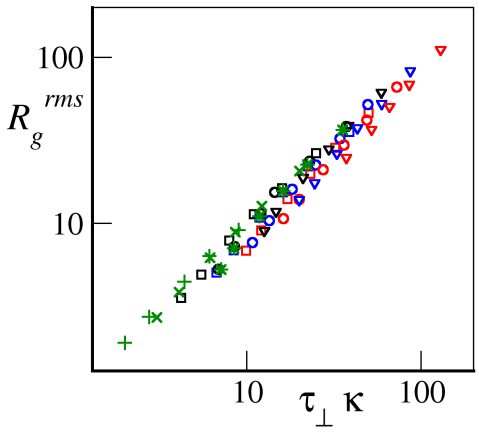

Figure 2.17: **Mean gyration radius as a function of temporal position of the first minimum:** R_g^{rms} vs $\tau_\perp$, properly rescaled by k, defined accordingly to Eqs.(2.55),(2.56). The different values for the parameters v_0, η, N are encoded in the following way: the colors represent the size N (black for $N = 10^3$, blue for $N = 2 \cdot 10^3$ and red for $N = 5 \cdot 10^3$), the shape of the markers encodes for the noise amplitude η (square for $\eta = 0.3$, circle for $\eta = 0.4$ and triangle for $\eta = 0.5$). For all these data we have $v_0 = 0.5$. The green points are all obtained for $\eta = 0.3$ and $N = 10^3$ but using different speed v_0. Plus have $v_0 = 0.15$, crosses $v_0 = 0.3$ and asterisks $v_0 = 1$.

2.3.3 Flocks internal structure

In Sec. 1.5.4, we introduced the pair correlation function $g(r)$, defined as the probability of finding a particle at a distance r from a given reference particle. For clarity, we report its definition here:

$$g(r) = \frac{1}{2\pi r \Delta r} \frac{1}{n_c(r)} \sum_{i=1}^{n_c(r)} \sum_{j \neq i} \delta_{\Delta r}(r - r_{ij}) \,. \tag{2.66}$$

Operationally, $g(r)$ is computed by counting the number of particles within an annulus of radius r and thickness Δr centered around a given particle, dividing by the area of the annulus, $2\pi r \Delta r$, and then averaging over different particles as follows: to minimize finite-size effects, only particles in the bulk of the flock are considered. In particular, particles located too close to the boundary would bias the estimate of $g(r)$. Therefore, when computing $g(r)$ at a given distance r, we include only the $n_c(r)$ particles for which a disk of radius r centered at their position is entirely contained within the flock.

The pair correlation function is a standard tool in condensed matter physics to characterize different states of matter and to infer structural properties of many-body systems. Its application to starling flocks in the wild [18] revealed a largely structureless organization, intermediate between that of a liquid and a gas. We now present the pair correlation function obtained from numerical simulations of our metric-free model and compare it with experimental results [20]. In Fig. 2.18(a), we report $g(r)$ computed for a system with $N = 10^3$ and $\beta = 10^{-2}$. The function is evaluated from a single configuration taken from the stationary regime and averaging only over particles sufficiently far

from the boundary, as discussed above. In practice, the flock boundary is determined by an *Alpha Shape* algorithm using a parameter of two times the typical distance between neighbours. In panel (b), we reproduce the corresponding experimental result from Ref. [20]. As discussed in Section 1.5.4 and also shown in Fig. 2.18(b) for direct comparison, experimental pair correlation functions exhibit a single pronounced peak — corresponding to the shell of nearest neighbors — followed by a nearly featureless decay at larger distances, and a suppression at very short distances due to volume exclusion. These observations indicate that highly ordered states induced by equilibrium-distance interactions, such as the *moving droplet* or the *flying crystal* emerging at large attraction strength, are not consistent with empirical data on starling flocks.

Our model yields a pair correlation function that is consistent with experimental observations. In particular, it displays a single well-defined peak associated with the first shell of topological neighbors—without a fixed metric distance—and remains largely structureless at larger separations, resembling a gas-like organization. At short distances, however, the model does not exhibit a pronounced exclusion zone, as no explicit hard-core repulsion is included. This difference does not significantly affect the large-scale properties of the flock. Notably, this qualitative behavior of $g(r)$ persists also for smaller values of β.

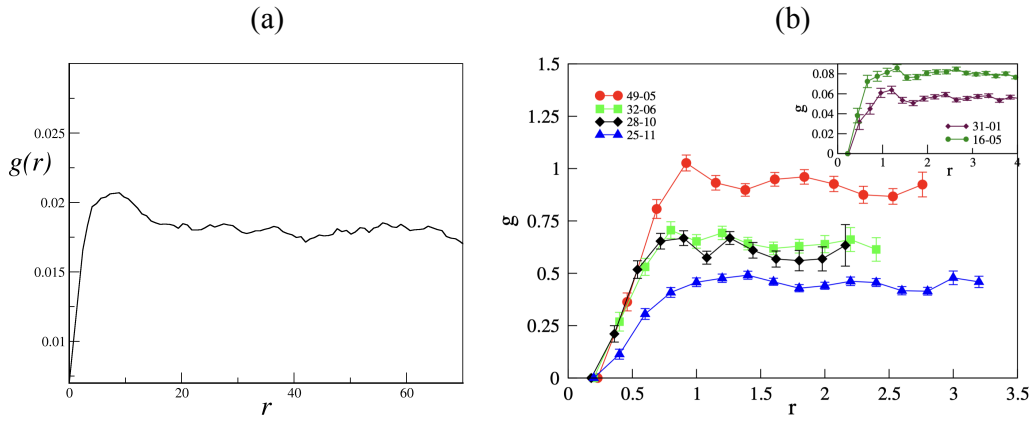

Figure 2.18: **Pair correlation function (a)** Pair correlation function evaluated from numerics performed on a flock of $N = 10^3$ SPPs with $\beta = 10^{-2}$ with our metric-free model. **(b)** Pair correlation function from experimental observation in the field of several flocks with different densities. We reported again the experimental pair correlation function obtained in [20] for a better comparison with the one obtained numerically with our model.

2.3.4 Correlations in velocity fluctuations

From bird flocks to fish schools, animal groups often respond to environmental perturbations in a highly coordinated manner. Such collective response provides a strong adaptive advantage and, as suggested in Ref. [12], may be mediated by scale-free behavioral correlations, enabling the group to achieve

an effective perception range much larger than the actual interaction range between neighbors. As anticipated in Sec. 1.4, this idea is supported by empirical observations in starling flocks, where spatial correlations of velocity fluctuations exhibit a power-law behavior, $C(r) \sim r^{-\gamma}$, as expected in systems that spontaneously break a continuous symmetry.

Previous studies [12, 74] reported values of the exponent γ close to zero, indicating anomalously long-ranged correlations in starling flocks. This behavior contrasts both with equilibrium systems, such as the Heisenberg model (where $\gamma = 1$), and with hydrodynamic theories of flocking, such as the Toner–Tu model, which predicts $\gamma = 6/5$ in 3d and $\gamma = 2/5$ in 2d. These predictions are supported by numerical simulations of topological models in two dimensions [73]. In all these cases, correlations decay faster than in the equilibrium case, whereas in starling flocks the decay is significantly slower, with $\gamma \approx 0$, indicating an almost non-decaying behavior.

In Ref. [74], it was hypothesized that such anomalous scaling of long-range correlations arise from a nonequilibrium mechanism associated with a dynamical information inflow from the boundary to the bulk, associated with the continuous interaction of flocks with the external environment. Supporting this idea, it was shown that applying a small external field to a dynamically changing portion of the boundary of a three-dimensional Heisenberg model leads to a nearly vanishing exponent, consistent with experimental observations.

In this section, we present numerical results for the spatial correlations of velocity fluctuations in our metric-free model, investigating whether the underdamped oscillations observed at the flock boundary can affect the bulk behavior scaling.

For completeness, we briefly recall the relevant definitions from Sec. 1.4. The two-point correlation function for a flock of N particles is defined as

$$C(r) = \frac{1}{C_0} \frac{\sum_{ij} \mathbf{u}_i \cdot \mathbf{u}_j \, \delta(r - r_{ij})}{\sum_{ij} \delta(r - r_{ij})}, \tag{2.67}$$

where

$$\mathbf{u}_i = \mathbf{v}_i - \frac{1}{N} \sum_l \mathbf{v}_l \tag{2.68}$$

represents velocity fluctuations, r_{ij} is the distance between particles i and j, $\delta(r - r_{ij})$ is a smoothed Dirac delta function selecting particle pairs at distance r, and C_0 is a normalization constant.

The correlation length ξ is defined as the first zero of $C(r)$, which necessarily exists since $\sum_i \mathbf{u}_i = 0$ by construction. Empirical observations show that ξ scales linearly with the system size L, implying scale-free correlations. Accordingly, the leading behavior of the correlation function can be written as

$$C(r, L) = \xi(L)^{-\gamma} \, f\left(\frac{r}{\xi(L)}\right), \tag{2.69}$$

where g is a dimensionless scaling function. As discussed in Sec. 1.4, correlations do not possess an intrinsic length scale beyond the trivial system size L.

A practical method to estimate the exponent γ is to evaluate the derivative of the rescaled correlation function at $r/\xi = 1$, which scales as

$$C'(1) \sim \xi^{-\gamma} \sim L^{-\gamma}. \tag{2.70}$$

We numerically compute velocity correlations by averaging over multiple configurations separated by a time interval equal to the autocorrelation time, ensuring statistical independence. We consider a d=2 unperturbed flock with $\beta = 10^{-2}$, $v_0 = 0.5$ and $\eta = 0.3$. The correlation length ξ is extracted as the zero of the averaged correlation function. By evaluating ξ for flocks of different sizes, and using $R_g^{\rm rms}$ as a proxy for the linear size L, we find (see Fig. 2.19(b)) that ξ grows linearly with $R_g^{\rm rms}$, in agreement with both experiments and previous models. This confirms that correlations in our system are scale-free, independently of the attraction strength.

Having verified scale-free behavior, we proceed to estimate the exponent γ that defines the power-law behaviour of the asympthotic ($L \to \infty$ correlation function. The easiest way to do so is by evaluating the derivative of $C(x = r/\xi)$ in $x = 1$ and plotting its absolute value against the linear size of the flock, which behaviour should scale as

$$C'(1) \sim \xi^{-\gamma} \sim L^{-\gamma} \tag{2.71}$$

We computed the spatial correlation function of velocities fluctuations for flocks of different size N and we evaluated the corresponding correlation length ξ. Then, $C'(1)$ has been evaluated as the slope of the curve obtained fitting the rescaled correlation function in $r/\xi = 1$ for all sizes. We plot the results obtained in Fig.2.19(c). The attraction strength has been kept fixed at $\beta = 10^{-2}$.

We observe that $|C'(1)|$ does not exhibit a clear power-law scaling with ξ, a behavior that persists across different values of the attraction strength. A possible explanation lies in the underdamped oscillations at the flock boundary, whichmay strongly affect the scaling of bulk correlations. This mechanism is consistent with the findings of Ref. [74], where a boundary-driven Heisenberg model shows a breakdown of the standard scaling behavior.

To further investigate this similarity, we analyze flocks in the overdamped regime, characterized by small β and small N, where boundary oscillations are suppressed. The corresponding results for $|C'(1)|$ are shown in Fig. 2.19(d), where a power-law behavior with exponent $\gamma \approx 0.15$ is observed. These findings support the idea that boundary effects may alter the bulk scaling, and that stronger global size oscillations lead to a more severe effect. While we currently lack a theoretical explanation, we may conjecture that spontanoeus boundary oscillations play a similar role as the dynamical boundary perturbation considered in Ref.[71].

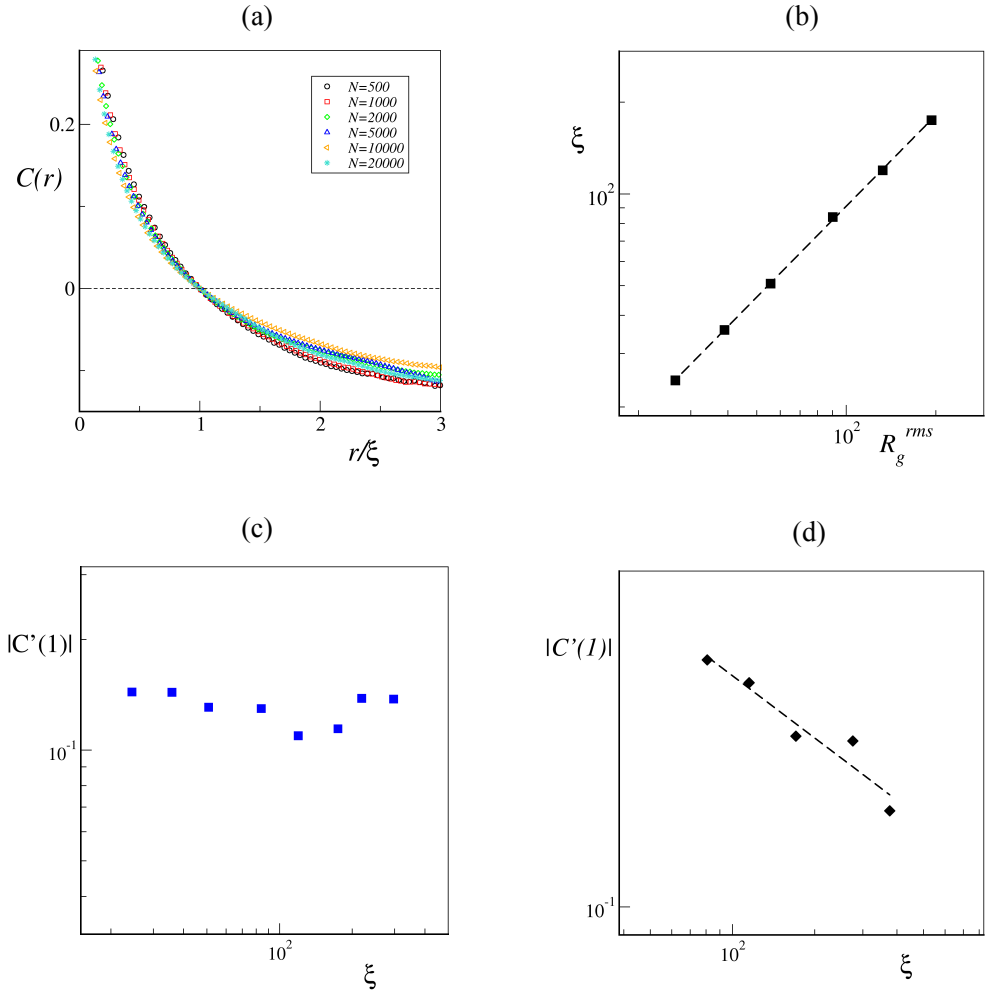

Figure 2.19: **Velocity correlation functions (a)** Correlation function where distances are rescaled by the correlation length ξ for different flocks sizes $N \in [5 \cdot 10^2, 2 \cdot 10^4]$. **(b)** scaling of the correlation length ξ as a function of the root mean squared gyration radius R_g^{rms}. The black dashed lines mark the linear scaling $\xi \sim R_g^{rms}$. **(c)** Modulus of the derivative of $C(x)$ in $x = r/\xi = 1$ for flocks of different sizes as a function of the correlation length, for $\beta = 10^{-2}$. No clear power-law decay is visible. **(d)** Same quantity as in the panel (c) but computed for $\beta = 10^{-3}$, i.e. for flocks without any underdamped oscillation of their boundaries. The dashed black line marks the power-law fit, with scaling exponent $\gamma \approx 0.15$.

2.4 Nonlinear social forces

The choice of a social force scaling linearly with the interparticle distance is motivated by previous studies on biological systems, such as fish schools [70]. However, it is natural to ask how the system behaves in the presence of more general social interactions, characterized by a nonlinear dependence on distance.

In this section, we investigate the static behavior of global size indicators of the flock in the case of a constant cohesive force that doesn't depend on the mutual distance between particles and a force with intensity proportional to the square root of interparticle distance. The analysis is restricted to static

properties, as it is not possible to derive and solve an equation analogous to Eq. 2.32 for nonlinear social forces outside the stationary regime. For this reason, dynamical properties are not considered here.

2.4.1 Transverse approximation for nonlinear social forces

After having carried out in section 2.2.1 the calculations for the linear social force case we now focus ourselves on the case of a nonlinear social torque of the kind

$$\boldsymbol{f}(\mathbf{r}_{ij}) = r_{ij}^{\lambda} \cdot \hat{r}_{ij} = r_{ij}^{\lambda-1} \boldsymbol{r}_{ij} = g(r_{ij})\mathbf{r}_{ij}, \tag{2.72}$$

with $g(r_{ij}) \equiv r_{ij}^{\lambda-1}$ and $\lambda \in [0,1)$, where for $\lambda = 1$ we recover a social torque with intensity growing linearly with the distance. We can rewrite Eq.(2.10) as

$$\dot{\hat{\mathbf{s}}}_i = \boldsymbol{\Theta}_i^{\perp} \left[\gamma \sum_j \mathcal{N}_{ij} \hat{\mathbf{s}}_j + \beta \sum_j \mathcal{N}_{ij} g(r_{ij}) \mathbf{r}_{ij} + \boldsymbol{\xi}_i \right]. \tag{2.73}$$

Again we perform a spin-wave expansion, as in Section 2.2.1 and we introduce the same symmetric Voronoi graph Laplacian defined in (2.16). Projecting onto the direction longitudinal and perpendicular to the mean velocity we obtain an equivalent of Eqs. (2.19)-(2.21), where now Eq.(2.21) reads

$$\dot{\boldsymbol{\pi}}_i = -\gamma \sum_j \mathcal{L}_{ij}\, \boldsymbol{\pi}_j - \beta \sum_j \mathcal{L}_{ij} (\mathbf{x}_j^2 + y_j^2)^{(\lambda-1)/2}\, \mathbf{x}_j + \boldsymbol{\xi}_i^{\perp} + \beta\, \mathbf{b}_i, \tag{2.74}$$

with $\mathbf{b}_i[\boldsymbol{\pi}_i, y_i] = \boldsymbol{\pi}_i \sum_j \mathcal{L}_{ij}\, (\mathbf{x}_j^2 + y_j^2)^{(\lambda-1)/2} y_j$. The calculation is carried out in the same way as in Section 2.2.1 for the dynamics of the fast transverse sector $(\mathbf{x}_i, \boldsymbol{\pi}_i)$, but now the attraction term and the leading order mixing term in (2.74) each carry a factor $g(r_{ij}) = r_{ij}^{\lambda-1}$. In order to obtain an equivalent to Eq.(2.32) however, we have to work in a somehow uncontrolled transverse approximation and disregard the longitudinal spatial separation between particles, that is assuming $x_j \gg y_j$,

$$\begin{aligned} \dot{\boldsymbol{\pi}}_i &= -\gamma \sum_j \mathcal{L}_{ij}\, \boldsymbol{\pi}_j - \beta \sum_j \mathcal{L}_{ij} \mathbf{x}_j^{(\lambda-1)} \cdot\, \mathbf{x}_j + \boldsymbol{\xi}_i^{\perp} + \beta\, \mathbf{b}_i, \\ &= -\gamma \sum_j \mathcal{L}_{ij}\, \boldsymbol{\pi}_j - \beta \sum_j \mathcal{L}_{ij} \mathbf{x}_j^{\lambda} + \boldsymbol{\xi}_i^{\perp} + \beta\, \mathbf{b}_i. \end{aligned} \tag{2.75}$$

We now repeat the same steps carried out in Section 2.2.1. First we substitute the time dependent Voronoi graph Laplacian with its annealed version. Then we approximate the low-lying spectrum of a finite flock with largest linear size L with that of a continuum Laplacian with free boundary conditions and a microscopic scale set by the characteristic neighbour distance a. We get:

$$\dot{\boldsymbol{X}}_k = v_0 \boldsymbol{\Pi}_k, \tag{2.76}$$

$$\dot{\boldsymbol{\Pi}}_k = -\gamma \lambda_k \boldsymbol{\Pi}_k - \beta \lambda_k \mathbf{X}_k^{\lambda} + \boldsymbol{\Xi}_k^{\perp} + \beta\, \mathbf{B}_k\,. \tag{2.77}$$

Combining these two equation we can eliminate the Π variables to get

$$\ddot{\mathbf{X}}_k = -\gamma_k \dot{\mathbf{X}}_k - \beta_k \mathbf{X}_k^{\lambda} + v_0 \boldsymbol{\Xi}_k^{\perp} \,. \tag{2.78}$$

We finally access the static asymptotic behavior of Eq.(2.78) by considering its overdamped limit. In this regime $\dot{\mathbf{X}}_k$ rapidly relaxes to a stationary value and, consequently, we can disregard the term $\ddot{\mathbf{X}}_k$. We are left with the equation

$$\dot{\mathbf{X}}_k = -\frac{\beta_k}{\gamma_k}\mathbf{X}_k^{\lambda} + \frac{v_0}{\gamma_k}\boldsymbol{\Xi}_k^{\perp}. \tag{2.79}$$

By solving the Fokker-Planck equation associated to (2.79) we can find the stationary probability $p(\mathbf{X}_k)$. The associated Fokker-Planck, or *Smoluchowski equation*, reads

$$\frac{\partial p(\mathbf{X}_k,t)}{\partial t} = a\frac{\partial}{\partial \mathbf{X}_k}\left[\mathbf{X}_k^{\lambda} p(\mathbf{X}_k,t)\right] + \frac{b^2}{2}\frac{\partial^2}{\partial \mathbf{X}_k^2} p(\mathbf{X}_k,t), \tag{2.80}$$

with $a = \beta_k/\gamma_k$ and $b = v_0/\gamma_k$. Since we are interested in the stationary probability $p(\mathbf{X}_k)$ such that $\frac{\partial}{\partial t}p(\mathbf{X}_k) = 0$ we obtain

$$\frac{b^2}{2}\frac{d}{d\mathbf{X}_k} p(\mathbf{X}_k) = -a\mathbf{X}_k^{\lambda} p(\mathbf{X}_k). \tag{2.81}$$

Eq. (2.81) can be readily solved to get the normalized probability distribution

$$p(\mathbf{X}_k) = \frac{(\lambda+1)\alpha^{\frac{1}{\lambda+1}}}{\Gamma\left(\frac{1}{\lambda+1}\right)} \exp\left(-\alpha \mathbf{X}_k^{\lambda+1}\right), \tag{2.82}$$

with $\alpha = \frac{2a}{b^2(\lambda+1)}$. We restrict ourselves to the two-dimensional case and we compute the second momentum $\langle X_k^2 \rangle$ that reads

$$\langle X_k^2 \rangle = \int_0^{\infty} X_k^2 \; p(X_k) dX_k \sim \left(\frac{b^2}{2a}\right)^{2/(\lambda+1)} \sim \left(\frac{v_0^2\Gamma}{\beta_k\gamma_k}\right)^{2/(\lambda+1)} \tag{2.83}$$

We now recall that $\gamma_k = \gamma\lambda_k$ and $\beta_k = v_0\beta\lambda_k$, with $\lambda_k = \rho_k/N$ in the $d = 2$ case, we get

$$\langle X_k^2 \rangle \sim \left[\frac{v_0\Gamma N^2}{\beta\gamma}\right]^{\frac{2}{\lambda+1}} \tag{2.84}$$

By making use of Eqs.(2.38), (2.39) and combining them with (2.84), we find that

$$\langle R_{\perp}^2 \rangle \sim \left[\frac{v_0\Gamma N^2}{\gamma\beta}\right]^{\frac{2}{\lambda+1}} \frac{1}{N}. \tag{2.85}$$

For the linear social torque ($\lambda = 1$) the results coincide with the one in Eq.(2.49), while in the other two relevant case, i.e. $\lambda = 0$ and $\lambda = 1/2$ we get, respectively

$$\sqrt{\langle R_g^2 \rangle} \sim \beta^{-1/(\lambda+1)} \sim \beta^{-1}, \tag{2.86}$$

$$\sqrt{\langle R_g^2 \rangle} \sim N^{\frac{3-\lambda}{2(\lambda+1)}} \sim N^{3/2}. \tag{2.87}$$

and

$$\sqrt{\langle R_g^2 \rangle} \sim \beta^{-1/(\lambda+1)} \sim \beta^{-2/3}, \tag{2.88}$$

$$\sqrt{\langle R_g^2 \rangle} \sim N^{\frac{3-\lambda}{2(\lambda+1)}} \sim N^{5/6}. \tag{2.89}$$

2.4.2 Numerical simulations

We numerically test the validity of the relation (2.85) for two different values of the exponent λ, namely $\lambda = 0$ and $\lambda = 1/2$. We consider the root-mean-square gyration radius $R_g^{rms} = \sqrt{\langle R_g^2 \rangle}$. In the transverse approximation one expects $R_g^2 \approx R_\perp^2$ and therefore

$$R_g^{rms} = \sqrt{\langle R_\perp^2 \rangle}. \tag{2.90}$$

For both $\lambda = 0$ and $\lambda = 1/2$, we observe a stationary flocking dynamics with a finite flock extension. As shown in Fig. 2.20, in the case of a distance-independent force ($\lambda = 0$), the scaling of $R_g^{\rm rms}$ with respect to both the attraction strength β (Fig. 2.20(a)) and the number of particles N (Fig. 2.20(b)) exhibits a clear power-law behavior, in good agreement with the theoretical predictions of Sec. 2.4.

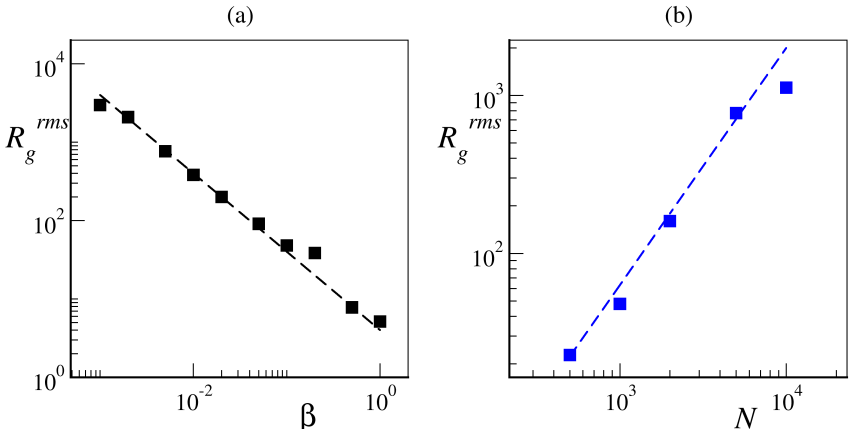

Figure 2.20: **size scaling of flocks for constant forces ($\lambda = 0$) (a)** R_g^{rms} as a function of $\beta \in [10^{-3}, 1]$ for $N = 10^3$ SPPs with social torque of intensity $f(r_{ij}) = 1$. The dashed black line marks the power-law behaviour $R_g^{rms} \sim \beta$ (see Eq.2.86) **(b)** R_g^{rms} for flocks of different size $N \in [5 \cdot 10^2, 10^4]$ with $\beta = 0.1$ fixed. The dashed blue line represent the power-law behaviour predicted analytically (see Eq.2.87).

Numerical simulations for $\lambda = 1/2$, reported in Fig. 2.21, also confirm the scaling $R_g^{\rm rms} \sim \beta^{-2/3}$ predicted by the theory (Fig. 2.21(a)), while deviations

from the predicted scaling with N in Eq. (2.89) are observed (Fig. 2.21(b)), suggesting possible corrections beyond the transverse approximation for large N.

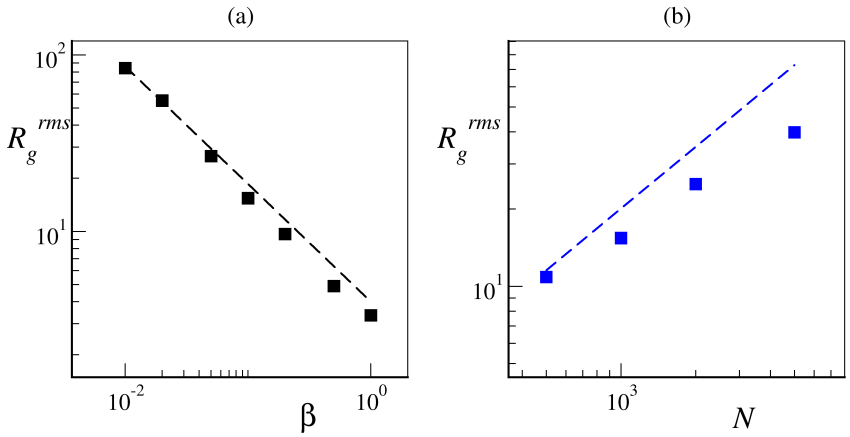

Figure 2.21: **size scaling of flocks for** $\lambda = 0.5$ **(a)** R_g^{rms} as a function of $\beta \in [10^{-2}, 1]$ for $N = 10^3$ SPPs with social torque of intensity $f(r_{ij}) = r_{ij}^{1/2}$. The dashed black line marks power-law scaling, with exponent $\approx 2/3$ predicted by the theory (see Eq. (2.88)). . **(b)** R_g^{rms} for flocks of different size $N \in [5 \cdot 10^2, 10^4]$ with $\beta = 0.1$ fixed. The dashed blue line represent the power-law fit, with exponent 5/6 (see Eq. (2.89)).

Finally, from the autocorrelation functions of the squared gyration radius shown in Fig. 2.22, we observe that the underdamped oscillations characteristic of the linear interaction case are absent for $\lambda = 0$, while for $\lambda = 1/2$ the underdamped behavior is still present albeit in a weaker form.

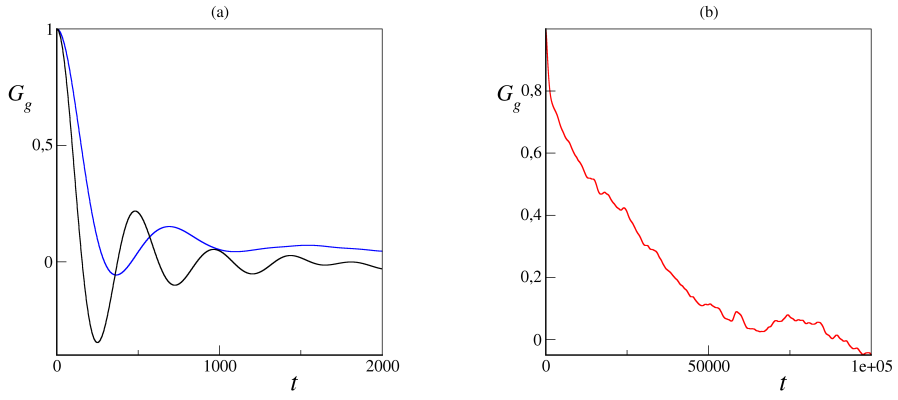

Figure 2.22: **Autocorrelation for different social forces (a)** Autocorrelation G_g for the squared gyration radius R_g^2 for $\beta = 10^{-1}$ and $N = 10^3$ for $\lambda = 1$, i.e. the linear case (in black), $\lambda = 0.5$ (in blue) **(b)** G_g for $\lambda = 0$ (in red).

2.5 Discussion

We have shown that finite cohesive flocks can display underdamped collective shape modes for any non zero attraction strength, despite the purely first-order relaxational microscopic dynamics. Our theory also allows us to formulate a directly observable relation between the typical flock size and its oscillation timescale involving only measurable parameters such as the number of birds, their velocity and the mean polarization of the flock, all easily accessible in experimental observation of starling flocks in the field.

Importantly, the mechanism underlying these underdamped global fluctuations has a completely different origin w.r.t. the inertial spin dynamics introduced in [75] to explain information propagation in turning events of starling flocks.

Our theory is valid in the strongly polarized regime, where alignment dominates cohesion, and relies on an annealed interaction network approximation analogous to linearized hydrodynamics in the context of Toner & Tu theory. In principle, in large systems one should expect corrections due to the well-known breakdown of linearized hydrodynamics; however, we have verified in practice that global shape indicators follow the annealed theory up to at least $N = 10^5$. An appealing extension of our work is indeed a continuum treatment based on Toner–Tu hydrodynamics [5] supplemented by a cohesive restoring stress, as in active polar droplet descriptions [98, 99].

From the analysis of the pair correlation function we could confirm that our finite flocks display a rather structureless correlation function, with a single peak due to the shell of first nearest neighbours and no residue of periodic structure at larger distances, matching experimental observation of starling flocks observed in the field. The analysis of the correlation function of the velocity fluctuations clearly shows that cohesive flocks are scale free, with a correlation length diverging linearly with the linear size of the system. However, no clear power-law behaviour in the form

$$C'(1) \sim L^{-\gamma} \tag{2.91}$$

is observed, confirming the possibility that boundary oscillations may qualitatively alter the scaling behaviour of the bulk, resulting in a much slower decay of the correlation function.

Finally, preliminary investigation of nonlinear attractive forces shows that cohesive flocking is possible for generic pairwise attractive torques which are non-decreasing with the neighbours distance. Several question, however remain open in this case: what about attractive forces decreasing with the distance? Are they able to stabilize the flock extension? Why is the uncontrolled transverse approximation effective in describing the asymptotic flock size scaling, at least for not too large N? And what can be said about the slow modes dynamics for the general nonlinear case?

While much work remains to be done in the general nonlinear case, this is left for future investigations.

Chapter 3

Multi-Agent Reinforcement Flocking in infinite domain

When studying gregarious species that display different collective behaviours, such as the milling of fish schools [70], the aerial display of starling murmurations [69, 100] and the compact swarming of midges [101, 102], a question that naturally arises is why and how such emergent collective behaviours are achieved [103]. Which biological imperatives lead the group target to favour one form of collective motion over the others? It has been argued, for instance, that the flocking state, due to its characteristic long range correlations [20], is highly susceptible and capable of collective reactions to environmental perturbations such as predatory threats. However, quantitative studies of swarming midges show that they can display strong collective behaviour despite the absence of global order [104], with a large capability to collectively respond to perturbations which is comparable to that of highly ordered flock of birds. It is thus difficult to argue that flocking is favoured over swarming for its improved collective response, so that biological function of, and the biological imperatives leading to, flocking as opposed to swarming thus remains elusive.

In this chapter, we try to shed some light on the link between biological imperatives and the local behavioral rules responsible for the emergence of cohesive collective motion through the lens of Multi Agent Reinforcement Learning (MARL). This approach was explored in [105] where it was applied to a group of self-propelled particles in periodic boundary conditions. These findings were corroborated by a theoretical study of mean-field optimal stochastic control in [106]. Here we extend the scope of these earlier works by considering a group in unbounded space. Rather than giving the agents a well defined dynamics for the orientation of their direction of motion (as for what has been done in Chapter 2), we made them learn the best possible combination of pairwise social alignment and cohesion according to a biologically inspired goal function, which parametrizes the urge to stay cohesive while, at the same time, avoiding collisions. We defined this as the "inverse" approach to the weak cohesion problem.

After a brief overview about the theoretical prescription of Reinforcement Learning we present the main techniques used in our work. We show how cohesive polar flocks can arise in groups of active agents that interact trying to avoid both dispersion and overcrowding and how such emergent behaviour can vary when the latter condition is removed. Moreover, we'll show how some characteristic internal structure's features of the emerging flocks are reminiscent of real starling flocks observed in the field.

3.1 An introduction to Reinforcement Learning

Learning by interacting with the environment is perhaps the first thing that comes to mind when one thinks about the nature of the learning process. Feedback to one's actions play a fundamental role in the learning process from the very beginning of a human life: from a child that moves, plays and interacts with objects even in the absence of an explicit teacher, learning from the external cues it perceives from its surroundings, to an adult that improves her/his skills at any given task accumulating experience by trials and errors. Through such feedback, the learner accumulates experience about the consequences of its actions: by observing the resulting states and their cost/reward, it can gradually identify which behaviours are more effective in pursuing the objective encoded by a specific goal function.

Reinforcement Learning (RL) is the branch of machine learning that formalizes this concept of learning by interacting with the environment. In the RL context, an agent learns how to map situations to actions by maximizing a reward signal over time. It is different from *supervised learning* since the agent is not told which actions to take, but it rather discovers, by trial and error, the one that yields the largest cumulative reward. Moreover, RL differs from *unsupervised learning* too, since the latter is typically about finding structure in unlabeled data and completely lacks an explicit *goal* or *reward*.

A key feature of RL is the trade-off between exploration and exploitation. To maximize cumulative reward, an agent must favor actions that have yielded high rewards in the past, while still trying new actions to discover potentially better outcomes. In this sense, the agent must *exploit* its information on high reward actions, so to collect as much reward as possible, but at the same time *explore* in order to take better actions in the future. Since these objectives are inherently in tension, the agent must continuously balance them, gradually favoring actions that appear to be optimal.

3.1.1 The essential ingredients

RL problems are characterized by agents interacting with a dynamic environment. Beyond that, one can identify a set of fundamental elements in this setting: a *policy*, a *reward signal*, a *value function* and, optionally, a *model* for the environment [107].

A *policy* maps the perception an agent has of the state of the environment to the action to be taken in that state. It can be deterministic—always selecting the same action in a given state—or stochastic, assigning probabilities to each possible action.

The *reward signal* defines the goal of the RL problem. At each time step, after the agent chooses an action, it receives a reward, and its only objective is to maximize the cumulative sum of the reward in the long run. In this sense, rewards provide the feedback through which the agent estimates which actions are advantageous in any given state. Rewards are crucial in shaping the policy of the agent as low rewards would discourage certain actions to be taken again

in the future.

In contrast to the reward, which provides an instantaneous feedback, the *value function* determines the long-time desirability of a state. The value function is then the total cumulative reward an agent can expect to accumulate starting from a given state. Whereas the reward represent the immediate desirability of the environmental state, the value function indicates its long-term value, taking into account the states that are likely to follow and the rewards available in such states. It can occur that, even in the case of a poor instantaneous reward, a state could have a high value, since it is followed by states with high rewards. The value function is what we want to maximize in order to obtain more reward in the future.

The last ingredient is the *model* of the environment. It mimics the behaviour of the environment and allows inferences to be made about how it will change when performing a given action in a given state. Methods for solving RL problems that use models and planning are called *model-based* methods, as opposed to *model-free* methods, that are basically explicit trial-and-error learners. Our algorithm, explained in Section 3.3, falls in the latter category, since agents don't have a model of the environment.

3.2 Tabular Methods

We now focus on the RL implementation we have chosen for this work and briefly describe the simplest class of reinforcement learning algorithms: the *tabular methods* [107], where the sets of states and actions are discrete. These problems are typically formalized as finite *Markov Decision Processes* (MDPs), for which a well-developed theoretical framework exists. We introduce their main properties and the quantities needed to solve them, and then present one fundamental solution method: *temporal-difference learning*. Since a rigorous treatment of the RL machinery is beyond the scope of this work, no other techniques will be analyzed other than the essential ones, needed to understand the general framework and the methods used in the following sections.

3.2.1 Markov Decision Processes

MDPs are formalization of sequential decision making, where actions not only influence immediate rewards, but also subsequent states and future rewards. In a MDP, at each time step, the agent interacts with the environment and receives a certain state's representation $S_t \in \mathcal{S}$. On the basis of the sensory input it receives, the agents then performs an action $A_t \in \mathcal{A}(S) = \mathcal{A}$ [1]. In the following time step, the agent receives a reward $R_{t+1} \in \mathcal{R} \subset \mathbb{R}$ and finds itself in the new state S_{t+1}.
Starting from a given state S_0 at $t = 0$, and picking the action A_0 the agent

[1] If the set of possible actions is the same independently of the state of the agent we can simplify a bit the notation and omit the dependence on the state.

will then be in the new state S_1, with a reward R_1. The repetition of such interaction generates a trajectory of the type

$$S_0, A_0, R_1, S_1, A_1, R_2, S_2, A_2, R_3, S_3... \tag{3.1}$$

Since the sets $\mathcal{S}, \mathcal{A}, \mathcal{R}$ are all finite, we can refer to the Markov Decision Processes as *finite* MDPs and, thanks to the markovian property, the probability distribution of states and rewards will only depend on the preceding state-action couple. This means that given a state s at time t and performing an action a, the probability $p(s', r|s, a)$ of receiving a reward r in the new state s' can be written as

$$p(s', r|s, a) \equiv P\left(S_t = s', R_t = r|S_{t-1} = s, A_{t-1} = a\right), \tag{3.2}$$

for every $s, s' \in \mathcal{S}$, $r \in \mathcal{R}$ and $a \in \mathcal{A}$. In a MDP the environment is completely characterized by the probabilities p.

The quantity that the agent tries to maximize is the total expected sum of rewards from time t onward which, in the simplest possible form, could be written as

$$G_t = R_{t+1} + R_{t+2} + R_{t+3} + ... + R_T, \tag{3.3}$$

where we denote with T the final time step. If the task to be learned has no finite final time, as it happens for *continuous task* where $T = \infty$, we have to take into account *discounted* rewards. Agents now aim to maximize the expected sum of discounted rewards, that is, each reward is now weighted by a parameter $\gamma \in [0, 1]$, namely the *discount rate*, to a power s that represents how much in future the given reward occurs from time t:

$$G_t = R_{t+1} + \gamma R_{t+2} + \gamma^2 R_{t+3} + ... = \sum_{s=0}^{\infty} \gamma^s R_{t+s+1}. \tag{3.4}$$

The discount rate γ determines the present value of a reward received in the future: a reward received after s time step will only be worth γ^{s+1} of the same reward received in the present. If $\gamma = 0$ the agent is said to be *myopic*, being it only concerned in maximizing the immediate reward. For $\gamma \in (0, 1)$ the sum in (3.4) has a finite value as long as the sequence of the rewards is bounded. As γ approaches one, the agent takes into account future rewards more and more and finally, for $\gamma = 1$ future rewards have the same weights as immediate ones. In Section 3.3, since concerned only on the immediate reward, we will implicitly assume $\gamma = 0$.

As previously said, the final goal of the agent in almost every RL algorithm is to collect rewards. To do so, the agent finding itself in the state s has to pick, among all the possible actions, the one that guarantees the most reward. The choice of the action given the current state is called *policy* and is the mapping between the states and the actions the agent can take. So if an agent at time t is in the state $S_t = s$, the policy $\pi(a|s)$ gives the probability that, for each action $a \in \mathcal{A}$ the agent will take that action, being in the state s. Our goal is then to find the policy - namely the *optimal policy* $\pi^*(a|s)$ - able to guarantee the largest cumulative reward among all the possible policies by estimating the

so called *value functions*. As we have seen, value functions are functions that estimate how good — or equivalently how bad — a given state is (or a given state-action couple is). The *state-value function* $v_\pi(s)$ of a state s, following policy π is defined as the expected return when starting in s and following the policy π thereafter, and can be written as

$$v_\pi(s) \equiv \mathbb{E}_\pi \left[G_t | S_t = s \right] = \mathbb{E}_\pi \left[\sum_{i=0}^{\infty} \gamma^i R_{t+i+1} \middle| S_t = s \right], \tag{3.5}$$

where $\mathbb{E}_\pi[\cdot]$ is the expectation value of the returns given that the agent follows the policy π from the time step t.
Similarly, the *action-value function* $q_\pi(a, s)$ is defined as the value of taking action a in the state s following the policy π and reads [107]

$$q_\pi(s, a) \equiv \mathbb{E}_\pi \left[G_t | S_t = s, A_t = a \right] = \mathbb{E}_\pi \left[\sum_{i=0}^{\infty} \gamma^i R_{t+i+1} \middle| S_t = s, A_t = a \right]. \tag{3.6}$$

A key concept in the RL framework that allows us to compute and learn state-value functions and action-value function is the *Bellman equation* [108], which comes from the property of value functions to satisfy recursive relations. Since its exact derivation is beyond the scope of this work we simply provide the equation without formally deriving it. For any given policy π and state s the Bellman equation reads

$$v_\pi(s) = \sum_a \pi(a|s) \sum_{s',r} p(s', r|s, a) \left[r + \gamma v_\pi(s') \right], \quad \forall s \in \mathcal{S}. \tag{3.7}$$

Equation (3.7) expresses the relationship between the value of a state and the value of its successive states. The analogous of equation (3.7) holds also for action-value functions $q_\pi(s, a)$ and reads

$$q_\pi(s, a) = \sum_{s',r} p(s', r|s, a) \left[r + \gamma \sum_{s',a'} \pi(a'|s') q_\pi(s', a') \right] \tag{3.8}$$

Since, in this work, we are primarily interested in the latter one, in the remainder of this chapter the term value function will refer to the action-value function, unless stated otherwise.

Optimal policies

We now focus ourselves on how to find the optimal policy. But how can we define optimality? We can make use of the value functions in order to find the optimal policy, in the sense that better policy will grant higher expected returns. In other words, given two policies π and π', we know that $\pi \geq \pi'$ if and only if $q_\pi(a, s) \geq q_{\pi'}(s, a), \ \forall s \in \mathcal{S}, a \in \mathcal{A}$. The optimal policy (in general could be more than one), denoted by π^* is then the policy that will grant the agent the highest expected return

$$q_*(s, a) \equiv \max_\pi q_\pi(s, a), \ \forall s \in \mathcal{S}, a \in \mathcal{A}. \tag{3.9}$$

Invoking the self-consistency condition given by equation (3.7), we can derive from (3.9) the Bellman optimality equation for the action-value function q_* [107]

$$\begin{aligned} q_*(s,a) &= \mathbb{E}\left[R_{t+1} + \gamma \max_{a'} q_*(S_{t+1}, a') \middle| S_t = s, A_t = a\right] \\ &= \sum_{s',r} p(s', r|s, a)\left[r + \gamma \max_{a'} q_*(s', a')\right]. \end{aligned} \tag{3.10}$$

Solving equation (3.10) provides one with the optimal policy, thus solving any given tabular RL problem. However this could prove very difficult since this method relies on three basic assumptions: *i*) a full knowledge of environment dynamics, *ii*) large enough computational resources and *iii*) the Markov property and many cases of interest could lead to a violation of a combination of any of the three latter assumptions. For this reason, in such thorny situations, one has usually to go with approximate methods of solving equation (3.10).

3.2.2 Temporal Difference (TD) learning

Among the many techniques used to approximate value functions such as Dynamic Programming (DP) and Monte Carlo methods (MC) we present here the one that is relevant to the scope of this work, i.e. Temporal Difference (TD) Learning which combines and implements ideas from both DP and MC algorithms [107]. TD methods use trial and error to estimate the value function when we lack a model for the environment, by continuously interacting with environment. Following a given policy π, TD methods update at each time step their estimates V of v_π, see Eq.3.5, in the simplest possible form, according to

$$V(S_t) \leftarrow V(S_t) + \alpha\left[R_{t+1} + \gamma V(S_{t+1}) - V(S_t)\right], \tag{3.11}$$

with $\alpha \in [0, 1]$ being the learning rate. We call this method TD(0) or *one-step* TD. Since TD(0) updates its estimates based on other estimates we say it is a *bootstrapping* method. Moreover, TD methods are said to be *sample updates*, since they need to look ahead to a sample successive state/state-action pair. They use the value of the new state and the reward collected to compute a backed-up value and then update the value of the state/state-action pair accordingly. Finally, we can define the quantity

$$\delta_t \equiv R_{t+1} + \gamma V(S_{t+1}) - V(S_t), \tag{3.12}$$

as the TD-error. δ_t is a sort of error in the sense that it measures how the estimated value $V(S_t)$ differs from the better estimate $R_{t+1} + \gamma V(S_{t+1})$. Since in this work we only deal with the *control* problem, that is finding the optimal policy, we will skip the part of evaluating a policy, i.e. the *prediction* problem. In the next section we give a brief review of the specific control TD algorithm used in the following work, that is the SARSA control algorithm [107].

TD Control: SARSA

Our task is to learn the value $q_\pi(s,a)\ \forall s \in \mathcal{S}, a \in \mathcal{A}$ and the procedure is analogous to the one described in the previous section for the expectation value of v_π. The estimated quantity for the state-action value function is the matrix $Q(s,a)$ and the update rule for the Q-matrix reads

$$Q(S_t,A_t) \leftarrow Q(S_t,A_t) + \alpha\left[R_{t+1} + \gamma Q(S_{t+1},A_{t+1}) - Q(S_t,A_t)\right]. \tag{3.13}$$

The name *Sarsa* arises from the quintuplet State-Action-Reward-State-Action and represents the transition that occurs from a state-action pair to the subsequent one. At each time step we are continuously estimating q_π for a given policy π and, simultaneously changing π in a greedy way. In the following we have a pseudocode that explains the general form of a SARSA algorithm.

SARSA — On-policy TD Control

Initialize: action-value function $Q(s,a)$ arbitrarily for all $s \in \mathcal{S}$, $a \in \mathcal{A}(s)$

Repeat (for each episode):

1. Initialize state S
2. Choose action A from S using policy derived from Q (e.g., ε-greedy)
3. **Repeat (for each step of episode):**
   (a) Take action A, observe reward R and next state S'
   (b) Choose A' from S' using policy derived from Q (e.g., ε-greedy)
   (c) Update:

$$Q(S,A) \leftarrow Q(S,A) + \alpha[R + \gamma Q(S',A') - Q(S,A)]$$

   (d) $S \leftarrow S'$, $A \leftarrow A'$
4. **until** S is terminal

3.2.3 From single to multi-agent reinforcement learning

The theory of RL sketched in the previous section refers to the case of a single agent interacting with the environment. This is obviously not a suitable framework when we tackle behavior problems like flocking, where the number of agents could greatly exceed the hundreds. Luckily, the above results can be easily generalized to the case with a number of agents $N > 1$. Such a generalization falls under the name of *Multi-agent reinforcement learning* (MARL) [105, 106, 109–111]. Now, the representation that agents sense from the environment incorporates also information about other agents (as we will see in our special case, the environmental states encompass information about the direction of motion and about the relative position of the nearest neighbours of each agent). The presence of a wide number of agents, however, slightly changes the nature of learning, since now two scenarios open. Agents could be seen as independent learners, each of them learning separately from the others or they can share the information they acquire during the dynamics, as if they were *hive-minded*. In the former case each agent has its own Q-matrix that gets updated separately from the others: when the i-th agent performs an action and receives a reward, only the i-th Q-matrix gets updated consequently,

accordingly to the scheme we learned in the last section. On the contrary, collaborative learners share the same Q-matrix, in the sense that if an agent picks a given action in a given state receives a reward, every other agents knows what happened and share the same reward storing it in their collective Q-matrix. We call these two different paradigms *Decentralized* and *Centralized Learning* (DT and CT) and in our work both of them will be tested.

3.3 Learning to flock in open space by avoiding collisions and staying together

We investigate the emergence of cohesive flocking in open, boundless space using a multi-agent reinforcement learning framework. Agents integrate positional and orientational information from their closest topological neighbours and learn to balance alignment and attractive interactions by optimizing a local cost function that penalizes both excessive separation and close-range crowding. The resulting Vicsek-like dynamics is robust to algorithmic implementation details and yields cohesive collective motion with high polar order. The optimal policy is dominated by strong aligning interactions when agents are sufficiently close to their neighbours, and a flexible combination of alignment and attraction at larger separations.

3.3.1 Dynamics

We consider N agents moving off-lattice in a 2-dimensional unbounded (that is, infinite) space. The dynamics is parallel and discrete and the agents update their position with the standard streaming rule

$$\mathbf{r}_i^{t+\Delta t} = \mathbf{r}_i^t + v_0 \mathbf{s}_i^{t+\Delta t} \Delta t, \tag{3.14}$$

where $\mathbf{r}_i^t$ is the position of the i-th agent at time t, $\mathbf{s}_i^t$ its unit heading direction and the speed of the agents is kept constant and equal to v_0. In the following, without loss of generality, we put $\Delta t = 1$. Agents only perceive their local environment represented by their topological (i.e. Voronoi) neighbours, the set V_i, a spatially balanced version of metric free interactions that grants optimal stability [18]. They integrate this information into the local average heading direction

$$\mathbf{V}_i^t = \boldsymbol{\theta} \left[\sum_{j \in \mathcal{V}_i} \mathbf{s}_j^t \right] \tag{3.15}$$

and direction to the center of mass of the neighbours

$$\mathbf{R}_i^t = \boldsymbol{\theta} \left[\sum_{j \in \mathcal{V}_i} (\mathbf{r}_j^t - \mathbf{r}_i^t) \right], \tag{3.16}$$

where the sum is over the set $\mathcal{V}_i$ of Voronoi neighbours of the i-th agent. These vectors are normalized to unity by the normalization operator $\boldsymbol{\theta}[\mathbf{v}] \equiv \mathbf{v}/|\mathbf{v}|$. At each time step, agents change their direction of motion, aligning towards

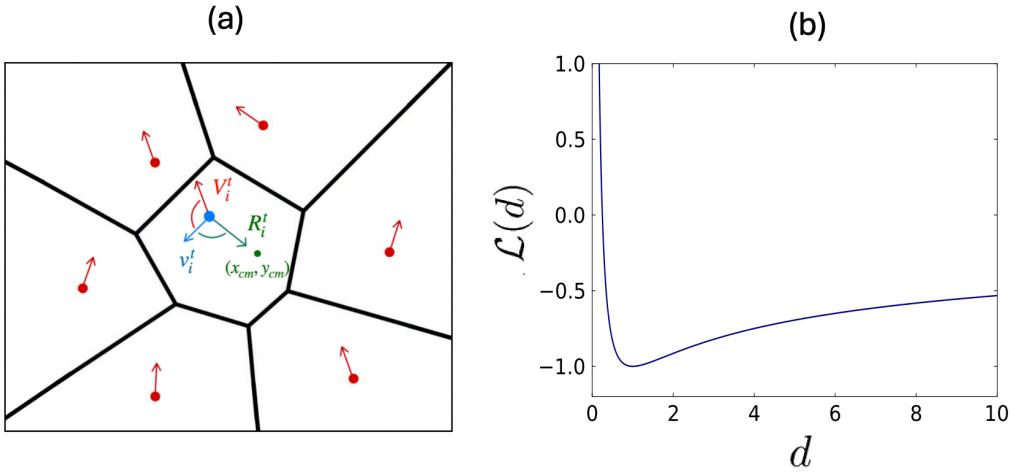

Figure 3.1: (a) Cartoon describing the orientational dynamics of agents. At each step the i-th agent (blue arrow) chooses the new direction given the information it perceives from its topological neighbours (red arrows) and linearly weights the alignment to the neighbours' mean direction V_i^t and to the direction R_i^t to the local center of mass. Nearest neighbours are evaluated via Voronoi tessellation. (b) The cost function (3.21) with parameters $a = 1$ and $b = 2$.

a combination of the two vectors above, weighted by a (learnable and state-dependent) relative coupling strength parameter $\beta \in [0, 1]$, with

$$\mathbf{s}_i^{t+1} = \Theta\left[(1-\beta)\mathbf{V}_i^t + \beta\mathbf{R}_i^t + \eta\xi_i^t\right], \tag{3.17}$$

where ξ_i^t is a random unit vector with zero mean and correlations,

$$\langle \xi_i^t \cdot \xi_j^{t'} \rangle = \delta_{ij}\delta_{t,t'} \,. \tag{3.18}$$

Agents first update their heading via Eq. (3.17) and then their position by Eq. (3.14), a sketch of the dynamics is given in Fig. 3.1(a). Note that for $\beta = 0$ this rule reduces to the standard Vicsek model with topological interactions [73], while $\beta = 1$ gives complete attraction towards the center of mass of local neighbours, that is an attraction dominated dynamics. The relative coupling strength is thus the crucial parameter that will be optimized via the reinforcement learning algorithm described in the next subsection. Note finally that attractive forces are expressed as an (overdamped) torque acting on the particles heading as in Ref. [112], so that particles heading always coincides with their direction of motion, a framework suitable for active agents that interact via social forces without physical collisions.

3.3.2 MARL Framework

In multi-agent RL, different agents interact between themselves and with the environment. See Refs. [105, 109–111, 113] for previous applications to active matter dynamics.

In this work we apply two different learning paradigms: centralized training (CT) and decentralized training (DT). In the former, agents act independently

one from the other, but learn by shared experience – as if they were *hive-minded* – while in the latter each agent learns its own policy independently, based solely on the sequence of states, actions and reward experienced by that specific agent.

The raw observation of each agent i is given by the relative positions and headings of its Voronoi neighbours, while its *policy observation* (i.e. the information on which the policy is conditioned) is given by the mean distance of agent i to its local neighbours,

$$d_i = \frac{1}{m_i} \sum_{j \in \mathcal{V}_i} |\mathbf{r}_j^t - \mathbf{r}_i^t|, \tag{3.19}$$

where m_i is the cardinality of the set $\mathcal{V}_i$ of Voronoi neighbours. Actions amount to the choice of a specific value for the relative coupling strength β with which the agent performs one step of the dynamics (3.17)-(3.14).

With a slight abuse of terminology, in the following we will use the term "state" for the policy observation d_i (not to be confused with the *microscopic agent state* $(\mathbf{r}_i, \mathbf{s}_i)$), and denote the chosen β with the term "action". This is a standard use in RL where one speaks generically of state/action pairs. For the sake of simplicity, we also discretize both the states and the actions in order to have a finite number of states n_s and a finite number of possible actions n_a, avoiding the unnecessary computational complexity associated with continuous states and actions (we describe the details of the discretization in Section 3.4).

State-action pairs are thus a discrete set of pairs (d, β) defining the entries of the so-called Q-matrix that in RL represents the estimate for the expected cost for each state-action pair and thus determines the optimal policy

$$\beta^*(d) = \arg\min_{\beta} Q(d, \beta)\,. \tag{3.20}$$

We first discuss how the cost is encoded in the Q matrix and afterwards how actions are selected during learning. The goal we impose to our agent group is to maintain cohesion while, at the same time, avoiding collision risks between agents (that is relative distances getting too small). Therefore, in order to evaluate the performance of the state-action pair, we adopted a cost function in the form of a gentler version of a Lennard-Jones-like potential:

$$\mathcal{L}(d) = \frac{a}{d} - \frac{b}{\sqrt{d}} \tag{3.21}$$

which is non-convex, with a negative minimum in $d_1 = (2a/b)^2$, a positive divergence for $d \to 0$ and a vanishing cost for $d \to \infty$ (see Fig. 3.1b). Here, the argument of the cost function is the agent's mean distance to its nearest neighbours d (we discuss other choices below). We fix the coefficients $a = 1$, $b = 2$, thus fixing the minimum of the potential in $\bar{d} = 1$. The cost/reward for the state-action pair is then:

$$c_i^{t+1} = \mathcal{L}(d_i^{t+1}) - \mathcal{L}(d_i^t), \tag{3.22}$$

where the cost functions are evaluated before (at time t) and after (at time $t+1$) the entire group of N agents updated its position and heading according to Eqs. (3.17) and (3.14). The difference c_i^t in Eq. (3.22) can be, of course, both negative (reward) or positive (cost).

First consider the decentralized training (DT) paradigm, where each agent is characterized by a different Q_i matrix. At each time-step t, agent i chooses an action β_i according to its state d_i, evolves its position and heading via Eqs. (3.14)-(3.17), and computes the corresponding cost (3.22). The Q_i-matrix element corresponding to a chosen state-action couple (d, β) is updated according to the following update rule

$$Q_i^{t+1}(d,\beta) = Q_i^t(d,\beta) + \alpha(d,\beta)[c_i^{t+1} - Q_i^t(d,\beta)], \tag{3.23}$$

where we initialize the Q_i^0 matrices to 0 and the learning rate α_i decays as training proceeds according to

$$\alpha_i(d,\beta) = \frac{\alpha_0}{(1+\Omega_i(d,\beta)/\Omega_0)^\omega}, \tag{3.24}$$

with $\alpha_0 \ll 1$ and $\omega \in (0.5, 1)$ [114] the so-called learning exponent. The frequency matrix $\Omega_i(d,\beta)$ is the number of times the agent visited that particular state-action pair during the entire learning procedure and Ω_0 is a frequency normalization. When an agent selects a state-action couple (d,β) the information it will learn will be weighted less the more often that state-action couple has been visited. This ensures the convergence of the Q-matrix towards a stationary state.

The goal of RL agents is to minimize the cumulative cost they collect over time, and typically this may be done by choosing the current optimal action via Eq. (3.20). On the other hand, agents need to explore all the possible combinations of states and actions in order to find the real optimum. The *exploration-exploitation tradeoff* is a central topic in RL algorithms and, in order to be correctly addressed, one needs to balance the two paradigms correctly. For this reason we decided to induce exploration of new state-action pairs using the so called $\epsilon - greedy$ exploration scheme. At each time step, agents choose the current optimal action (3.20) with probability $p = 1 - \epsilon_i(d,\beta)$ or, with complementary probability $\epsilon_i(d,\beta)$ a random action β chosen with equal probability between the n_a different options. The *exploration rate* ϵ_i is a function of state-actions pairs and decreases during learning according to the decay rule

$$\epsilon_i(d,\beta) = (1+\Omega_i(d,\beta)/\Omega_0)^{-\nu}, \tag{3.25}$$

with an exploration exponent $\nu \in (0,1)$ [114]. Random exploration avoids the training dynamics to be stuck in sub-optimal minima; analogously to the learning rate, the exploration rate decays towards zero as state action pairs are repeatedly visited, ensuring convergence of the learning algorithm.
Learning is typically organized in n_e training episodes of T time-steps (in a time step all agent evolve once with a synchronous dynamics), with the initial positions and headings of the agents reinitialized at the beginning of each

episode. The Q-matrices, learning rates and exploration rates, of course, are not reinitialized every episode. At the end of learning, one expects the Q-matrices to have practically converged towards a stationary state and one can define a learned dynamics where agents always select the optimal action for each given state via Eq. (3.20).

Centralized training (CT) follows the same procedure, but in this case agents share the same information during learning, with single Q and frequency matrices, $Q_i = Q$, $\Omega_i = \Omega$ and learning and exploration rates, $\alpha_i = \alpha$, $\epsilon_i = \epsilon$, $\forall i$.

3.4 Results

Learning is performed over n_e training episodes, each of a duration of $T = 20N$ time steps. We discretize actions and states with $\Delta\beta = 1/(n_a - 1)$ and $n_a = 11$ actions and $\Delta d = 0.2$ with $n_d = 20$ different possible states (the 20th state also encodes for mean neighbours distances $d > 20\Delta d = 4$). We have verified that our results are robust with respect to reasonable increases in n_d and n_a. For what concerns the learning parameters introduced in the previous section, we have performed a preliminary exploration of different values in the convergence windows of RL theory [114] in order to adapt them to our specific problem. While we cannot claim optimality in a rigorous sense, we have settled for $\alpha_0 = 0.005$, $\Omega_0 = N$ and $\nu = \omega = 0.7$ for centralized training. These choices seem to grant a sufficiently fast convergence towards a stationary state, with fairly robust results w.r.t. small changes in these parameters. As we will show in Sec. 3.4.1, decentralized training is more delicate. For sufficiently small flocks, $N < 800$, these parameters, with the frequency normalization $\Omega_0 = 100$ are still efficient, while for larger flocks we obtained better cohesion with $\nu = 0.5$ and $\omega = 0.99$.

At the beginning of each training episode the agents' positions and headings are randomly reinitialized (for the positions we uniformly distribute the agents in a circle with a radius $R_0 = 10\sqrt{2}$) but of course they keep track of what they learned so far (the Q matrix is not reinitialized). Unless differently stated, we also fix $v_0 = 0.2$ and $\eta = 0.3$ in the agents dynamics.

3.4.1 Onset of cohesive flocking

We have verified numerically that our RL algorithm leads to a state of cohesive flocking in a relatively small number of training episodes, both in the CT and DT paradigms. In particular, flocking alignment is quantified as usual via the scalar polar order parameter (OP)

$$\Phi(t) = \frac{1}{N}\left|\sum_{i=1}^{N} \mathbf{s}_i^t\right| . \tag{3.26}$$

For an ordered ensemble of mutually correlated agent headings $\Phi(t)$ is finite and of order one, while it tends to zero for uncorrelated and disordered headings. In finite flocks, in the latter case one has indeed $\Phi(t) \sim 1/\sqrt{N}$ due to

finite fluctuations. Furthermore, group cohesion can be assessed via the mean distance to the group center of mass (MDCM) which estimates the typical flock size

$$\Gamma(t) = \frac{1}{N}\sum_{i=1}^{N} |\mathbf{r}_i^t - \mathbf{r}_{cm}^t| \tag{3.27}$$

with

$$\mathbf{r}_{cm}^t = \frac{1}{N}\sum_{i=1}^{N} \mathbf{r}_i^t \,. \tag{3.28}$$

Cohesive groups will be therefore characterized by a finite stationary $\Gamma(t)$, which will otherwise grow unbounded in the absence of group cohesion. For instance, for purely alignment interactions with topological neighbours one has $\Gamma(t) \sim \sqrt{t}$ [73].

We first consider groups of $N = 100$ agents. The MDCM and OP timeseries during the last episode of training are (respectively) reported in the main panels of Fig. 3.2(a)-(b). Blue curves have been obtained by centralized training, while red ones via decentralized one. Cohesive collective motion, with $\Gamma \approx 2$ and $\langle\Phi\rangle_t \approx 0.95$, is obtained with both training protocols. This high ordered regime is indeed characteristic of starling flocks observed in the wild [20]. Training is notably efficient, as evidenced by the single-episode averages $\langle\Gamma\rangle_t$ and $\langle\Phi\rangle_t$ of MDCM and OP – reported in the insets of Fig. 3.2(a)-(b) – that settle to their final values after around 30 episodes for CT. DT, on the other hand, requires more training episodes to reach the final trained state, especially for what concerns the saturation of the typical size Γ to a stationary value.

We established the scaling of our training algorithm with the number of agents testing groups up to $N = 1600$ agents (a typical size for starling flocks observed in the field [20]). As shown in Fig. 3.2(c), the average OP at the end of training for CT converges towards a finite asymptotic value $\Phi \approx 0.94$, while the flock size Γ grows like $\sqrt{N}$, signaling that the flock density remains constant as the group size is varied. Decentralized training, on the other hand, seems to be less robust, with $\Phi \approx 0.84$ and a large flock size Γ signaling a partial loss of cohesion at $N = 1600$. This is due to the increasing difficulties of individual agents to explore the full range of states d_i in a finite time when N is increased. In practice, some agents do not learn an optimal policy in a reasonable training time. This difficulty may be partially mitigated by a change of the exploration ($\nu = 0.5$) and learning ($\omega = 0.99$) exponents, a choice that increases the late time exploration rate at the expense of a faster decreasing learning rate. As shown in Fig. 3.2, these values lead to nearly identical results for $N < 800$ but result in better cohesion at larger system sizes. A more careful analysis of the finite size scaling of training in the DT regime is left for future work.

We have also verified that the order parameter decreases with increasing noise amplitude, with a transition towards swarming behavior ($\Phi \approx 1/\sqrt{N}$) at $\eta_c \approx 1$. A detailed investigation of this transition is however beyond the scope of this work.

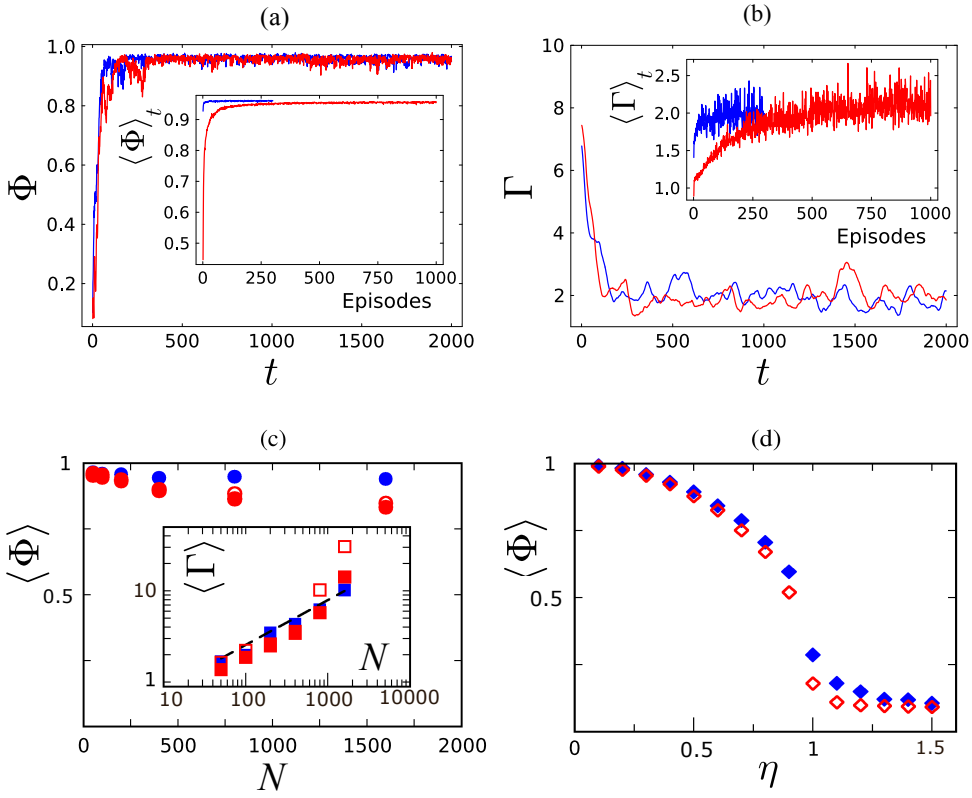

Figure 3.2: Mean distance to the centre of mass (MDCM) and order parameter (OP) for both centralized (CT) (blue, $n_e = 300$) and decentralized (DT) training (red, $n_e = 1000$). (a) MDCM in the last training episode for a group of $N = 100$ agents. (b) OP in the last training episode ($N = 100$). Insets in (a) and (b) are averages over single episodes. (c) Finite size scaling of the average OP. Inset: Finite size scaling of the average MDCM, the dashed black line marks the power law $\sim \sqrt{N}$. (d) OP vs. noise amplitude for $N = 100$. In panels (c)-(d) open red symbols refer to DT with $\nu = \omega = 0.7$, while full red symbols to DT with $\nu = 0.5$ and $\omega = 0.99$.

3.4.2 Flock Structure

We characterized the structure of cohesive flocks, showing that our flocks behave as a rather structureless nonequilibrium liquid, with a finite neighbours exchange rate [82] and a pair distribution function qualitatively matching experimental observations in starling flocks [69].

The relative positions of birds in a flock are not fixed, and they are known to exchange neighbours similarly to what happens in an ordinary liquid. Such an exchange can be quantified by the mixing rate [71]

$$\mu = \frac{1}{N}\sum_{i}^{N}\frac{1}{m_i}\sum_{j}^{N}|W_{ij}(t+1) - W_{ij}(t)| \tag{3.29}$$

with the adjacency matrix $W_{ij}(t) = 1$ if agents i and j are topological neighbours at time t and 0 otherwise. A non-zero mixing rate implies neighbour exchange and an irreversible, nonequilibrium dynamics [13]. Indeed, it can be shown that the entropy production rate of Vicsek-like models is proportional to such a mixing rate [81]. The mixing rates measured in our trained

flocks are small but finite, $\mu \approx 5 \cdot 10^{-2}$ for the typical parameters considered in this work. Particles do flow, but their neighbour rearrangement occurs on a much slower timescale than local alignment, consistently with the state of local quasi-equilibrium observed in starling flocks [82].

The structure of a group can be further investigated by the *radial pair distribution function* $g(r)$ which measures the typical probability of finding a particle at distance r from a reference particle and its definition is given in Eq.(1.65).

To compute it, we used the same procedure depicted in Section 2.3.3, again defining the border particles via an α-shape algorithm [115] with a scale parameter equal to 3 times the mean neighbour distance $d_{nn} = \langle d_i \rangle$.

A typical pair distribution function for a trained flock of $N = 400$ agents is reported in Fig. 3.3(a). It presents a single peak at $r \approx 0.5$ and no further structure, in qualitative agreement with experimental observation in starling flocks [18, 20] whose $g(r)$ also lacks the oscillating behavior of typical liquids, see for instance Fig.1.8. The only peak we observe is a consequence of a well defined peak in the mean neighbour distance distribution (see Fig. 3.3(b)) and is due to the effective repulsion discussed in Sec. 3.4.3 and a further repulsive effect due to noisy fluctuations in the orientation [116]. Moreover, the pair correlation function in Fig.3.3 displays a good qualitative agreement with the one presented in Fig. 2.18 for in silico flocking realizations using the metric free model. The cohesive groups produced by both numerical procedures seem to display the same structural features of real starling flocks.

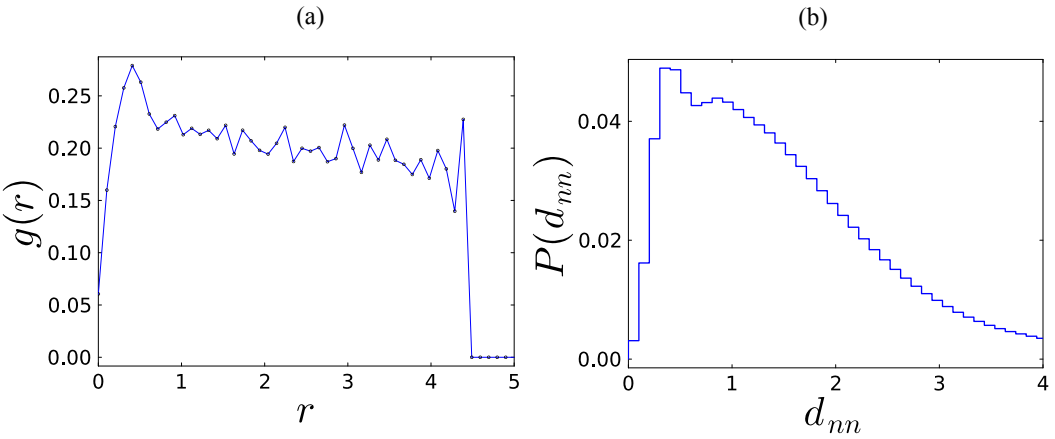

Figure 3.3: (a) Radial pair distribution function measured for a single configuration in a system of $N = 400$ agents trained in the CT regime. Here $\Delta r = 0.05$. (b) Probability distribution of the distance of the nearest neighbours obtained from the last episode of the same simulation. For a comparison with pair correlation functions obtained for starling flocks in the field and for in silico reproduction using our metric-free version of the VM, see for instance Figs. 1.8,2.18.

3.4.3 Analysis of the Q-matrix

In order to discuss in detail the cohesive flocking rule learned by our agents, we now analyze the trained Q-matrix obtained after n_e episodes.

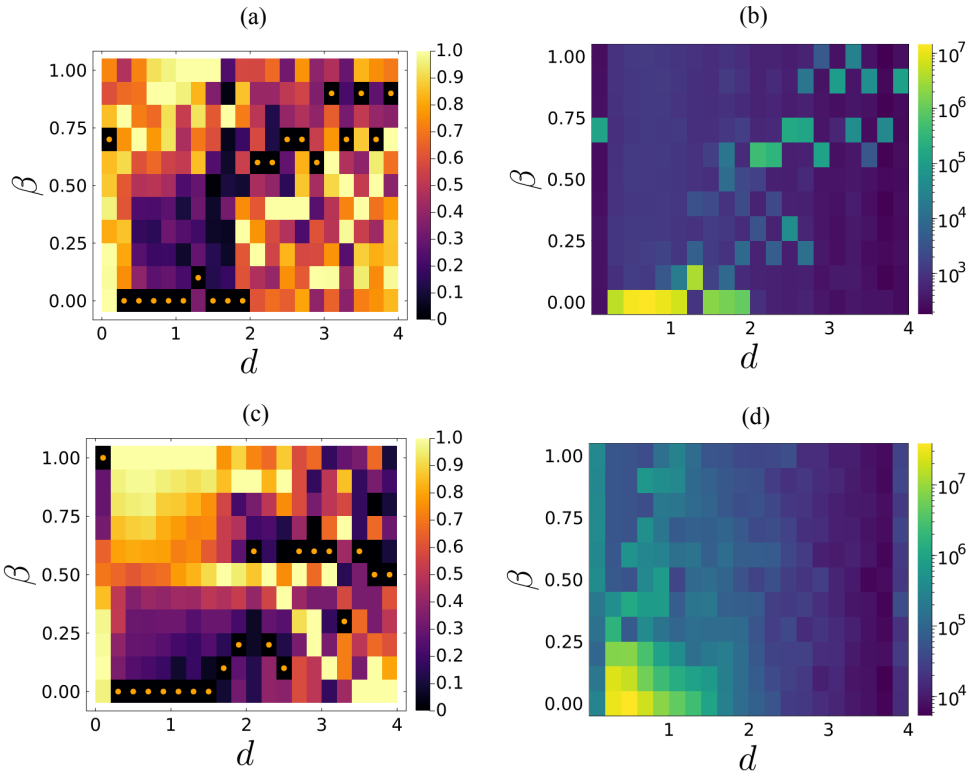

Figure 3.4: **(a)** Trained Q-matrix of the agents for CT after $n_e = 300$ episodes. Dots mark the state-action pairs that minimize the matrix for each state. For better visualization, we show the (state-by-state) normalized matrix $\tilde{Q}(d,\beta) \equiv [Q(d,\beta) - Q^m(d)]/[Q^M(d) - Q^m(d)] \in [0,1]$, where $Q^m(d) = \min_\beta\{Q(d,\beta)\}$ and $Q^M(d) = \max_\beta\{Q(d,\beta)\}$ are respectively the minimum and the maximum values for the state d. (b) Final frequency matrix Ω of the state-action pairs for CT. (c) Trained Q-matrix $\langle Q_i\rangle_i$, averaged over all agents for DT after $n_e = 1000$ episodes, normalized as in (a). (d) Final total frequency matrix $\sum_i \Omega_i$ for DT. In panels (a) and (c) the optimal policies (see Eq. 3.20) are marked by orange dots. $N = 100$ in all panels.

The (normalized) final Q-matrices for CT and DT are shown (respectively) in Fig. 3.4(a) and Fig. 3.4(c) for $N = 100$. They are characterized by two main regimes, a first one for states $d > d^* \approx 2$ and a second one at shorter distances, $d < d^*$. At large mean distances to neighbours, the optimal actions for the agents, given by Eq. (3.20), involve a combination of alignment with, and attraction to, their neighbours, with β seemingly randomly scattered in the interval $(0, 1]$.

Alignment ($\beta \approx 0$), on the other hand, is clearly favoured at smaller distances, $d < d^*$. Contrary to the large distances case, we have verified that strong alignment at short distances is essential for the onset of flocking behavior. The threshold d^* between these two regimes may slightly change between different training runs due to the stochastic nature of the ϵ-greedy scheme, but it is not too far from the cost function inflection point (where the slope changes sign) located at $d = 64a^2/(9b^2) = 16/9$. It is also interesting to note that the onset of these two different strategies is somehow reminiscent of the distance-dependent behavioral zones assumed in various early flocking models [11, 19, 117, 118].

Note finally the exception of the first state, $d < \Delta d = 0.2$, where attraction seems to be the optimal action in both CT and DT. This rather puzzling result is a consequence of the discrete nature of our dynamics: when $d < \bar{d}$ the cost function rewards actions that increase the mean distance to neighbours d and penalizes those that further reduce it. For $d > v_0$ this simply rules out attraction, resulting in agents with commonly aligned headings that separate slowly due to noisy fluctuations in their individual headings. However, when extremely close, $d \leq v_0$, strong attraction may lead to large differences in neighbours' heading, so that nearby agents may easily pass each other and find themselves, after a single time-step, separated by a larger distance. In practice, at distances smaller than v_0, large β may act like an effective repulsion and be favored by the diverging cost function.

We have indeed verified that, for a reduced speed $v_0 \ll \Delta d$ (in particular, we have chosen $v_0 = 0.05$), this effect is largely mitigated, with a typical optimal policy for the smallest mean neighbour distance state ($d < \Delta d$) dominated by alignment, $\beta \in [0, 0.2]$. In Section 3.4.4 we further show that forcing $\beta = 0$ for $d < v_0$ still leads to cohesive flocking.

Note finally that the total CT and DT frequency matrices, reported in Figs. 3.4b-d, show that agents predominantly visit state-action pairs characterized by a relatively short distance to neighbours and strong aligning interactions.

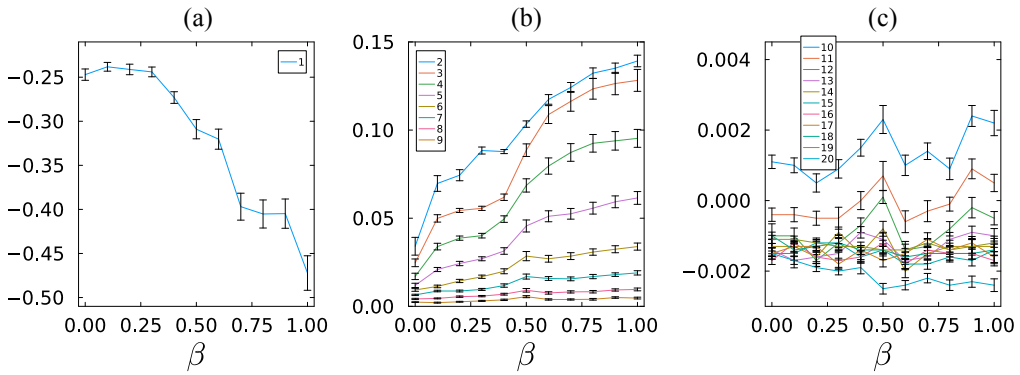

Figure 3.5: Representation of the average Q-matrix $\bar{Q} = \langle Q_i \rangle_i$ trained in the DT scheme for $N = 100$ agents. Each plot, labeled by an integer n refers to a specific state $d = n\Delta d$ and shows $\bar{Q}(d, \beta)$ as a function of β. Error bars represent one standard error.

3.4.4 Policy distillation

A detailed analysis of the trained (and averaged over all agents for the DT scheme) Q-matrix state-by-state (see for instance Fig. 3.5) shows that it is characterized by a well-defined minimum only for small mean neighbour distances. This shows that for $d < d^*$ training strongly converges towards a well-defined optimal policy of fully aligning interactions (with the only exception of the case $d < v_0$ as discussed in Sec. 3.4.3). For $d > d^*$, on the other hand, absolute minima are not well defined, and indeed one can verify that at large distances different training instances do not always converge towards the same optimal policy $\beta^*(d)$. This suggests that, as long as some degree of attractive interaction is present, the exact value of the policy $\beta^*(d)$ is unimportant at large distances.

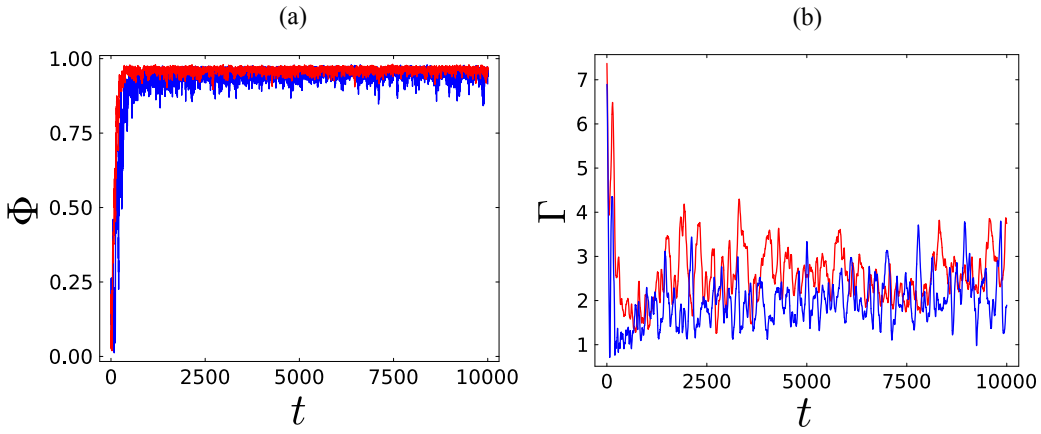

Figure 3.6: Time-series of the order parameter Φ (a) and flock size Γ for $N = 100$ agents with two different policy distillations (see text): Random policy for $d > d^*$ (blue curves) and complete aligning interaction for $d < v_0$ (red curves).

To verify this conjecture, we have considered the optimal policy generated by the usual CT training but, for $d > d^*$, we replaced $\beta^*(d)$ with a random value uniformly distributed in $[0, 1]$. We have verified that the resulting dynamics shows cohesive flocking and it is qualitatively analogous to the one generated by the original optimal policy, as evidenced by the OP and MDCM time-series shown in red in Fig. 3.6.

An analogous policy distillation can be performed to remove strong attraction arising for $d < v_0$, as shown in the top left panel of Fig. 3.5. We have verified that substituting the attractive optimal policy selected by training with pure alignment ($\beta = 0$) still results in cohesive flocking (see Fig. 3.6, red curves), albeit with a slightly larger order parameter and smaller flock size due to the lack of the effective repulsion discussed in Sec. 3.4.3).

3.4.5 A swarming counterexample

We conclude by discussing the role of the cost function (3.21) divergence at short distances in the onset of flocking behavior. Such a divergence can be removed by considering instead $\mathcal{L}(d+z)$ with a positive shift z. In particular, with the choice $z = \bar{d} = 1$ the minimum of the cost function is shifted to

$d = 0$, completely removing penalties for arbitrarily small agent distances d. We have verified, as shown in Fig. 3.7, that this choice suppresses flocking and only leads to cohesive swarming. The analysis of the trained Q-matrix indeed shows that in this case the orientational dynamics is dominated by attraction ($\beta \approx 1$).

However, a diverging cost function is not a necessary condition for flocking, which also appears for finite but sufficiently large penalties at small d. In Fig. 3.7(b) we show how flocking is sustained up to a shift value of around $z_c \approx 0.6$. A detailed investigation of the transition from flocking to swarming as the shift control parameter is varied is beyond the scope of this paper.

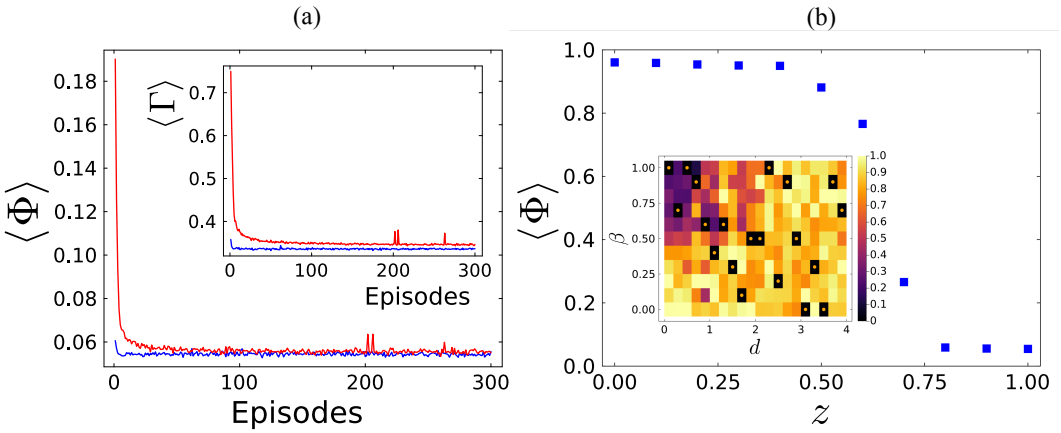

Figure 3.7: (a) Order parameter averaged over single episodes for $z = 1$ and CT (blue curves) and DT (red curves) schemes. Inset: Episode averaged MDCM for the same simulations. (b) Stationary order parameter for different shifting parameter z and CT scheme. Inset: trained Q-matrix for CT and $z = 1$. $N = 100$ in both panels.

3.4.6 Boundary agents and Voronoi based cost

So far we have evaluated the cost function (3.21) on the mean distance to Voronoi neighbors (3.22). This choice, however, does not distinguish between agents positioned at the boundary and those at the interior of the group. However, one may argue that, from the behavioral standpoint of protection from predators [119], agents may have a preference for the latter positions. In order to test this idea, we have chosen the area of the agents' Voronoi cells as the argument of their cost functions. If $\mathcal{A}_i^t$ is the area of the Voronoi cell of agent i at time t, the new cost/reward for state-action pairs is now computed as

$$c_i^{t+1} = \mathcal{L}(\mathcal{A}_i^{t+1}) - \mathcal{L}(\mathcal{A}_i^t)\,, \tag{3.30}$$

with the convenient choice of cost function parameters $a = \pi/4$ and $b = \sqrt{\pi}$, which fixes the minimum of the cost function at $\bar{\mathcal{A}} = \pi/4$.

Since Voronoi cells at the group boundary have, by definition, an infinite area, corresponding to a vanishing cost function $\mathcal{L}$, our new choice highlights the cost/reward difference between agents located inside and those at the boundary of the flock. Therefore, actions resulting in agents moving from the boundary to the interior of the group will be strongly rewarded, while moving from the interior to the border is strongly penalized. Moreover, agents at the boundary get zero cost/reward for any action that does not move them to the inside of the flock, regardless of any change in the distance to their Voronoi neighbours. We have numerically tested this new learning scheme both for centralized and decentralized training, but we have not found any qualitative difference with cost/rewards based on the distance to neighbours, with agents still learning similar optimal policies leading to cohesive flocking, as shown for instance in Fig. 3.8.

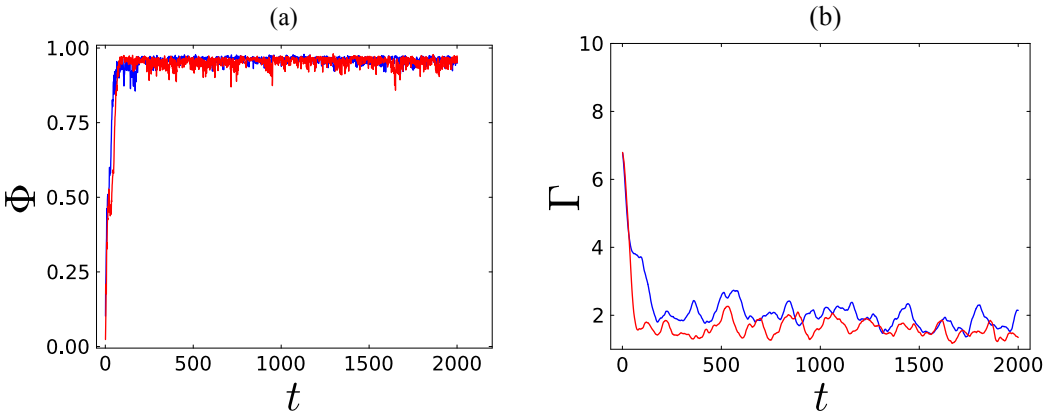

Figure 3.8: Comparison between the optimal policy dynamics of flocks of $N = 100$ agents trained in the CT paradigm with cost functions based on mean distance (blue) or Voronoi area (red). (a) Scalar order parameter vs. time. (b) Flock size vs. time.

3.5 Discussion

Using a reinforcement learning framework for a finite group in a boundless space, we demonstrated that cohesive collective motion with high polar order

can arise from agents learning to avoid both excessive separation and crowding. While the former requirement is needed to avoid dispersion of the group, the latter condition proved essential for the onset of collective motion: when penalties for small inter-agent distances are removed, the learned strategy shifts toward attractive interactions and results in a disordered swarming state.

Interestingly, the learned flocking dynamics shows characteristic structural features, such as a slow mixing rate and a structureless pair distribution function, reminiscent of natural bird flocks, reinforcing the biological plausibility of the learned behavior. While our results have been obtained in two spatial dimensions, one should remember that, due to the presence of gravity, real birds fly preferentially in the horizontal directions, resulting in a kind of quasi-2d motion [14, 69]. For this reason, we believe our results may be of direct relevance for real birds.

From a learning perspective, our results are fairly robust under centralized training. The optimal flocking policy adopted by the agents consists of pure alignment at short distances and a combination of alignment and attraction at larger ones. Interestingly, we found that in the latter regime, the precise balance between alignment and attraction is not critical for maintaining cohesive flocking. This implies that multiple policies are equally effective — a redundancy that may contribute to behavioral robustness in biological systems. Decentralized training is almost equally efficient for moderate group sizes, leading to the same optimal policy, but it partially degrades for larger groups. Preliminary analysis suggests that this is due to individual agents not thoroughly exploring the full range of possible states.

Our findings help clarify the longstanding question of why some species flock while others swarm. Both collective behaviors ensure cohesion in groups of moving agents, but our results suggest that flocking may emerge as the optimal strategy not only for maintaining group cohesion but also for avoiding potentially dangerous collisions.

We finally note that our results may also prove useful beyond animal behavior, particularly in the field of swarm robotics [120]. In the future, it may be interesting to generalize these results to mixed-agent populations and environments with external threats/perturbations in order to extend the result of [74] to the full non-equilibrium dynamics learned by our agents.

Chapter 4

Conclusions & Outlook

In this thesis, we addressed the problem of cohesive flocking in open space, namely the emergence and maintenance of finite, self-bound collective motion in the absence of periodic boundaries. Our focus was on weakly cohesive flocks, which, in agreement with experimental observations, do not display positional order but instead exhibit a gas-like internal structure. This regime is particularly interesting because it is poorly explored and it lies beyond the typical setting of many classical flocking models, and therefore calls for a more refined understanding of how global coherence can arise in finite groups through the interplay of alignment and cohesion.

The problem was approached through two complementary perspectives. On the one hand, we developed a direct approach, based on the assumption of weak attractive interactions, and investigated their consequences both theoretically and numerically for the size and shape collective modes of the flock. On the other hand, we formulated an inverse problem, framed in the formalism of reinforcement learning, in order to provide a possible answer to the kind of objectives or biological imperatives that are satisfied by self propelled particles shoving cohesive collective motion.

The results of the first approach show that cohesive but structureless flocking can arise for weak pairwise attractive torques that are nondecreasing with distance. In particular, when the attractive force grows linearly with the distance to neighbouring individuals, the global size and shape modes of the flock exhibit an underlying Gaussian structure with underdamped oscillations, even for weak attractive perturbations of the overdamped Vicsek dynamics.. This leads to a clear characterization of the collective fluctuations of the flock, and we derived an experimentally testable relation connecting the characteristic oscillation time to the global extension of the flock. Importantly, this relation depends only on observable quantities, such as the flock polarization and the individual particle speed, making it potentially testable in real biological systems. Moreover, we provided numerical evidence that oscillations of the flock boundary can qualitatively modify the scaling of bulk equal-time velocity correlations, significantly weakening their power-law decay, a finding that calls for further theoretical scrutiny.

The second approach, based on reinforcement learning, demonstrated that cohesive flocking in open space can emerge as a learned collective strategy rather than being prescribed microscopically from the outset. In particular, the framework proved useful in disentangling the notions of swarming and flocking and the role played by aligning and attractive torques. We found that the requirement of staying together, taken alone, does not necessarily generate

a polarized flocking state; instead, it may be satisfied by a simpler swarming-like regime completely dominated by attractive torques. Collective motion in the strict sense emerges only when this condition is supplemented by the additional requirement of avoiding collisions which strongly favours alignment interactions with the closest neighbours. This result suggests that cohesion is not a secondary correction to standard flocking models, but a fundamental ingredient in the description of finite groups moving in open space.

Taken together, these findings support a broader conclusion: the physics of finite flocks cannot be reduced to alignment dynamics alone. Cohesion must be treated as an essential structural and dynamical ingredient, even in the weak cohesion limit that underlies the structureless gas-like structure exhibited by real flocks. Therefore, the interplay between attraction, alignment, and finite-size effects is central to understanding the emergence of collective motion in open environments. More generally, this thesis shows that the problem can be fruitfully addressed from two complementary angles: an interpretable microscopic perspective, which yields analytical insight into the collective modes of the system, and a learning-based inverse perspective, which reveals which simple biological imperatives are sufficient for cohesive motion to emerge.

Several extensions naturally follow from this work. On the direct side, the proposed relation between oscillation times and global flock extension calls for experimental validation, while a more detailed characterization of nonlinear attractive forces, of which here we have only scratched the surface, could clarify the robustness of the theory beyond the linear regime. A systematic study in three dimensions, of the consequence anisotropic scaling, would also be interesting, even if one may argue that due to gravity pure three dimensional flocks do not exist. Further extensions could incorporate non-reciprocal interactions, external perturbations, and quasi-two-dimensional models that explicitly account for fluctuations and damping induced by gravity in the vertical direction [14]. On the inverse side, it would be interesting to extend the reinforcement-learning framework to heterogeneous agents and to environments with external threats or perturbations. Such developments would also open the way toward applications in engineered collectives, particularly robotic swarms, where cohesion and collision avoidance must be balanced in a controlled and adaptive manner.

Overall, this thesis contributes to a more general theoretical picture in which cohesion is not merely a boundary condition on flocking, but a constitutive principle of finite collective motion. By combining analytical theory, numerical exploration, and machine-learning-based inference, we have taken a step toward a unified understanding of how self-bound flocks organize, fluctuate, and move in open space.

Appendix A

Appendix

A.1 Mode coupling Corrections

The leading mode-coupling corrections to the Gaussian solution of the transverse sector can be computed through the Lyapunov equation. Defining the stacked vector $\mathbf{Z}_k = (\mathbf{X}_k, \mathbf{\Pi}_k)^T$ we rewrite Eqs. (2.26)-(2.27) as

$$\dot{\mathbf{Z}}_k = \sum_h A_{kh}\mathbf{Z}_h + K\,\mathbf{\Xi}_k^{\perp} \tag{A.1}$$

with $K = (0, \sqrt{2\Gamma})^T$ and $A_{kh} = A_k^{(0)}\delta_{kh} + \delta A_{kh}$, with

$$A_k^{(0)} = \begin{pmatrix} 0 & v_0 \\ -\beta\lambda_k & -\gamma\lambda_k \end{pmatrix} \quad \text{and} \quad \delta A_{kh} = \begin{pmatrix} 0 & 0 \\ 0 & \beta Q_{kh} \end{pmatrix}. \tag{A.2}$$

where $Q_{hk}[Y]$ is the mode coupling matrix introduced in Section 2.2.1.

In the weak-cohesion regime the linear operator A is Hurwitz-stable (negative real part eigenvalues) and Eq.(A.1) admits a stationary solution. Its covariance matrix $\mathbf{\Sigma}_{kh} = \langle \mathbf{Z}_k \mathbf{Z}_h^T \rangle$ can be computed through the Lyapunov equation

$$\sum_p \left[A_{kp}\mathbf{\Sigma}_{ph} + \mathbf{\Sigma}_{kp}A_{hp}^T \right] = -(d-1)\delta_{kh}\, KK^T\,, \tag{A.3}$$

which in turn can be solved perturbatively. Defining $\mathbf{\Sigma} = \mathbf{\Sigma}^{(0)} + \delta\mathbf{\Sigma}$ and treating the slow longitudinal variables adiabatically, we obtain on the fast transverse timescale the Gaussian equation

$$A_k^{(0)}\mathbf{\Sigma}_{kh}^{(0)} + \mathbf{\Sigma}_{kh}^{(0)}(A_h^{(0)})^T = -(d-1)\delta_{kh}\, KK^T\,. \tag{A.4}$$

The Gaussian covariance matrix is diagonal in mode space, $\mathbf{\Sigma}_{kh}^{(0)} \propto \delta_{kh}$, with diagonal variances given by Eq. (2.34) and

$$\langle \mathbf{\Pi}_k^2 \rangle_0 = (d-1)\frac{\Gamma}{\gamma\lambda_k}\,, \quad (k > 0). \tag{A.5}$$

(From now on we denote the Gaussian level expectations with $\langle\cdot\rangle_0$).

Mode coupling corrections $\delta\mathbf{\Sigma}$ are then computed from the first-order Lyapunov equation

$$\delta A_{kh}\mathbf{\Sigma}_{hh}^{(0)} + \mathbf{\Sigma}_{kk}^{(0)}(\delta A_{hk})^T + A_k^{(0)}\delta\mathbf{\Sigma}_{kh} + \delta\mathbf{\Sigma}_{kh}(A_h^{(0)})^T = 0\,. \tag{A.6}$$

We are particularly interested in corrections to the transverse velocity covariance, which determines the longitudinal dynamics. Straightforward algebra gives

$$\Sigma^{\pi\pi}_{kh} \equiv \langle \mathbf{\Pi}_k \cdot \mathbf{\Pi}_h \rangle_Y = (d-1)\Gamma \left(\frac{\delta_{kh}}{\gamma \lambda_k} + \frac{\beta}{\gamma} \frac{(\lambda_k + \lambda_h) Q_{kh}[Y]}{\Lambda_{kh}} \right) \tag{A.7}$$

where

$$\Lambda_{kh} = \gamma \lambda_k \lambda_h (\lambda_k + \lambda_h) + \frac{\beta v_0}{2\gamma} (\lambda_k - \lambda_h)^2 \tag{A.8}$$

and the conditional mean $\langle \cdot \rangle_Y$ indicates the adiabatic expectation value at fixed longitudinal variables.

A.1.1 Longitudinal dynamics

We briefly discuss the slow longitudinal dynamics (2.19) neglecting the Coriolis-like term. In mode space one has

$$\dot{Y}_k = -\frac{v_0}{2} \sum_{hp>0} W_{khp} \mathbf{\Pi}_h \cdot \mathbf{\Pi}_p \tag{A.9}$$

so that, separating its adiabatic expectation from fluctuations, one has

$$\dot{Y}_k = -\frac{v_0}{2} \sum_{hp>0} W_{khp} \langle \mathbf{\Pi}_h \cdot \mathbf{\Pi}_p \rangle_Y + \Delta_k \tag{A.10}$$

where

$$\Delta_k(t) \equiv -\frac{v_0}{2} \sum_{hp>0} W_{khp} \left[\mathbf{\Pi}_h(t) \cdot \mathbf{\Pi}_p(t) - \langle \mathbf{\Pi}_h \cdot \mathbf{\Pi}_p \rangle_Y \right] \tag{A.11}$$

is a zero-mean effective noise, decorrelated on the slow longitudinal timescales,

$$\langle \Delta_k(t) \Delta_{k'}(t') \rangle \approx 2 D_{kk'} \delta(t - t'). \tag{A.12}$$

We can estimate its amplitude at the Gaussian level,

$$D_{kk'} \approx \frac{1}{2} \int_0^\infty dt \, \langle \Delta_k(t) \Delta_{k'}(0) \rangle_0 \, . \tag{A.13}$$

In this approximation, Wick's theorem allows us to reduce the four-point correlator to obtain

$$\begin{aligned}
\int_0^\infty dt \, \langle \Delta_k(t) \Delta_{k'}(0) \rangle &\approx \frac{v_0^2}{4} \sum_{h\,p\,h'p'>0} W_{khp} W_{k'h'p'} \int_0^\infty dt \\
&\quad \times \Big[\langle \mathbf{\Pi}_h(t) \cdot \mathbf{\Pi}_p(t) \; \mathbf{\Pi}_{h'}(0) \cdot \mathbf{\Pi}_{p'}(0) \rangle_0 - \langle \mathbf{\Pi}_h^2 \rangle_0 \, \langle \mathbf{\Pi}_{h'}^2 \rangle_0 \, \delta_{hp} \, \delta_{h'p'} \Big] \\
&= \frac{v_0^2}{2} \sum_{hp>0} W_{khp} \, W_{k'hp} \int_0^\infty dt \; \langle \mathbf{\Pi}_h(t) \cdot \mathbf{\Pi}_h(0) \rangle_0 \, \langle \mathbf{\Pi}_p(t) \cdot \mathbf{\Pi}_p(0) \rangle_0 \\
&\equiv \frac{v_0^2}{2} \sum_{hp>0} W_{khp} \, W_{k'hp} \; I_{hp} \, .
\end{aligned} \tag{A.14}$$

where the transverse velocity correlation function for positive times can be computed from Eq. (2.26),

$$\langle \mathbf{\Pi}_k(t)\cdot\mathbf{\Pi}_k(0)\rangle_0 = -v_0^{-2}\partial_t^2\langle \mathbf{X}_k(t)\cdot\mathbf{X}_k(0)\rangle_0. \tag{A.15}$$

Inserting Eq. (2.35) and using Eqs. (A.5), (2.36) one has

$$\langle \mathbf{\Pi}_k(t)\cdot\mathbf{\Pi}_k(0)\rangle_0 = \frac{(d-1)\Gamma}{\gamma\lambda_k}e^{-\frac{\gamma_k}{2}t}\left[\cos(\Omega_k t) - \frac{\gamma_k}{2\Omega_k}\sin(\Omega_k t)\right]. \tag{A.16}$$

It can be shown that the sum in Eq. (A.14) is dominated by diagonal terms $h = p$, whose integral has a simple form,

$$I_{hh} = \int_0^\infty dt\, \langle \mathbf{\Pi}_h(t)\cdot\mathbf{\Pi}_h(0)\rangle_0^2 = \frac{(d-1)^2\Gamma^2}{2\gamma_h^3} \tag{A.17}$$

so that

$$D_{k\,k'} \approx \frac{(d-1)^2 v_0^2\Gamma^2}{8\gamma^3}\sum_{h>0}\frac{W_{khh}W_{k'hh}}{\lambda_h^3}. \tag{A.18}$$

We finally discuss the drift part of Eq. (A.10). Using the adiabatic transverse covariance (A.7), it can be decomposed into a constant term

$$F_k = -\frac{v_0}{2}(d-1)\frac{\Gamma}{\gamma}\sum_{h>0}\frac{W_{khh}}{\lambda_h} \tag{A.19}$$

originating from the Gaussian diagonal covariance and a linear one

$$M_{kh} = \frac{v_0}{2}(d-1)\Gamma\frac{\beta}{\gamma}\lambda_h\sum_{pm>0}W_{kpm}W_{hpm}\frac{\lambda_p+\lambda_m}{\Lambda_{pm}} \tag{A.20}$$

due to the Y-dependent mode-coupling correction, yielding the shifted OU equation

$$\dot{Y}_k = F_k - \sum_{h>0}M_{kh}Y_h + \Delta_k. \tag{A.21}$$

Note that, for $k > 0$, the triple overlap $W_{khh} = \sum_i w_i^{(k)}(w_i^{(h)})^2$ is the projection of the positive field $(w_i^{(h)})^2$ onto the nonuniform mode k. Therefore, it only measures its nonuniform part, which is expected to be small. Moreover, the sum over h is signed, so additional cancellations in the sum are expected, yielding $F_k \approx 0$ (or better, negligible w.r.t. fluctuations) for $k > 0$. Only the zeroth translational mode receives a relevant constant drift contribution originating from the average of π_i^2 over the entire flock.

By the same argument one can argue that the off-diagonal elements of both D and M are expected to be negligible: they involve signed products of small nonuniform overlap projections and are suppressed by cancellations. Conversely, the diagonal elements are sums of squares and remain finite. Hence

D and M are expected to be approximately diagonal, $D_{kh} \approx D_k \delta_{kh}$ and $M_{kh} \approx M_k \delta_{kh}$ with

$$D_k = \frac{(d-1)^2 v_0^2 \Gamma^2}{8\gamma^3} \sum_{h>0} \frac{W_{khh}^2}{\lambda_h^3} \,. \tag{A.22}$$

and

$$M_k = \frac{v_0}{2}(d-1)\Gamma \frac{\beta}{\gamma^2} \lambda_k \sum_{p>0} \frac{W_{kpp}^2}{\lambda_p^2} > 0 \tag{A.23}$$

where we have also recognized that the sum in Eq. (A.20) is dominated by terms $p = m$ and used $\Lambda_{pp} = 2\gamma\lambda_p^3$. We have thus recovered the effective OU Eq. (A.10).

A.1.2 Stationary longitudinal variance

We focus here on the two-dimensional case, where the longitudinal and the transverse sector share the same scaling behaviour, while three-dimensional flocks display a anisotropic scale, as one can see in Fig. 2.8. We therefore assume d=2. The stationary longitudinal variance is thus, for each approximately decoupled mode $k > 0$,

$$\langle Y_k^2 \rangle \approx \frac{D_k}{2M_k} = \frac{\Gamma v_0}{8\gamma\beta} \frac{1}{\lambda_k} \frac{\sum_{h>0} W_{khh}^2 \lambda_h^{-3}}{\sum_{p>0} W_{kpp}^2 \lambda_p^{-2}} \,. \tag{A.24}$$

We finally note that the ratio

$$R_k = \frac{\sum_{h>0} W_{khh}^2 \lambda_h^{-3}}{\sum_{p>0} W_{kpp}^2 \lambda_p^{-2}} \equiv \sum_{h>0} \mu_{kh} \lambda_h^{-1} \tag{A.25}$$

is a weighted average of the inverse eigenvalue λ_h^{-1} with weights

$$\mu_{kh} = \frac{W_{khh}^2 \lambda_h^{-2}}{\sum_{p>0} W_{kpp}^2 \lambda_p^{-2}} \,, \qquad \sum_{h>0} \mu_{kh} = 1 \,. \tag{A.26}$$

For a graph Laplacian with local connections, modes with nearby indices have similar scales, so that the triple overlap coefficients are expected to be dominated by terms with similar indices and μ_{kh} is concentrated on modes with λ_h of the same order as λ_k. Therefore $R_k \sim \lambda_k^{-1}$ up to an $O(1)$ factor. Comparing Eq. (2.34) with (A.24) we conclude that the longitudinal and transverse variances share the same scaling $\sim \lambda_k^{-2}$ with $\langle Y_k^2 \rangle \lesssim \langle \mathbf{X}_k^2 \rangle$.

A.2 Autocorrelation shape

At the Gaussian level, the fluctuations of the flock boundary are described by independent normal modes. In this approximation, the connected autocorrelation of the squared gyration radius,

$$G_g(t) \approx G_\perp(t) = \langle \delta R_g^2(t)\, \delta R_g^2(0) \rangle, \tag{A.27}$$

is expected to factorize according to Wick's theorem:

$$\begin{aligned} G_\perp &= \langle R_g^2(t) R_g^2(0)\rangle - \langle R_g^2\rangle^2 \\ &= \langle R_g(t)R_g(t)\rangle\langle R_g(0)R_g(0)\rangle \;+\; \langle R_g(t)R_g(0)\rangle\langle R_g(t)R_g(0)\rangle \;+ \\ &\quad +\;\; \langle R_g(t)R_g(0)\rangle\langle R_g(t)R_g(0)\rangle \\ &= 2\langle R_g(t)R_g(0)\rangle^2 \\ &= 2\left\langle \sum_k \mathbf{X}_k(t)\mathbf{X}_k(0)\right\rangle \\ &= 2\sum_k C_k^2 \end{aligned} \tag{A.28}$$

where C_k are the transverse mode autocorrelations given by Eq. (2.35). The sum is approximately dominated by the lowest mode autocorrelation, so that

$$G_\perp(t) \sim C_1^2(t). \tag{A.29}$$

If $C_1(t)$ displays damped oscillations, squaring the correlator removes the sign changes and doubles the oscillation frequency. Consequently, within the Gaussian theory the connected autocorrelation of R_g^2 should not exhibit negative lobes.

This prediction is in clear contrast with the numerical results. The measured autocorrelation of R_g^2 oscillates with the same qualitative structure as the correlator of R_g itself, including pronounced negative regions. Such behavior strongly suggests that nonlinear effects and mode coupling cannot be neglected. In particular, the persistence of the sign-changing structure indicates the presence of correlations beyond Gaussian factorization, generated by interactions among boundary modes. At a phenomenological level, this suggests a decomposition of the form

$$G_\perp(t) \sim C_1^2(t) + C_1(t)\, E(t), \tag{A.30}$$

where the second term encodes non-Gaussian corrections arising from mode coupling, and $E(t)$ represents a slowly varying envelope associated with the collective nonlinear dynamics. While a detailed derivation of the function $E(t)$ is beyond the scope of the present work, the numerical evidence clearly indicates that the Gaussian approximation alone is insufficient to capture the exact shape of the shape fluctuations autocorrelation beyond the simple scaling of the associated transverse timescale $\tau_\perp$.

Bibliography

[1]R. Livi and P. Politi, *Nonequilibrium statistical physics: a modern perspective* (Cambridge University Press, 2017).

[2]M. Kardar, G. Parisi, and Y.-C. Zhang, "Dynamic scaling of growing interfaces", Phys. Rev. Lett. **56**, 889 (1986).

[3]S. Alexandre and Z. Yongfeng, "The surprising physics of interfaces in active matter", Chin. Phys. Lett. (2025).

[4]T. Vicsek, A. Czirók, E. Ben-Jacob, I. Cohen, and O. Shochet, "Novel type of phase transition in a system of self-driven particles", Phys. Rev. Lett. **75**, 1226 (1995).

[5]J. Toner and Y. Tu, "Long-range order in a two-dimensional dynamical xy model: how birds fly together", Phys. Rev. Lett. **75**, 4326 (1995).

[6]H.-P. Zhang, A. Be'er, E.-L. Florin, and H. L. Swinney, "Collective motion and density fluctuations in bacterial colonies", Proc. Natl. Acad. Sci. U.S.A. **107**, 13626–13630 (2010).

[7]F. Giavazzi, C. Malinverno, S. Corallino, F. Ginelli, G. Scita, and R. Cerbino, "Giant fluctuations and structural effects in a flocking epithelium", J. Phys. D: Appl. Phys. **50**, 384003 (2017).

[8]X. Trepat, M. R. Wasserman, T. E. Angelini, E. Millet, D. A. Weitz, J. P. Butler, and J. J. Fredberg, "Physical forces during collective cell migration", Nat. Phys. **5**, 426–430 (2009).

[9]J. K. Parrish, W. Hamner, and W. M. Hamner, *Animal groups in three dimensions: how species aggregate* (Cambridge University Press, 1997).

[10]F. Ginelli, F. Peruani, M.-H. Pillot, H. Chaté, G. Theraulaz, and R. Bon, "Intermittent collective dynamics emerge from conflicting imperatives in sheep herds", Proc. Natl. Acad. Sci. U.S.A. **112**, 12729–12734 (2015).

[11]I. D. Couzin, J. Krause, R. James, G. D. Ruxton, and N. R. Franks, "Collective memory and spatial sorting in animal groups", J. Theor. Biol. **218**, 1–11 (2002).

[12]A. Cavagna, A. Cimarelli, I. Giardina, G. Parisi, R. Santagati, F. Stefanini, and M. Viale, "Scale-free correlations in starling flocks", Proc. Natl. Acad. Sci. U.S.A. **107**, 11865–11870 (2010).

[13]F. Ginelli, "The physics of the vicsek model", Eur. Phys. J. Spec. Top. **225**, 2099–2117 (2016).

[14]J. Toner and Y. Tu, "Flocks, herds, and schools: a quantitative theory of flocking", Phys. Rev. E **58**, 4828 (1998).

[15]J. Toner, Y. Tu, and S. Ramaswamy, "Hydrodynamics and phases of flocks", Ann. Phys. (N.Y.) **318**, 170–244 (2005).

[16]H. Chaté, F. Ginelli, G. Grégoire, and F. Raynaud, "Collective motion of self-propelled particles interacting without cohesion", Phys. Rev. E **77**, 046113 (2008).

[17]G. Grégoire, H. Chaté, and Y. Tu, "Moving and staying together without a leader", Physica D **181**, 157–170 (2003).

[18]M. Camperi, A. Cavagna, I. Giardina, G. Parisi, and E. Silvestri, "Spatially balanced topological interaction grants optimal cohesion in flocking models", Interface Focus **2**, 715–725 (2012).
[19]C. W. Reynolds, "Flocks, herds and schools: a distributed behavioral model", in Proceedings of the 14th annual conference on computer graphics and interactive techniques (1987), pp. 25–34.
[20]A. Cavagna, A. Cimarelli, I. Giardina, A. Orlandi, G. Parisi, A. Procaccini, R. Santagati, and F. Stefanini, "New statistical tools for analyzing the structure of animal groups", Math. Biosci. **214**, 32–37 (2008).
[21]G. Fava, A. Gambassi, and F. Ginelli, "Strong casimir-like forces in flocking active matter", Phys. Rev. Lett. **133**, 148301 (2024).
[22]L. Lenzini, G. Fava, and F. Ginelli, "Boundary symmetry breaking of flocking systems", J. Stat. Mech. **2024**, 083210 (2024).
[23]R. Aditi Simha and S. Ramaswamy, "Hydrodynamic fluctuations and instabilities in ordered suspensions of self-propelled particles", Phys. Rev. Lett. **89**, 058101 (2002).
[24]H. Chaté and B. Mahault, "Dry, Aligning, Dilute, Active Matter: A Synthetic and Self-contained Overview", in *Active Matter and Nonequilibrium Statistical Physics: Lecture Notes of the Les Houches Summer School: Volume 112, September 2018* (Oxford University Press, 2022).
[25]M. Ballerini, N. Cabibbo, R. Candelier, A. Cavagna, E. Cisbani, I. Giardina, V. Lecomte, A. Orlandi, G. Parisi, A. Procaccini, M. Viale, and V. Zdravkovic, "Interactions ruling animal collective behavior depends on topological rather than metric distance: evidence from a field study", Proc. Natl. Acad. Sci. U.S.A. **105**, 1232–1237 (2008).
[26]Y. Fily and M. C. Marchetti, "Athermal phase separation of self-propelled particles with no alignment", Phys. Rev. Lett. **108**, 235702 (2012).
[27]O. Granek, Y. Kafri, M. Kardar, S. Ro, J. Tailleur, and A. Solon, "Colloquium: inclusions, boundaries, and disorder in scalar active matter", Rev. Mod. Phys. **96**, 031003 (2024).
[28]M. J. Schnitzer, "Theory of continuum random walks and application to chemotaxis", Phys. Rev. E **48**, 2553–2568 (1993).
[29]G. S. Redner, A. Baskaran, and M. F. Hagan, "Reentrant phase behavior in active colloids with attraction", Phys. Rev. E **88**, 012305 (2013).
[30]A. Duzgun and J. V. Selinger, "Active brownian particles near straight or curved walls: pressure and boundary layers", Phys. Rev. E **97**, 032606 (2018).
[31]N. Sepúlveda, L. Petitjean, O. Cochet, E. Grasland-Mongrain, P. Silberzan, and V. Hakim, "Collective cell motion in an epithelial sheet can be quantitatively described by a stochastic interacting particle model", PLoS Comput. Biol. **9**, e1002944 (2013).
[32]Y. Fily, A. Baskaran, and M. F. Hagan, "Dynamics and density distribution of strongly confined noninteracting nonaligning self-propelled particles in a nonconvex boundary", Phys. Rev. E **91**, 012125 (2015).
[33]G. Szamel, "Self-propelled particle in an external potential: existence of an effective temperature", Phys. Rev. E **90**, 012111 (2014).
[34]F. Giavazzi, M. Paoluzzi, M. Marta, B. Dapeng, G. Scita, M. L. Manning, R. Cerbino, and M. C. Marchetti, "Flocking transitions in confluent tissues", Soft Matter **16**, 2208 (2018).

[35]J. R. Howse, R. A. Jones, A. J. Ryan, T. Gough, R. Vafabakhsh, and R. Golestanian, "Self-motile colloidal particles: from directed propulsion to random walk", Phys. Rev. Lett. **99**, 048102 (2007).
[36]J. Deseigne, O. Dauchot, and H. Chaté, "Collective motion of vibrated polar disks", Phys. Rev. Lett. **105**, 098001 (2010).
[37]P. Häunggi and P. Jung, "Colored noise in dynamical systems", Adv. Chem. Phys. **89**, 239–326 (1994).
[38]J. Stenhammar, D. Marenduzzo, R. J. Allen, and M. E. Cates, "Phase behaviour of active brownian particles: the role of dimensionality", Soft Matter **10**, 1489–1499 (2014).
[39]C. Liu, X. Fu, L. Liu, X. Ren, C. K. Chau, S. Li, L. Xiang, H. Zeng, G. Chen, L.-H. Tang, et al., "Sequential establishment of stripe patterns in an expanding cell population", Science **334**, 238–241 (2011).
[40]J. D'Alessandro, A. P. Solon, Y. Hayakawa, C. Anjard, F. Detcheverry, J.-P. Rieu, and C. Rivière, "Contact enhancement of locomotion in spreading cell colonies", Nat. Phys. **13**, 999–1005 (2017).
[41]M. B. Miller and B. L. Bassler, "Quorum sensing in bacteria", Annu. Rev. Microbiol. **55**, 165–199 (2001).
[42]I. Buttinoni, J. Bialké, F. Kümmel, H. Löwen, C. Bechinger, and T. Speck, "Dynamical clustering and phase separation in suspensions of self-propelled colloidal particles", Phys. Rev. Lett. **110**, 238301 (2013).
[43]J. Palacci, S. Sacanna, A. P. Steinberg, D. J. Pine, and P. M. Chaikin, "Living crystals of light-activated colloidal surfers", Science **339**, 936–940 (2013).
[44]G. Spera, C. Duclut, M. Durand, and J. Tailleur, "Nematic torques in scalar active matter: when fluctuations favor polar order and persistence", Phys. Rev. Lett. **132**, 078301 (2024).
[45]M. E. Cates and J. Tailleur, "Motility-induced phase separation", Annu. Rev. Condens. Matter Phys. **6**, 219–244 (2015).
[46]J. O'Byrne, Y. Kafri, J. Tailleur, and F. van Wijland, "Time irreversibility in active matter, from micro to macro", Nat. Rev. Phys. **4**, 167–183 (2022).
[47]L. Caprini, U. Marini Bettolo Marconi, and A. Puglisi, "Spontaneous velocity alignment in motility-induced phase separation", Phys. Rev. Lett. **124**, 078001 (2020).
[48]B. Szabo, G. Szöllösi, B. Gönci, Z. Jurányi, D. Selmeczi, and T. Vicsek, "Phase transition in the collective migration of tissue cells: experiment and model", Phys. Rev. E **74**, 061908 (2006).
[49]S. Henkes, Y. Fily, and M. C. Marchetti, "Active jamming: self-propelled soft particles at high density", Phys. Rev. E **84**, 040301 (2011).
[50]J. Toner, "Reanalysis of the hydrodynamic theory of fluid, polar-ordered flocks", Phys. Rev. E **86**, 031918 (2012).
[51]S. SenGupta, C. A. Parent, and J. E. Bear, "The principles of directed cell migration", Nat. Rev. Mol. Cell Biol. **22**, 529–547 (2021).
[52]M. Brambati, G. Fava, and F. Ginelli, "Signatures of directed and spontaneous flocking", Phys. Rev. E **106**, 024608 (2022).
[53]N. D. Mermin and H. Wagner, "Absence of ferromagnetism or antiferromagnetism in one-or two-dimensional isotropic heisenberg models", Phys. Rev. Lett. **17**, 1133 (1966).

[54]J. Toner, "Birth, death, and flight: a theory of malthusian flocks", Phys. Rev. Lett. **108**, 088102 (2012).
[55]E. Bertin, M. Droz, and G. Grégoire, "Boltzmann and hydrodynamic description for self-propelled particles", Phys. Rev. E **74**, 022101 (2006).
[56]E. Bertin, M. Droz, and G. Grégoire, "Hydrodynamic equations for self-propelled particles: microscopic derivation and stability analysis", J. Phys. A: Math. Theor. **42**, 445001 (2009).
[57]J. M. Kosterlitz and D. J. Thouless, "Ordering, metastability and phase transitions in two-dimensional systems", J. Phys. C: Solid State Phys. **6**, 1181 (1973).
[58]J. Toner, *The physics of flocking: birth, death, and flight in active matter* (Cambridge University Press, 2024).
[59]H. Nishimori and G. Ortiz, *Elements of phase transitions and critical phenomena* (Oxford University Press, Oxford, 2010).
[60]N. Kyriakopoulos, F. Ginelli, and J. Toner, "Leading birds by their beaks: the response of flocks to external perturbations", New J. Phys. **18**, 073039 (2016).
[61]H. Chaté and A. Solon, "Dynamic scaling of two-dimensional polar flocks", Phys. Rev. Lett. **132**, 268302 (2024).
[62]D. Forster, D. R. Nelson, and M. J. Stephen, "Large-distance and long-time properties of a randomly stirred fluid", Phys. Rev. A **16**, 732 (1977).
[63]B. Mahault, F. Ginelli, and H. Chaté, "Quantitative assessment of the toner and tu theory of polar flocks", Phys. Rev. Lett. **123**, 218001 (2019).
[64]M. Besse, H. Chaté, and A. Solon, "Metastability of constant-density flocks", Phys. Rev. Lett. **129**, 268003 (2022).
[65]L. Chen, P. Jentsch, C. F. Lee, A. Maitra, S. Ramaswamy, and J. Toner, *The inconvenient truth about flocks*, 2025.
[66]H. Chaté and A. Solon, *Comment on "the inconvenient truth about flocks" by chen et al*, 2025.
[67]L. Chen, P. Jentsch, C. F. Lee, A. Maitra, S. Ramaswamy, and J. Toner, *Response to the comment on the inconvenient truth about flocks by chaté and solon*, 2025.
[68]H. Chaté and A. Solon, *Continuing the discussion on "the inconvenient truth about flocks" by chen et al*, 2025.
[69]M. Ballerini, N. Cabibbo, R. Candelier, A. Cavagna, E. Cisbani, I. Giardina, A. Orlandi, G. Parisi, A. Procaccini, M. Viale, et al., "Empirical investigation of starling flocks: a benchmark study in collective animal behaviour", Anim. Behav. **76**, 201–215 (2008).
[70]J. Gautrais, C. Jost, M. Soria, A. Campo, S. Motsch, R. Fournier, S. Blanco, and G. Theraulaz, "Analyzing fish movement as a persistent turning walker", J. Math. Biol. **58**, 429–445 (2009).
[71]A. Cavagna, I. Giardina, F. Ginelli, T. Mora, D. Piovani, R. Tavarone, and A. M. Walczak, "Dynamical maximum entropy approach to flocking", Phys. Rev. E **89**, 042707 (2014).
[72]J. Gautrais, F. Ginelli, R. Fournier, S. Blanco, M. Soria, H. Chaté, and G. Theraulaz, "Deciphering interactions in moving animal groups", PLoS Comput. Biol. **8**, 1–11 (2012).

[73]F. Ginelli and H. Chaté, "Relevance of metric-free interactions in flocking phenomena", Phys. Rev. Lett. **105**, 168103 (2010).
[74]A. Cavagna, I. Giardina, and F. Ginelli, "Boundary information inflow enhances correlation in flocking", Phys. Rev. Lett. **110**, 168107 (2013).
[75]A. Attanasi, A. Cavagna, L. Del Castello, I. Giardina, T. S. Grigera, A. Jelić, S. Melillo, L. Parisi, O. Pohl, E. Shen, et al., "Information transfer and behavioural inertia in starling flocks", Nat. Phys. **10**, 691–696 (2014).
[76]Y. Tu, J. Toner, and M. Ulm, "Sound waves and the absence of galilean invariance in flocks", Phys. Rev. Lett. **80**, 4819 (1998).
[77]A. Cavagna, I. Giardina, T. S. Grigera, A. Jelic, D. Levine, S. Ramaswamy, and M. Viale, "Silent flocks: constraints on signal propagation across biological groups", Phys. Rev. Lett. **114**, 218101 (2015).
[78]A. Cavagna, L. Del Castello, I. Giardina, T. Grigera, A. Jelic, S. Melillo, T. Mora, L. Parisi, E. Silvestri, M. Viale, et al., "Flocking and turning: a new model for self-organized collective motion", J. Stat. Phys. **158**, 601–627 (2015).
[79]P. M. Chaikin and T. C. Lubensky, *Principles of condensed matter physics* (Cambridge University Press, 1995).
[80]C. M. Breder, "Fish schools as operational structures", Fish. Bull. **74**, 471–502 (1976).
[81]F. Ferretti, S. Grosse-Holz, C. Holmes, J. L. Shivers, I. Giardina, T. Mora, and A. M. Walczak, "Signatures of irreversibility in microscopic models of flocking", Phys. Rev. E **106**, 034608 (2022).
[82]T. Mora, A. M. Walczak, L. Del Castello, F. Ginelli, S. Melillo, L. Parisi, M. Viale, A. Cavagna, and I. Giardina, "Local equilibrium in bird flocks", Nat. Phys. **12**, 1153–1157 (2016).
[83]D. J. Pearce, A. M. Miller, G. Rowlands, and M. S. Turner, "Role of projection in the control of bird flocks", Proc. Natl. Acad. Sci. U.S.A. **111**, 10422–10426 (2014).
[84]J. Giraldo-Barreto and V. Holubec, "Active matter flocking via predictive alignment", arXiv preprint arXiv:2504.07778 (2025).
[85]C. Heins, B. Millidge, L. Da Costa, R. P. Mann, K. J. Friston, and I. D. Couzin, "Collective behavior from surprise minimization", Proc. Natl. Acad. Sci. U.S.A. **121**, e2320239121 (2024).
[86]T. Niizato and Y.-P. Gunji, "Metric–topological interaction model of collective behavior", Ecol. Modell. **222**, 3041–3049 (2011).
[87]M. Moussaid, S. Garnier, G. Theraulaz, and D. Helbing, "Collective information processing and pattern formation in swarms, flocks, and crowds", Top. Cogn. Sci. **1**, 469–497 (2009).
[88]A. Peshkov, S. Ngo, E. Bertin, H. Chaté, and F. Ginelli, "Continuous theory of active matter systems with metric-free interactions", Phys. Rev. Lett. **109**, 098101 (2012).
[89]D. Martin, H. Chaté, C. Nardini, A. Solon, J. Tailleur, and F. Van Wijland, "Fluctuation-induced phase separation in metric and topological models of collective motion", Phys. Rev. Lett. **126**, 148001 (2021).
[90]W. S. Geisler and D. G. Albrecht, "Visual cortex neurons in monkeys and cats: detection, discrimination, and identification", Vis. Neurosci. **14**, 897–919 (1997).

[91]R. Burioni and D. Cassi, "Universal properties of spectral dimension", Phys. Rev. Lett. **76**, 1091 (1996).
[92]H. Weyl, "Über die asymptotische verteilung der eigenwerte", Nachrichten von der Gesellschaft der Wissenschaften zu Göttingen, Mathematisch-Physikalische Klasse **1911**, 110–117 (1911).
[93]P. Kröger, "Upper bounds for the neumann eigenvalues on a bounded domain in euclidean space", J. Funct. Anal. **106**, 353–357 (1992).
[94]P. Kroger, "Estimates for sums of eigenvalues of the laplacian", J. Funct. Anal. **126**, 217–227 (1994).
[95]A. Cavagna, I. Giardina, and T. S. Grigera, "The physics of flocking: correlation as a compass from experiments to theory", Phys. Rep. **728**, 1–62 (2018).
[96]H. Chaté, F. Ginelli, G. Grégoire, F. Peruani, and F. Raynaud, "Modeling collective motion: variations on the vicsek model", Eur. Phys. J. B **64**, 451–456 (2008).
[97]A. Cavagna, I. Giardina, A. Orlandi, G. Parisi, and A. Procaccini, "The starflag handbook on collective animal behaviour: part ii, three-dimensional analysis", arXiv preprint arXiv:0802.1674 (2008).
[98]E. Tjhung, D. Marenduzzo, and M. E. Cates, "Spontaneous symmetry breaking in active droplets provides a generic route to motility", Proc. Natl. Acad. Sci. U.S.A. **109**, 12381–12386 (2012).
[99]C. A. Whitfield, D. Marenduzzo, R. Voituriez, and R. J. Hawkins, "Active polar fluid flow in finite droplets", Eur. Phys. J. E **37**, 8 (2014).
[100]H. Rackham, W. Jones, and D. Eichholz, "Pliny natural history (the loeb classical library)", London, Cambridge (1942).
[101]A. Attanasi, A. Cavagna, L. Del Castello, I. Giardina, S. Melillo, L. Parisi, O. Pohl, B. Rossaro, E. Shen, E. Silvestri, et al., "Finite-size scaling as a way to probe near-criticality in natural swarms", Phys. Rev. Lett. **113**, 238102 (2014).
[102]A. Cavagna, D. Conti, C. Creato, L. Del Castello, I. Giardina, T. S. Grigera, S. Melillo, L. Parisi, and M. Viale, "Dynamic scaling in natural swarms", Nat. Phys. **13**, 914–918 (2017).
[103]J. K. Parrish and L. Edelstein-Keshet, "Complexity, pattern, and evolutionary trade-offs in animal aggregation", Science **284**, 99–101 (1999).
[104]A. Attanasi, A. Cavagna, L. Del Castello, I. Giardina, S. Melillo, L. Parisi, O. Pohl, B. Rossaro, E. Shen, E. Silvestri, et al., "Collective behaviour without collective order in wild swarms of midges", PLoS Comput. Biol. **10**, e1003697 (2014).
[105]M. Durve, F. Peruani, and A. Celani, "Learning to flock through reinforcement", Phys. Rev. E **102**, 012601 (2020).
[106]F. Borra, M. Cencini, and A. Celani, "Optimal collision avoidance in swarms of active brownian particles", J. Stat. Mech. **2021**, 083401 (2021).
[107]R. S. Sutton, A. G. Barto, et al., *Reinforcement learning: an introduction*, Vol. 1, 1 (MIT press Cambridge, 1998).
[108]R. E. Bellman and S. E. Dreyfus, *Applied dynamic programming* (Princeton university press, 2015).
[109]R. C. Löffler, E. Panizon, and C. Bechinger, "Collective foraging of active particles trained by reinforcement learning", Sci. Rep. **13**, 17055 (2023).

[110]W. Cai, G. Wang, Y. Zhang, X. Qu, and Z. Huang, "Reinforcement learning for active matter", arXiv preprint arXiv:2503.23308 (2025).
[111]S. Monter, V.-L. Heuthe, E. Panizon, and C. Bechinger, "Dynamics and risk sharing in groups of selfish individuals", J. Theor. Biol. **562**, 111433 (2023).
[112]G. Grégoire and H. Chaté, "Onset of collective and cohesive motion", Phys. Rev. Lett. **92**, 025702 (2004).
[113]X. Wang, S. Liu, Y. Yu, S. Yue, Y. Liu, F. Zhang, and Y. Lin, "Modeling collective motion for fish schooling via multi-agent reinforcement learning", Ecol. Modell. **477**, 110259 (2023).
[114]S. Singh, T. Jaakkola, M. L. Littman, and C. Szepesvári, "Convergence results for single-step on-policy reinforcement-learning algorithms", Mach. Learn. **38**, 287–308 (2000).
[115]H. Edelsbrunner, D. Kirkpatrick, and R. Seidel, "On the shape of a set of points in the plane", IEEE Trans. Inf. Theory **29**, 551–559 (2003).
[116]M. Brambati, G. Baj, and F. Ginelli, "*In preparation*", (2026).
[117]I. Aoki, "An analysis of the schooling behavior of fish: internal organization and communication process", Bull. Ocean Res. Inst. Univ. Tokyo **12**, 1–65 (1980).
[118]A. Huth and C. Wissel, "The simulation of the movement of fish schools", J. Theor. Biol. **156**, 365–385 (1992).
[119]J. Krause and G. Ruxton, "Important topics in group living", Social behaviour: genes, ecology and evolution, 203–225 (2010).
[120]H. Hamann, *Swarm robotics: a formal approach*, Vol. 221 (Springer, 2018).